



**IMPROVED DICTIONARY FORMATION AND SEARCH FOR SYNTHETIC  
APERTURE RADAR CANONICAL SHAPE FEATURE EXTRACTION**

**THESIS**

Matthew P. Crosser, Captain, USAF

AFIT-ENG-14-M-21

**DEPARTMENT OF THE AIR FORCE  
AIR UNIVERSITY**

***AIR FORCE INSTITUTE OF TECHNOLOGY***

**Wright-Patterson Air Force Base, Ohio**

DISTRIBUTION STATEMENT A:  
APPROVED FOR PUBLIC RELEASE; DISTRIBUTION UNLIMITED

The views expressed in this thesis are those of the author and do not reflect the official policy or position of the United States Air Force, the Department of Defense, or the United States Government.

This material is declared a work of the U.S. Government and is not subject to copyright protection in the United States.

AFIT-ENG-14-M-21

IMPROVED DICTIONARY FORMATION AND SEARCH FOR SYNTHETIC  
APERTURE RADAR CANONICAL SHAPE FEATURE EXTRACTION

THESIS

Presented to the Faculty  
Department of Electrical and Computer Engineering  
Graduate School of Engineering and Management  
Air Force Institute of Technology  
Air University  
Air Education and Training Command  
in Partial Fulfillment of the Requirements for the  
Degree of Master of Science in Electrical Engineering

Matthew P. Crosser, BS, MBA

Captain, USAF

March 2014

DISTRIBUTION STATEMENT A:  
APPROVED FOR PUBLIC RELEASE; DISTRIBUTION UNLIMITED

AFIT-ENG-14-M-21

IMPROVED DICTIONARY FORMATION AND SEARCH FOR SYNTHETIC  
APERTURE RADAR CANONICAL SHAPE FEATURE EXTRACTION

Matthew P. Crosser, BS, MBA  
Captain, USAF

Approved:

//signed//  
\_\_\_\_\_  
Julie A. Jackson, PhD (Chairman)

13 Mar 2014  
\_\_\_\_\_  
Date

//signed//  
\_\_\_\_\_  
Brett J. Borghetti, PhD (Member)

12 Mar 2014  
\_\_\_\_\_  
Date

//signed//  
\_\_\_\_\_  
Capt Dustin G. Mixon, PhD (Member)

14 Mar 2014  
\_\_\_\_\_  
Date

**Abstract**

Automatic target recognition (ATR) requires detecting and estimating distinguishing characteristics of a target of interest. Radar data provides range and amplitude information; range distinguishes location relative to the radar whereas amplitude determines strength of reflectivity. Strong reflecting scattering features of targets are detected from a combination of radar returns, or radar phase history (PH) data. Strong scatterers are modeled as canonical shapes (a plate, dihedral, trihedral, sphere, cylinder, or top-hat). Modeling the scatterers as canonical shapes takes the high dimensional radar PH from each scatterer and parameterizes the scatterer according to its location, size, and orientation.

This thesis efficiently estimates the parameters of canonical shapes from radar PH data using dictionary search. Target scattering peaks are detected using 2-D synthetic aperture radar (SAR) imaging. The parameters are estimated with decreased computation and improved accuracy relative to previous algorithms through reduced SAR image processing, informed parameter subspace bounding, and more efficient dictionary clustering. The effects of the collection flight path and radar parameters are investigated to permit pre-collection error analysis. The results show that even for a limited collection geometry, the dictionary estimates the canonical shape scatterer parameters well.

## **Acknowledgments**

I would like to especially thank my partner for daily support and motivation to make it through this thesis. Secondly, thank you to my advisor, Dr. Jackson. Your technical expertise and regular guidance allowed me to push myself in this thesis. This thesis research was sponsored by the Air Force Office of Scientific Research under lab task LRIR12RY19COR.

Matthew P. Crosser

## Table of Contents

	Page
Abstract . . . . .	iv
Acknowledgments . . . . .	v
Table of Contents . . . . .	vi
List of Figures . . . . .	viii
List of Tables . . . . .	xi
List of Symbols . . . . .	xv
List of Acronyms . . . . .	xix
 I. Introduction . . . . .	 1
1.1 Problem Statement . . . . .	1
1.2 State of the art . . . . .	2
1.3 Objectives and Methodology . . . . .	3
1.4 Thesis Chapters . . . . .	4
 II. Background . . . . .	 6
2.1 Technical Overview . . . . .	6
2.2 Scattering Parametric Models . . . . .	9
2.2.1 2-D Scattering Models . . . . .	10
2.2.2 3-D Scattering Models . . . . .	11
2.3 Background Summary . . . . .	18
 III. Data Collection and Pre-Processing . . . . .	 20
3.1 Step 1A: Collection Flight Path and Radar Parameters Analysis . . . . .	21
3.1.1 Collection Flight Path . . . . .	22
3.1.1.1 Shape geometry . . . . .	22
3.1.1.2 Mathematic solution . . . . .	25
3.1.1.3 Flight Paths . . . . .	27
3.1.2 Collection Radar Parameters . . . . .	30
3.2 Step 1B: Error Analysis Pre-Processing . . . . .	32

	Page
3.2.1 Representative Parameter Set . . . . .	33
3.2.2 Location Error Analysis . . . . .	34
3.2.3 Size Error Analysis . . . . .	45
3.2.4 Orientation Error Analysis . . . . .	55
3.3 Step 1C: Data Collection, SAR Image Formation, and Pre-Processing . . .	57
3.3.1 2-D SAR Image Formation and Segmentation . . . . .	58
3.3.2 Model Order Estimation . . . . .	73
3.3.3 2-D Location Estimation . . . . .	73
3.3.4 Peak Association . . . . .	78
IV. Initial Shape Type Estimation and Parameter Estimation and Bounding . . . . .	81
4.1 Step 2A: Spotlight Partitioned Flight Path Phase Histories . . . . .	82
4.2 Step 2B: Initial Shape Type Estimate - The SPLIT Algorithm . . . . .	84
4.3 Step 2C: Initial Location Estimation and Bounding . . . . .	90
4.4 Step 2D: Initial Size Estimation and Bounding . . . . .	94
4.5 Step 2E: Initial Orientation Estimation and Bounding . . . . .	98
4.6 Step 2F: Shape Type Check . . . . .	101
V. Dictionary Formation and Dictionary Search . . . . .	104
5.1 Dictionary Formation . . . . .	104
5.2 Dictionary Search . . . . .	107
5.2.1 Dictionary Results Summary . . . . .	115
VI. Conclusions and Future Work . . . . .	117
6.1 Objectives and Methodology . . . . .	117
6.2 Results and Conclusions . . . . .	118
6.3 Future Work . . . . .	119
6.3.1 Flight Path and System Analysis . . . . .	119
6.3.2 Shape Choice and Parameter Estimation . . . . .	120
Appendix A: Grazing Angle and Tilt Angle Derivations . . . . .	121
Appendix B: Additional Results . . . . .	123
Bibliography . . . . .	136



## List of Figures

Figure	Page
1.1 Six canonical shapes for target identification. . . . .	2
1.2 Demonstrative grouping of canonical shapes that represent a target. . . . .	2
1.3 Canonical shape estimation algorithm overall steps. . . . .	4
2.1 2-D Layover explanatory figure. . . . .	8
2.2 3-D layover explanatory figure. . . . .	9
3.1 Step 1 process flow diagram. . . . .	20
3.2 Sphere $x - y$ plane and $z$ offsets due to the radius. . . . .	23
3.3 Cylinder $x$ and $z$ offsets due to the radius. . . . .	24
3.4 Top-hat $x - y$ plane offset geometry due to the radius. . . . .	25
3.5 Thesis flight path partitions in azimuth and elevation. . . . .	29
3.6 Plate 1 location estimates and errors. . . . .	36
3.7 Plate 2 location estimates and errors. . . . .	37
3.8 Dihedral location estimates and errors. . . . .	38
3.9 Trihedral location estimates and errors. . . . .	39
3.10 Sphere location and radius estimates and errors. . . . .	40
3.11 Cylinder location and radius estimates and errors. . . . .	41
3.12 Top-hat location and radius estimates and errors. . . . .	42
3.13 Graphical depiction of the 3-D location error bound calculations. . . . .	44
3.14 Plate length estimates and errors. . . . .	47
3.15 Dihedral length estimates and errors. . . . .	47
3.16 Cylinder length estimates and errors. . . . .	48
3.17 Length increase with skew orientation. . . . .	49
3.18 The length and height parameter bound calculation shown graphically. . . . .	50

Figure	Page
3.19 Plate height estimates and errors. . . . .	52
3.20 Dihedral height estimates and errors. . . . .	52
3.21 Trihedral height estimates and errors. . . . .	53
3.22 Top-hat height estimates and errors. . . . .	53
3.23 Top-hat true radius and apparent radius orientation dependence. . . . .	54
3.24 Scenario 1 2-D SAR images. . . . .	61
3.25 Scenario 1 segment masks for the 2-D SAR images. . . . .	62
3.26 Scenario 2 Case 1 2-D SAR images. . . . .	63
3.27 Scenario 2 Case 1 segment masks for the 2-D SAR images. . . . .	64
3.28 Scenario 2 Case 2 2-D SAR images. . . . .	65
3.29 Scenario 2 Case 2 segment masks for the 2-D SAR images. . . . .	66
3.30 Scenario 2 Case 3 2-D SAR images. . . . .	67
3.31 Scenario 2 Case 3 segment masks for the 2-D SAR images. . . . .	68
3.32 Scenario 2 Case 4 2-D SAR images. . . . .	69
3.33 Scenario 2 Case 4 segment masks for the 2-D SAR images. . . . .	70
3.34 Scenario 3 2-D SAR images. . . . .	71
3.35 Scenario 3 segment masks for the 2-D SAR images. . . . .	72
3.36 Peak association layover example. . . . .	80
4.1 Parameter estimation and bounding flow diagram. . . . .	81
4.2 Scenario 1 SPLIT shape type estimate and polarization bounce image. . . . .	86
4.3 Scenario 2 SPLIT shape type estimates and polarization bounce images. . . . .	87
4.4 Scenario 3 SPLIT shape type estimates and polarization bounce image. . . . .	88
5.1 Dictionary formation and search flow diagram. . . . .	104
5.2 Full dictionary redundancy. . . . .	108
5.3 Molecule dictionary with reduced coherency. . . . .	108

Figure	Page
5.4 Scenario 1 chosen plate and trihedral PHs. . . . .	111
A.1 Slant Plane Coordinate System. . . . .	121
A.2 Cross product geometry for $\hat{z}$ . . . . .	122

## List of Tables

Table	Page
2.1 Richards' 3-D parameter estimation steps. . . . .	12
2.2 Applicable parameters for each shape type. . . . .	14
2.3 3-D scatterer model polarization bounces and amplitude response equations. . .	14
2.4 Distance from the scene center due to the radius parameter, $\Delta R_r$ . . . . .	15
3.1 Flight path azimuth and elevation ranges. . . . .	28
3.2 Grazing angles and tilt angles. . . . .	28
3.3 Thesis flight paths used to estimate each shape parameter set. . . . .	30
3.4 Simulated Radar Operating Parameters. . . . .	32
3.5 Representative parameter set orientation angles. . . . .	34
3.6 Representative parameter set for location error analysis. . . . .	35
3.7 Representative parameter set for size error analysis. . . . .	45
3.8 Length estimate segment thresholds. . . . .	46
3.9 Height solutions to the RCS equations. . . . .	51
3.10 Orientation Monte Carlo Parameter for Error Estimation. . . . .	55
3.11 Orientation Monte Carlo results. . . . .	56
3.12 Orientation $3\sigma$ error values for parameter bounding. . . . .	57
3.13 Scenario 1 plate parameters. . . . .	60
3.14 Scenario 2 plate parameters. . . . .	60
3.15 Scenario 3 scatterer parameters. . . . .	60
3.16 Scenario 1 2-D image peak locations. . . . .	74
3.17 Scenario 2 Cases 1-4 2-D image peak locations. . . . .	75
3.18 Scenario 3 2-D image peak locations. . . . .	76
4.1 Frequency response $\alpha$ values. . . . .	85

Table	Page
4.2 SPLIT shape type estimates. . . . .	89
4.3 Scenario 1 scatterer shape true parameters, parameter estimates, and shape check. . . . .	91
4.4 Scenario 2 scatterer shape true parameters, parameter estimates, and shape check. . . . .	92
4.5 Scenario 3 scatterer shape true parameters, parameter estimates, and shape check. . . . .	93
4.6 Peak radar cross-section (RCS) equations for each shape. . . . .	95
4.7 Shape true peak RCS values and measured RCS from the HRRs. . . . .	95
4.8 Information used to determine the size parameter for each shape type . . . . .	96
4.9 Pseudo-code for orientation angle coarse-to-fine parameter estimation. . . . .	99
4.10 Orientation estimation coarse-to-fine sample numbers. . . . .	100
5.1 Parameter estimate sampling size. . . . .	105
5.2 Scenario 1 scatterer shape true parameters, parameter estimates, and shape coherency check. . . . .	110
5.3 Scenario 2 scatterer shape true parameters, parameter estimates, and shape coherency check. . . . .	112
5.4 Scenario 2 Case 4 $\Delta R$ consistency check. . . . .	112
5.5 Scenario 3 scatterer shape true parameters, parameter estimates, and shape coherency check. . . . .	114
5.6 Scenario 2 Case 4 $\Delta R$ consistency check. . . . .	115
B.1 Scenario 1 plate SPLIT shape type estimates. . . . .	123
B.2 Scenario 1 plate shape check. . . . .	124
B.3 Scenario 1 plate scatterer shape true parameters, parameter estimates, and shape check. . . . .	124
B.4 Scenario 1 dihedral SPLIT shape type estimates. . . . .	125
B.5 Scenario 1 dihedral shape check. . . . .	125
B.6 Scenario 1 dihedral true parameters and parameter estimates. . . . .	125

Table	Page
B.7 Scenario 1 trihedral SPLIT shape type estimates. . . . .	126
B.8 Scenario 1 trihedral shape check. . . . .	126
B.9 Scenario 1 trihedral true parameters and parameter estimates. . . . .	126
B.10 Scenario 1 sphere SPLIT shape type estimates. . . . .	127
B.11 Scenario 1 sphere initial and final shape type estimates. . . . .	127
B.12 Scenario 1 sphere true parameters and parameter estimates. . . . .	127
B.13 Scenario 1 cylinder SPLIT shape type estimates. . . . .	128
B.14 Scenario 1 cylinder initial and final shape type estimates. . . . .	128
B.15 Scenario 1 cylinder true parameters and parameter estimates. . . . .	128
B.16 Scenario 1 dihedral SPLIT shape type estimates. . . . .	129
B.17 Scenario 1 top-hat initial and final shape type estimates. . . . .	129
B.18 Scenario 1 top-hat true parameters and parameter estimates. . . . .	129
B.19 Scenario 2 plate SPLIT shape type estimates and shape type check. . . . .	130
B.20 Scenario 2 plate shape true parameters, parameter estimates, and coherency shape check. . . . .	131
B.21 Scenario 2 dihedral SPLIT shape type estimates and shape type check. . . . .	131
B.22 Scenario 2 dihedral shape true parameters, parameter estimates, and coherency shape check. . . . .	132
B.23 Scenario 2 trihedral SPLIT shape type estimates and shape type check. . . . .	132
B.24 Scenario 2 trihedral shape true parameters, parameter estimates, and coherency shape check. . . . .	132
B.25 Scenario 2 sphere shape estimates. . . . .	133
B.26 Scenario 2 sphere shape true parameters, parameter estimates, and coherency shape check. . . . .	133
B.27 Scenario 2 cylinder shape estimates. . . . .	133

Table	Page
B.28 Scenario 2 cylinder shape true parameters, parameter estimates, and coherency shape check. . . . .	134
B.29 Scenario 2 top-hat SPLIT shape type estimates and shape type check. . . . .	134
B.30 Scenario 2 top-hat shape true parameters, parameter estimates, and coherency shape check. . . . .	134

## List of Symbols

Symbol	Definition
$a$	atom phase history vector (dimensionless)
$b$	image amplitude (W)
$B$	bandwidth (Hz)
$c$	speed of light (m/s)
$C$	number of coherency matches
$D$	radar diameter (m)
$E$	scene extent (m)
$f$	frequency (Hz)
$g$	HRR amplitude
$G$	spatial frequency amplitude
$H$	object height parameter (m)
$J$	number of shape types
$k$	wavenumber (1/m)
$K$	number of data samples in a flight path
$L$	object length parameter (m)
$mol$	molecule phase history vector (dimensionless)
$M$	phase history (complex number)
$N$	number of atoms
$p(\cdot)$	probability
$Q$	number of shape parameters
$r$	object radius parameter (m)
$\Delta R$	radar range from scene center (m)
$s$	modeled radar return signal (V)



Symbol	Definition
$S$	number of samples per parameter (dimensionless)
$u$	spatial range (m)
$U$	spatial frequency ( $\text{m}^{-1}$ )
$v$	specular pointing vector
$w$	dictionary coefficients
$x$	object x parameter (m)
$x_g$	x location in image ground plane (m)
$\bar{x}$	center of mass (m)
$\hat{x}$	x location in 2-D image for the 2-D scattering models
$y$	object y parameter (m)
$y_g$	y location in image ground plane (m)
$\hat{y}$	y location in 2-D image for the 2-D scattering models
$Y$	observed data vector
$z$	object z parameter (m)
$\alpha$	image locations vector (m)
$\beta$	polarization matrix type
$\chi$	2-D to 3-D transfer function (dimensionless)
$\delta$	sample step size
$\delta(\cdot)$	delta function
$\Delta$	extent of a variable
$\eta$	slant plane tilt angle (radians or degrees)
$\gamma$	object roll parameter (radians or degrees)
$\tilde{\gamma}$	scattering aspect dependence parameter (dimensionless)
$\Gamma$	shape type
$\theta$	object pitch parameter (radians or degrees)

Symbol	Definition
$\tilde{\theta}$	elevation angle of the radar (radians or degrees)
$\Theta$	model parameters
$\lambda$	wavelength (m)
$\Lambda$	radar location in azimuth and elevation
$\mu$	mean (m or radians/degrees)
$\nu$	location estimate vector (m)
$\omega$	frequency (radians)
$\phi$	object yaw parameter (radians or degrees)
$\tilde{\phi}$	azimuth angle of the radar (radians or degrees)
$\Phi$	object parameter vector (m and radians/degrees)
$\psi$	slant plane grazing angle (radians or degrees)
$\sigma$	standard deviation (m or radians/degrees)
$\Sigma$	covariance matrix
$\tau$	time (s)
$\lfloor$	round down (floor)
$\lceil$	round up (ceiling)

### *Subscripts*

$c$	center
$g$	image ground plane
$i, j, q$	counting indices
$m$	shape index
$p$	projection
$pt$	point scatterer
$r$	radius

Symbol	Definition
--------	------------

$m$	object index in a given scene
-----	-------------------------------

$0$	scene center
-----	--------------

### *Superscripts*

$-1$	inverse operator
------	------------------

$h$	horizontal polarization
-----	-------------------------

$H$	Hermitian operator
-----	--------------------

$T$	transpose operator
-----	--------------------

$v$	vertical polarization
-----	-----------------------

$\dagger$	Moore-Penrose pseudoinverse
-----------	-----------------------------

## List of Acronyms

Acronym	Definition
1-D	one-dimensional
2-D	two-dimensional
3-D	three-dimensional
ATR	Automatic target recognition
BP	basis pursuit
BPDN	basis pursuit denoising
EM	electro-magnetic
FT	Fourier transform
GO	geometric optics
GTD	Geometric Theory of Diffraction
HRR	high range resolution
IFFT	inverse fast Fourier transform
IFT	inverse Fourier transform
LS	least-squares
MF	matched filter
ML	maximum likelihood
PH	phase history
RCS	radar cross-section
SAR	synthetic aperture radar
SINR	signal-to-noise-plus-interference ratio
SPLIT	spectrum parted linked image test

# IMPROVED DICTIONARY FORMATION AND SEARCH FOR SYNTHETIC APERTURE RADAR CANONICAL SHAPE FEATURE EXTRACTION

## I. Introduction

Parameterized scattering models for radar returns from target objects provide an efficient way to describe a scene. This thesis utilizes a three-dimensional (3-D) scattering model [1] to survey a scene. Observed radar returns are processed to estimated target parameters in a scene. This thesis decreases the estimation calculations needed in [1] using dictionary search from [2]. This thesis improves parameter estimation accuracy relative to [2] with parameter initialization and bounding.

### 1.1 Problem Statement

SAR data provides all-weather, 24-hour target sensing capability. Analysts are not able to keep up with the volume of captured data collections. ATR algorithms pre-process data to point analysts to collections of interest.

Canonical shapes provide a compact way of representing a target. The canonical shapes from [1] are shown in Figure 1.1. A notional example of a target and its canonical shape representation is shown in Figure 1.2 [3]. Detecting canonical shape scatterers in a scene and estimating their parameters provide inputs for ATR algorithms. This thesis aids SAR ATR by accurately detecting and estimating canonical shapes within radar SAR data.

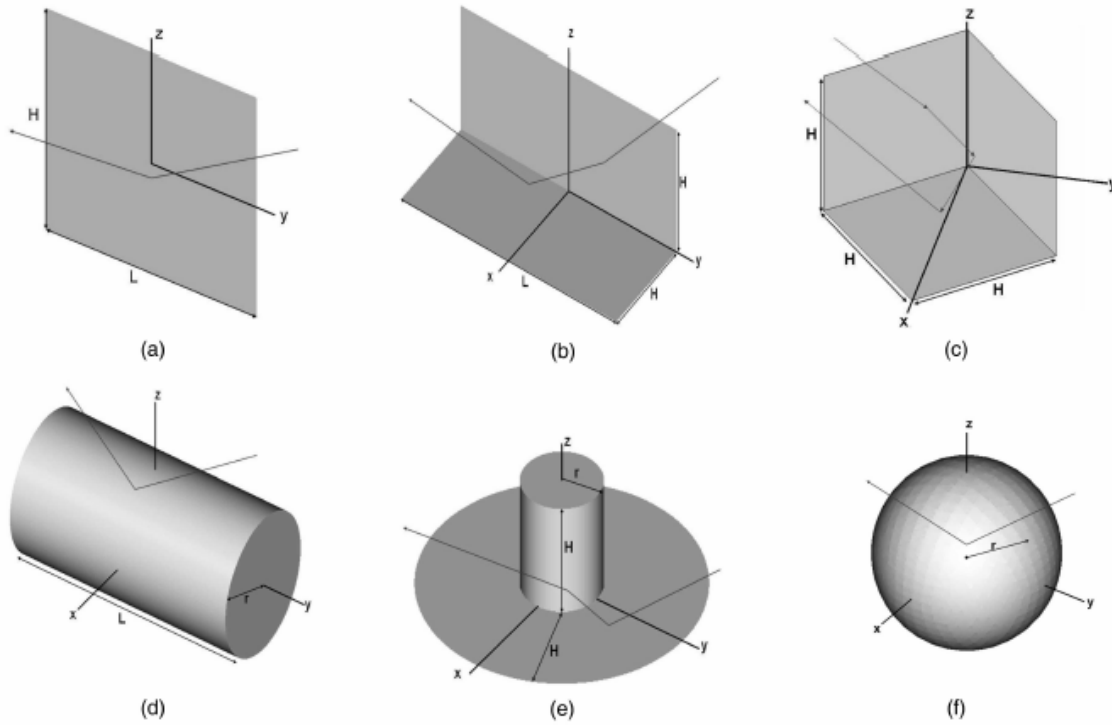


Figure 1.1: Six canonical shapes for target identification [1]. The shapes are a (a) plate, (b) dihedral, (c) trihedral, (d) cylinder, (e) top-hat, and (f) sphere.



Figure 1.2: Demonstrative grouping of canonical shapes that represent a target [3, 4].

## 1.2 State of the art

Parameterized scatterer models have progressed from isotropic point scatterers to two-dimensional (2-D) scattering models [5–10] to 3-D models [1–3, 11, 12]. The parameterized models derived in [1] involve all aspects of shape geometry. These models account for the object location, size, and orientation, and the collection geometry of the radar.

The models from [1] are highly non-linear. Estimating the parameters directly using a numeric solver can cause large errors without very accurate initial estimates. Dictionary formation and search using a least-squares (LS) match between dictionary entries and the observed data can make estimation tractable, as the discretized dictionary provides a finite number of parameters to check. Limiting the finite set of parameters allows for fast formation and search. The speed of search is improved over gradient descent methods due to the finite set. Dictionary search was researched using a coarse dictionary sampling [2]. This coarse sampling can lead to large estimation errors due to local minima in the cost function across the parameter subspace. Attempting to sample the entire parameter subspace with fine resolution is limited by memory constraints. This thesis improves the dictionary method bounding the parameter subspace using initial estimates and error analysis prior to sampling. For the same memory constraints with a smaller parameter subspace, finer parameter sampling is accomplished near the true values. The local minima far from the true parameter values from coarse sampling the entire subspace are eliminated.

### **1.3 Objectives and Methodology**

The primary objective of this research is to develop an improved dictionary formation and search algorithm to obtain more accurate scatterer parameter estimates relative to [2]. The supporting objectives are to increase the accuracy of the estimates and to decrease the number of computations. To improve accuracy, initial parameter estimates are made and parameter error analysis is performed to limit the searchable parameter subspace. The limited subspace allows for finer sampling, so final estimates are more accurate. The dictionary method decreases the number of computations relative to gradient descent from [1]. The bound parameter subspace decreases computation by limiting the number of dictionary entries.

An overview of the full algorithm to detect and estimate the scatterers in a scene is provided in Figure 1.3.

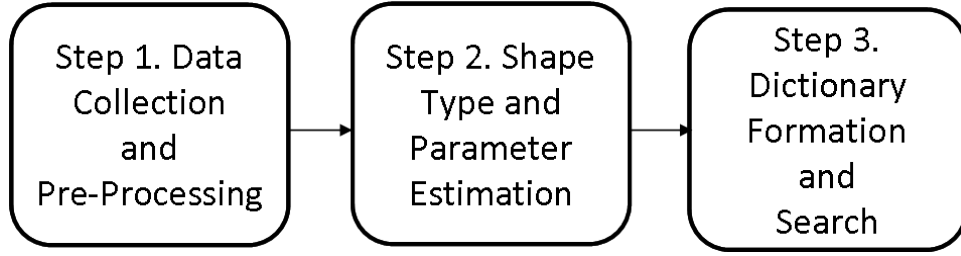


Figure 1.3: Canonical shape estimation algorithm overall steps.

In Step 1 the radar return data is collected. The data collection parameters are analyzed to pre-process the minimum and maximum possible errors. The collected data is processed to form a images and detect scatterers in the scene. Section 2.1 provides the details of how 2-D SAR images are produced.

Step 2 makes initial parameter estimates. The location initialization uses the location of the scatterers in multiple images formed from the SAR data. The size initialization uses the length of the scatterer detected in the image, the location and radius relation on a 2-D image, and the amplitude of the return. The orientation initialization uses a coarse-to-fine dictionary formation and coherency match. Error analysis for each parameter based on the collection flight path determines an upper and lower bound for each parameter. The parameter bounds limit the dictionary sampling range for each scatterer.

Finally in Step 3, the dictionary is formed by sampling each parameter within the bounds from Step 2. A two stage dictionary search using normalized maximum coherency and LS cost relative to the observed PH provides the final estimate of parameters for each shape.

## 1.4 Thesis Chapters

The thesis is organized by chapters. Chapter 2 is the literature review that provides a technical overview of radar data collection, radar data analysis, and conversion of radar data to 2-D SAR images. After the technical overview, parameterized scatter models used for



efficient target identification are provided. Estimation techniques of the model parameter rounds out the chapter.

Chapters 3, 4, and 5 walk through the steps to make final parameter estimates. Each chapter addresses one of the three Steps from Figure 1.3. The Step's methodology is addressed first. To evaluate the methodology, each chapter includes results for specified cases.

Chapter 3 addresses Step 1, data collection and pre-processing. The known collection flight path and radar parameters are analyzed. The collection parameters are used to determine the minimum and maximum error possible because the target shapes are not known a priori. The data is collected and processed using 2-D SAR image formation.

Chapter 4 details how Step 2 makes the initial estimate of the shape type and parameters of each canonical shape in a scene. Each shape has parameters of 3-D location, size, and orientation. The initial estimates are combined with the error analysis from Step 1 to provide possible ranges of each parameter used in Step 3 for dictionary formation.

Chapter 5 shows how the parameter ranges are sampled to form dictionaries. Dictionary entry uniqueness is evaluated using Gram matrices. A Gram matrix shows the level of coherency in a dictionary by taking the inner product of each entry with the others ( $D^H D$ ). The dictionary search is accomplished using maximum coherency and LS comparison. The algorithm is assessed based on the final shape type choice and final parameter estimate accuracies.

Chapter 6 is the conclusion and future works. The data-based findings from the thesis are summarized, and logical extensions of this work are presented.

## II. Background

This chapter presents background information regarding radar processing and outlines specific radar scattering models. Section 2.1 gives a technical overview to describe the data received by a radar, how the data is manipulated for analysis, and how a synthetic aperture is formed from multiple pulses and is used for image formation.

Radar return parameterized scatterer models describe mathematically expected radar return values. Section 2.2 describes the many parameter models derived for scatterer radar returns. When using models for ATR, the parameters are not known a priori. Therefore, a model is effective only if the parameters are determined from the received radar data.

The last scatterer model of this chapter is the 3-D model derived by Jackson [1]. Hammond estimates the model parameters with dictionary formation and search [2, 3]. This thesis improves the dictionary search to achieve more accurate parameter estimates.

### 2.1 Technical Overview

A radar transmits a pulse of energy and receives returns from all scatterers in a scene. The return is sampled in time and captures the amplitude and phase of the return. The return data is then converted from the time domain to spatial frequency. When multiple pulses from different geometries are converted to the spatial frequency domain and combined, the combined set is called PH data.

To convert to PH, the return data is sampled and matched filtered using the transmitted waveform. The matched filter (MF) output is transformed into the spatial frequency domain. The result is the scene PH. In this thesis, the PH is generated directly from the model equations, so these steps are not utilized.

The PH data is used to get accurate range measurements of the scatterers in the scene. Taking the inverse fast Fourier transform (IFFT) of the PH (spatial frequency)

outputs the range measurements of the scatterers. The range measurement is called a high range resolution (HRR) profile. An HRR of a single pulse provides one-dimensional (1-D) information in range. Scatterers are ambiguous in cross-range, which is perpendicular to the radar pointing direction. From a given azimuth direction,  $\tilde{\phi}$ , the HRR is expressed as  $g_p(u, \tilde{\phi})$ , where  $u$  is the spatial range location and  $g_p$  is the amplitude of the return.

SAR combines spatially separated radar returns to synthetically produce an aperture larger than the aperture of the physical radar. Each radar location provides an HRR measurement. Multiple HRRs collected along a flight path can be combined to produce an image [13]. One method to produce a 2-D image of the combined HRRs is called backprojection. Backprojection under the far field assumption is expressed as [13, 14]

$$b(x_g, y_g) = \int_{\tilde{\phi}_1}^{\tilde{\phi}_2} \left\{ \int_{-\infty}^{\infty} |U| G_p(U, \tilde{\phi}) e^{j2\pi U u} dU \right\} d\tilde{\phi}. \quad (2.1)$$

The amplitude of the scatterers in the ground plane for the 2-D image is  $b(x_g, y_g)$ , where  $x_g$  is the location in the  $x$  or range direction, and  $y_g$  is the location in the  $y$  or cross-range direction. The inner integral is the inverse Fourier transform (IFT) of  $|U| G_p(U, \tilde{\phi})$ , where  $|U|$  is the radar frequency, and  $G_p(U, \tilde{\phi})$  is the Fourier transform (FT) of the projection data  $g_p(u, \tilde{\phi})$ .

The FT and IFT are subject to aliasing depending on the sample step size [15]. The size of the image where no aliasing occurs is called the scene extent. The sampling in frequency affects the range extent and the sampling in azimuth affects the cross-range scene extent. The range scene extent is

$$E_{range} = \frac{c}{2\delta f}, \quad (2.2)$$

where  $c$  is the speed of light, and  $\delta f$  is the frequency sampling step size. In the cross-range direction, the scene extent is

$$E_{cross-range} = \frac{\lambda_{min}}{2\delta\tilde{\phi}}, \quad (2.3)$$

where  $\lambda_{min}$  is the minimum wavelength of the radar, and  $\delta\tilde{\phi}$  is the azimuth sampling step size.

Equation (2.1) produces a 2-D image integrating over azimuth angles and spatial frequency. The collection geometry includes elevation,  $\tilde{\theta}$ . Scatterers not in the ground or image plane are projected into the image plane based on the angle or slant plane that the flight path makes with the ground plane. This phenomena is called layover [13]. The projection is perpendicular to the slant plane formed from the flight path due to the planar wavefront assumption. Figure 2.1 shows a simplified model of how layover works. The red target is projected perpendicular to the radar slant plane. The range to the scatterer and projected location in the 2-D image ground plane are equivalent.

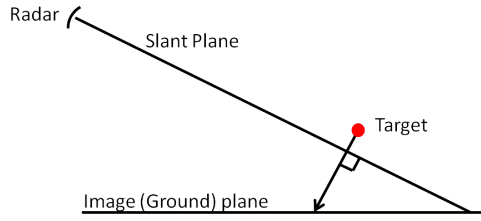


Figure 2.1: 2-D Layover example figure. The range to the scatterer and the projected point on the image plane are equivalent under a far field assumption.

When the flight path varies in azimuth and elevation, the resulting layover projection has layover in the range and cross-range directions [13]. Figure 2.2 shows a descending flight path. The grazing angle caused by the azimuth still projects the target closer to the radar in the range direction. The descent in flight path causes a tilt angle in the slant plane that causes a shift in the cross-range direction when the target is projected. Therefore, the resultant projection vector moves the target location in range and cross-range.

The layover projection angles in range and cross-range for 2-D SAR image formation are dependent on flight path. This thesis utilizes the unique layover projections between 2-D images produced from different flight paths to estimate the 3-D location of scatterers. The details of the location estimation are provided in Section 4.3.

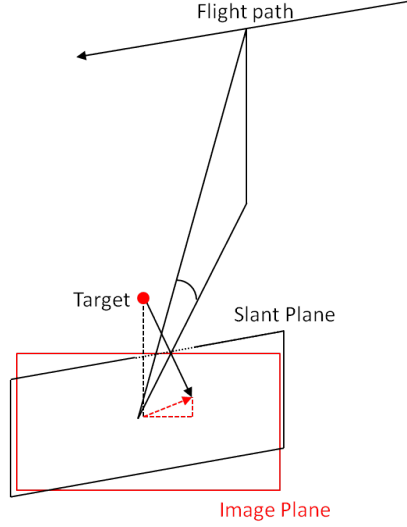


Figure 2.2: 3-D Layover example figure. The projected scattered has layover in both the range and cross-range directions.

One factor affecting the accuracy of the 3-D location estimate is the accuracy of the 2-D location estimate in each image. The 2-D location accuracy is determined by the resolution. Resolution in the range direction for SAR images is determined by bandwidth with  $\text{resolution}_{\text{range}} = \frac{c}{2B}$ , where  $B$  is the radar bandwidth. Resolution in the cross-range resolution is determined by azimuth extent of the flight path using  $\text{resolution}_{\text{cross-range}} = \frac{\lambda}{2\Delta\phi}$ , where  $\lambda$  is the wavelength at the center frequency and  $\Delta\phi$  is the flight path azimuth extent.

## 2.2 Scattering Parametric Models

Each parametric scattering model involves utilization of SAR data. The diversity in frequency and location combine to make location estimates. Historically, each scatterer in a target scene is treated as an isotropic point scatterer. Mathematically, point scatterers are most straight forward, as each is treated as a delta function. The scatterer,  $g_{pt}$ , is described mathematically using its location,  $(x, y, z)$ , and amplitude,  $A$ , by [16]

$$g_{pt}(x, y, z) = A\delta(x, y, z).$$

The point target model is limited because the reflections from an extended object are aspect dependent. The resultant reflection is not isotropic. The orientation of true objects varies the amplitude of a scatterer depending on the collection geometry. The object orientation is not captured by the point scatterer model.

Models are created in [5–8] to account for the physical size and orientation of scatterers. 2-D parameter scattering models [5–8] were first introduced to aid object identification in 2-D images. The location, size, and probable azimuth angle of scatterers are estimated relative to the 2-D image scene. 3-D parameter scattering models [1, 17, 18] utilize the full object geometry of objects. The 3-D models includes details regarding the true 3-D position of an object, the estimated size, and 3-D pose angle of objects.

### 2.2.1 2-D Scattering Models.

Two-dimensional scattering model parameter initial estimation uses 2-D images. The initial estimates are the initialization points for each parameter. The 2-D parameterized model investigated in [5–10] is expressed as

$$s(\omega, \tilde{\phi}; \Theta) = \sum_m A_m \left( j \frac{\omega}{\omega_c} \right)^{\alpha_m} \text{sinc} \left( \frac{\omega}{c} L_m \sin(\tilde{\phi} - \tilde{\phi}_m) \right) e^{-\omega \tilde{\gamma}_m \sin \tilde{\phi}} e^{j \frac{\omega}{c^2} (\hat{x}_m \cos \tilde{\phi} + \hat{y}_m \sin \tilde{\phi})}, \quad (2.4)$$

where  $s$  is the modeled receive PH signal;  $q$  is a counting index for each scatterer;  $A$  is the amplitude;  $\omega$  is the frequency where  $\omega = 2\pi f$  and  $\omega_c$  is the center frequency;  $\alpha$  determines the shape frequency dependence;  $L$  is the length;  $\tilde{\phi}$  is the azimuth angle of the radar and  $\tilde{\phi}_q$  is the azimuth pointing angle for each scatterer;  $\tilde{\gamma}$  is the scattering aspect dependence parameter; and  $\hat{x}_q$  and  $\hat{y}_q$  are the  $x$  and  $y$  locations in the image for each scatterer. The variable  $\Theta$  represents all the unknown scatterer parameters. The sum over each scatterer denotes that the total received signal is the sum of the individual responses, a valid approximation when  $\lambda \ll \text{object size}$ .

Automated algorithms to determine the parameters for each scatterer use initial estimates and iterative minimization of a cost function. Different approaches are taken in

the various publications [5–10]. All utilize the image domain to initialize the 2-D location and size parameter.

[5–7], and [10] use maximum likelihood (ML) along with the maximum image pixels to initialize parameters. The ML is conditioned such that the parameters produce the same maximum pixel locations as the image. The comparison eliminates the majority of the parameters allowing for a confined initial estimate. The ML formulation for the signal in noise is

$$\hat{\Theta}_{ML} = \arg \min_{\Theta} [Y - s(\Theta)]^H \Sigma^\dagger [Y - s(\Theta)], \quad (2.5)$$

where  $Y$  is the observed data;  $s(\Theta)$  is a simplified representation of the received  $s(\omega, \tilde{\phi}; \Theta)$ ; the superscript  $H$  is the Hermitian operator;  $\Sigma$  is the covariance matrix of the noise; and  $(\cdot)^\dagger$  denotes the Moore-Penrose pseudoinverse.

In [8], the parameters per scatterer are estimated, and the resultant images are created. The images are summed and compared to the SAR image to determine the best fit. This method is computationally inefficient as image formation and comparison takes longer than comparing PH data directly.

Overall, 2-D scattering models give insight into the response of scatterers projected onto a 2-D image plane. The limitation of these methods is that the output does not give the full physical geometry of the scatterers. The scatterer pose angle is not limited to an azimuth direction. The location of a scatterer can be above the ground plane. To parameterize the full geometry of a scatterer, a 3-D model is needed.

### **2.2.2 3-D Scattering Models.**

Early parameter estimation in 3-D is done using canonical shape model equations in [17, 18]. The parameters of each shape are given:  $\Theta_i = [\Theta_i^t, \Theta_i^x, \Theta_i^a, \Theta_i^p, \Theta_i^r]$ , where  $\Theta_i^t$  is the shape type;  $\Theta_i^x$  is the 3-D location;  $\Theta_i^a$  corresponds to the maximum RCS;  $\Theta_i^p$  is the pose angle; and  $\Theta_i^r$  is the radius of curvature. RCS is the apparent size of a target detected by a radar in units of  $\text{m}^2$  [19].

Each parameter is estimated through iterative ML estimation according to [17, Section 4.1]

$$\hat{\Theta}_{ML} = \arg \max_{\Theta} \log p(Y|\Theta), \quad (2.6)$$

where  $Y$  is the observed returns, and  $p(\cdot)$  is the probability of the given quantity. At each iteration, a new 2-D SAR image is formed, and the parameters estimates are updated. To decrease computation, the parameters are estimated in steps per iteration. The expectation maximization steps are in Table 2.1.

Table 2.1: The iterative steps for Richards' expectation-maximization to estimate 3-D parameters [18].

1. Form an image of the scene from an arbitrary flight path.
2. Use ML to estimate the pose angle. The amplitude, location and radius fixed.
3. Use ML to estimate the amplitude. The location and radius fixed.
4. Use ML to estimate the location and radius.

The pose angle in Richards' model consists of an azimuth and elevation angle of maximum RCS [17]. Using three axial rotations to describe orientation gives more specificity to a shape's orientation. Jackson's 3-D models specify how each parameter affects the scattering response and accounts for all orientations of a shape [1].

Jackson derives 3-D parametric scattering models for canonical shapes in [1, Chapter 3]. The six shapes are shown in Figure 1.1. The models improve on Richard's model by including three angles for orientation to allow all possible shape orientations.

The models are derived using geometric optics (GO) and Geometric Theory of Diffraction (GTD) [20] that describe how electro-magnetic (EM) waves impinging and re-radiating from a flat, right-angle, and circular surfaces. The responses are combined to model each shape's features. The angles of reflection are determined by the orientation of the shape and the location of the radar. The size of the shape determines the width of the response in phase history as well as the amplitude of the return.



In [1] the full bistatic model is derived. This thesis uses the simplified monostatic case and presents the monostatic equations only. The known parameters are  $k$ , the wavenumber  $k = \frac{2\pi f}{c}$ ;  $\Lambda$ , the flight path to include the azimuth and elevation  $\Lambda = (\tilde{\phi}, \tilde{\theta})$ ; and  $P$ , the polarization(s) of the radar that is known only for each shape type. Using high frequency approximations from the GTD [20], the PH model response,  $s$ , is a sum of scattering responses and is given in Equation (2.8). The response can be a single value for a single polarization or up to a 2 x 2 matrix for all polarizations from the polarization matrix

$$P_m(\Lambda; \Theta_m) = \begin{bmatrix} P^{vv} & P^{vh} \\ P^{hv} & P^{vh} \end{bmatrix}, \quad (2.7)$$

where  $v$  and  $h$  represent vertical and horizontal linear polarization, and two of those letters together represent the transmitted and received polarization channels. For odd and even number of bounces, the matrices are

$$P_{\text{odd}}(\Lambda; \Theta_m) = \begin{bmatrix} -1 & 0 \\ 0 & 1 \end{bmatrix}, \text{ and } P_{\text{even}}(\Lambda; \Theta_m) = \begin{bmatrix} -1 & 0 \\ 0 & -1 \end{bmatrix}.$$

The response,  $s$ , is a sum of the responses from each scatterer in the scene described by [1]

$$s(k, \Lambda; \Theta) = \sum_m P_m(\Lambda; \Theta_m) M_{\Gamma_m}(k, \Lambda; \Theta_m) e^{jk\Delta R(\Lambda; \Theta_m)}, \quad (2.8)$$

where  $\Theta$  contains the parameters of each object;  $M_{\Gamma_m}$  is the scattering response given in Table 2.3;  $\Gamma$  is the shape type,  $\Gamma \in [\text{plate, dihedral, trihedral, sphere, cylinder, top-hat}]$ ; and  $\Delta R$  is the distance from scene center.

The parameters for Jackson's 3-D parameter model are  $\Theta = [x, y, z, L, H, r, \gamma, \theta, \phi]$ . The parameters  $x, y$ , and  $z$  are 3-D location of the object;  $L, H$ , and  $r$  are the size parameters of length, height, and radius; and  $\gamma, \theta, \phi$  are the orientation parameters of roll, pitch, and yaw. The applicable parameters for each shape are given in Table 2.2. The scatterer response  $M$  is different for each canonical shape type. Table 2.3 provides each equation.

The size of the shape modulates the amplitude of the response. The amplitude in each equation is denoted with the variable  $A$ , and its equations are also provided in Table 2.3.

Table 2.2: Applicable parameters for each shape type [1].

Shape	x	y	z	L	H	r	$\gamma$	$\theta$	$\phi$
plate	X	X	X	X	X		X	X	X
dihedral	X	X	X	X	X		X	X	X
trihedral	X	X	X		X		X	X	X
sphere	X	X	X			X			
cylinder	X	X	X	X		X	X	X	X
top-hat	X	X	X		X	X	X	X	X

Table 2.3: Odd or even polarization bounces and amplitude response for each shape type [1]. The magnitude of the amplitude is scaled by the shape size and is given with the parameter  $A$ .

Shape	Polarization Bounce	$\mathbf{M}_{\Gamma\mathbf{m}}(\mathbf{k}, \Lambda; \Theta_{\mathbf{m}})$	A
plate	odd	$\frac{jk}{\sqrt{\pi}} A \text{sinc}(kL \sin \tilde{\phi} \cos \tilde{\theta}) \text{sinc}(kH \sin \tilde{\theta}); \tilde{\theta} \in [-\frac{\pi}{2}, \frac{\pi}{2}], \tilde{\phi} \in [-\frac{\pi}{2}, \frac{\pi}{2}]$	LH
dihedral	even	$\frac{jk}{\sqrt{\pi}} A \text{sinc}(kL \sin \tilde{\phi} \cos \tilde{\theta}) \times \begin{cases} \sin \tilde{\theta}; \tilde{\theta} \in [0, \frac{\pi}{4}] \\ \cos \tilde{\theta}; \tilde{\theta} \in [\frac{\pi}{4}, \frac{\pi}{2}] \end{cases}; \tilde{\phi} \in [-\frac{\pi}{2}, \frac{\pi}{2}]$	2LH
trihedral	odd	$\frac{jk}{\sqrt{\pi}} A \times \begin{cases} \sin(\tilde{\theta} + \frac{\pi}{4} - \tan^{-1}(\frac{1}{\sqrt{2}})); \tilde{\theta} \in [0, \tan^{-1}(\frac{1}{\sqrt{2}})] \\ \cos(\tilde{\theta} + \frac{\pi}{4} - \tan^{-1}(\frac{1}{\sqrt{2}})); \tilde{\theta} \in [\tan^{-1}(\frac{1}{\sqrt{2}}), \frac{\pi}{2}] \end{cases} \\ \times \begin{cases} -\cos(\tilde{\phi} - \frac{\pi}{4}); \tilde{\phi} \in [-\frac{\pi}{4}, 0] \\ \sin(\tilde{\phi} - \frac{\pi}{4}); \tilde{\phi} \in [0, \frac{\pi}{4}] \end{cases}$	$2\sqrt{3}H^2$
sphere	odd	$A\sqrt{\pi}; \tilde{\theta} \in [-\frac{\pi}{2}, \frac{\pi}{2}], \tilde{\phi} \in [-\pi, \pi]$	r
cylinder	odd	$A\sqrt{jk} \cos \tilde{\phi} \text{sinc}(kL \sin \tilde{\phi} \cos \tilde{\theta}); \tilde{\theta} \in [-\frac{\pi}{2}, \frac{\pi}{2}], \tilde{\phi} \in [-\frac{\pi}{2}, \frac{\pi}{2}]$	$L\sqrt{r}$
top-hat	even	$A\sqrt{jk} \times \begin{cases} \sin \tilde{\theta}; \tilde{\theta} \in [0, \frac{\pi}{4}] \\ \cos \tilde{\theta}; \tilde{\theta} \in [\frac{\pi}{4}, \frac{\pi}{2}] \end{cases}; \tilde{\phi} \in [-\pi, \pi]$	$\sqrt{\frac{8r}{\sqrt{2}}}H$

The distance from scene center,  $\Delta R$ , is a function of the shape center location and shape radius, where applicable. The combined relation is

$$\Delta R = \Delta R_0 + \Delta R_r, \quad (2.9)$$

where  $\Delta R_0 = 2(x \cos(\tilde{\theta}) \cos(\tilde{\phi}) + y \cos(\tilde{\theta}) \sin(\tilde{\phi}) + z \sin(\tilde{\theta}))$  for an object centered at  $(x, y, z)$ , and  $\Delta R_r$  is the additional distance to the surface of the object from the object center. The equations for  $\Delta R_r$  are in Table 2.4 (from [1, Section 3.4]).

Table 2.4: Distance from the scene center due to the radius parameter of the sphere, cylinder, and top-hat [1]. The radius vector is added to the distance from scene center due to the location of the object from scene center,  $\Delta R_0$ .

Shape	$\Delta R_r$
sphere	$2r$
cylinder	$2r \cos \tilde{\phi}$
top-hat	$2r \cos \tilde{\theta}$

In [1], the parameters are estimated from the PH data collected over a multiple passes around the scene. Location and size are initiated from a regularized 3-D image formed from sparsity-constrained imaging techniques from [21–23]. After initialization, each parameter is estimated using gradient descent. The gradient descent uses the LS solution [1, Chapter 5]

$$\hat{\Theta}_m = \arg \min_{\Theta_m} \|Y - s(\Theta_m)\|^2, \quad (2.10)$$

where  $Y$  is the observed data,  $s$  is the expected return response given parameters  $\Theta_m$  from Equation (2.8). The subscript  $m$  represents the scatterer index. Accurate results are obtained from the gradient descent estimation subject to good initialization. The long flight path captures a very large amount of PH data. The large data set requires more computation than from a short flight path.

This thesis follows from the work done by Hammond [2, 3] using the scattering models derived in [1]. [2] decreases parameter estimation computations in two ways. A smaller flight path is used that requires less data generation. And clustered dictionaries of PHs are pre-allocated for each shape so parameter estimation is done on a finite set of parameters. This thesis utilizes the work from [2] by limiting the flight path relative to [1] with an order of magnitude less samples. This thesis also creates PH dictionaries using permutations of samples shape parameters as done in [2].

A dictionary is a set of PHs and each entry is referred to as “atom”. Each atom is produced using the 3-D SAR models from [1]. The parameter set of each atom is a unique permutation of the sampled individual parameters. An atom is formed for each parameter permutation and requires large memory for even small sampling. The large dictionary occurs because the number of permutations grows geometrically with the number of samples per parameter.

The dictionary size expression is [2]

$$\text{Memory Required} = \left(8 \frac{\text{bytes}}{\text{sample}}\right) \cdot \left(2K \frac{\text{samples}}{\text{atom}}\right) (N \text{ atoms}), \quad (2.11)$$

where  $K$  is the number of samples per radar pulse, and  $N$  is the number of atoms in a dictionary. The number of samples depends on the azimuth sampling, number of polarizations collected and number of frequency samples. The number of samples is  $K = \# \text{ azimuths} \times \# \text{ polarizations} \times \# \text{ frequencies}$ . Each dictionary atom entry is a complex number so one atom is  $2K$  elements long to account for the real and imaginary components. The number of atoms is expressed as [2]

$$N_{atoms} = \sum_{j=1}^J \prod_{q=1}^Q S_{jq}, \quad (2.12)$$

where  $J$  is the number of shape types included in the dictionary,  $Q$  is the number of parameters per shape type, and  $S$  is the number of samples per parameter.

The large dictionary memory requirement is demonstrated for a plate using Equation (2.11). For a single shape,  $J = 1$ . There are  $Q = 8$  parameters for a plate. The plate dictionary is sampled at 10 locations in  $x, y, z$ , 10 lengths and heights, and 5 orientations in roll, pitch, and yaw, giving  $N_{\text{atoms}} = 1.25 \times 10^7$  atoms. Each atom is sampled at 50 azimuth locations, for a single polarizations, and at 20 frequencies, yielding  $K = 1000$  samples per pulse. Assuming each element uses 8 bytes of memory, the full plate dictionary requires 186 gigabytes of memory.

This thesis improves the sampling approach by estimating and bounding each parameter prior to dictionary formation. Parameter bounds allows for fewer samples per parameter, with finer resolution, thus decreasing the overall number of atoms while improving accuracy of the final estimate.

After initial dictionary formation, [2] decreases estimation search time by first clustering the dictionary atoms into “molecules.” Clustering is done using the coherency between two normalized atoms. If the coherency between two atoms is greater than the coherency limit,  $\eta$ , they are combined into a molecule. Mathematically, the test for coherency is expressed as

$$|\langle \hat{a}_i, \hat{a}_j \rangle| > \eta, \quad (2.13)$$

where  $\hat{a}$  is the normalized PH of an atom.

After the dictionary is formed and clustered, the observed PH is compared to the molecule dictionary using LS. The atom within the chosen molecule is selected using LS. Both the molecule and atom comparisons utilize LS under a sparsity constraint shown in Equation (2.14). The sparsity constraint is applied to find the parameters of multiple shapes in a single scene using

$$\min \|w\|_1 \quad \text{s.t.} \quad \|Y - D_{\Gamma_j} w\|_2^2 < \epsilon, \quad (2.14)$$

where  $D_{\Gamma j}$  is the formed dictionary as a matrix with each column as the atoms,  $Y$  is the observed radar PH,  $w$  is the vector of sparse dictionary coefficients:  $w = [w_1, w_2, \dots, w_N]^T$ , and  $\epsilon$  is the sparsity constraint.

This thesis clusters the dictionary to reduce coherency more efficiently than calculating the coherency between every atom pair. Coherency is calculated using normalized atoms. Atoms with the height parameter only in the amplitude,  $A$ , (dihedral, trihedral, and top-hat) are equal as the height parameter changes. Therefore, all atoms with the same parameters except height are grouped into molecules.

The molecule dictionary is searched using a maximum coherency expressed as

$$\hat{\Theta}_{\text{molecule}} = \arg \max_{\Theta_m} \langle |Y|, |a(\Theta_m)| \rangle, \quad (2.15)$$

where  $a$  represents a molecule. Once the molecule is chosen, the closest atom in that molecule is chosen using a LS approach similar to Equation (2.10). The difference for the dictionary LS is that only the sampled parameter values in the dictionary are searched, so the LS equation replaces the gradient descent signal  $s$  with the dictionary atoms  $a_{\Gamma m}(\Theta_{\Gamma m})$ ,

$$\hat{\Theta}_{\text{atom}} = \arg \min_{\Theta_m} \| |Y| - |a(\Theta_m)| \|_2. \quad (2.16)$$

Overall, this thesis utilizes better parameter scattering models than [17]. The models in [1] account for any orientation. Computation time is decreased from [1] by removing the iterative sparse regularization for the 3-D imaging and gradient descent. The dictionary parameter ranges are smaller than in [2] because initial estimates are made on each parameter. The smaller ranges allow for more precise sampling. Final parameter estimates are more accurate than [2] due to the better sampling. This thesis clusters more efficiently than [2] using the properties of the scattering model.

### 2.3 Background Summary

Chapter 2 provided a technical background for radar operation, including radar returns at amplitude and phase, PH data as the spatial frequency version of the returns, and the HRR

as the precise range measurement. SAR combines radar returns from multiple locations to synthetically produce a large aperture. Backprojection takes SAR data and creates a 2-D image (Equation (2.1)). Objects not in the ground plane in 2-D images are subject to layover due to the geometry of the radar and the projection to a constant range plane.

Parameterized scattering models range from point scattering models to 2-D models to 3-D models. Estimation of the high dimension, non-linear models is non-trivial. Iterative approaches, gradient-descent, and dictionary search all using ML and LS are in current research.

Next, Chapters 3 - 5 provide a an overview of the proposed algorithm and results for parameter estimation for the 3-D scattering model from [1]. The collection flight path and radar parameters are pre-processed to determine the range of possible errors. Multiple techniques are used to make initial estimates. The initial estimates are combined with the pre-processed errors to limit the searchable parameter subspace for dictionary formation. Efficient dictionary clustering, formation, and search provide the final parameter estimates.

### III. Data Collection and Pre-Processing

In Chapter 2 the technical background builds the foundation for radar operation and SAR image formation. The 3-D canonical shape scattering model from [1] is selected for this thesis. The collected data in this thesis are ideal returns generated from the scatterer model equation from Equation (2.8). The planned collection flight path and the radar collection parameters are known prior to a data collect. The shape types and shape parameters are not known a priori. Determining the shapes and their parameters is a detection and estimation problem. Three main steps are used to solve this problem and are detailed in Chapters 3 - 5, respectively.

Chapter 3 details the Step 1 data collection and pre-processing. The steps within Step 1 are in Figure 3.1. The methodology of Steps 1A - 1C are presented in each subsection and can be applied to any radar system. The methodology of Steps 1A - 1C are evaluated using a specific collection flight path and specific radar parameters. The subsections provide the evaluation results after each step of the methodology is explained.

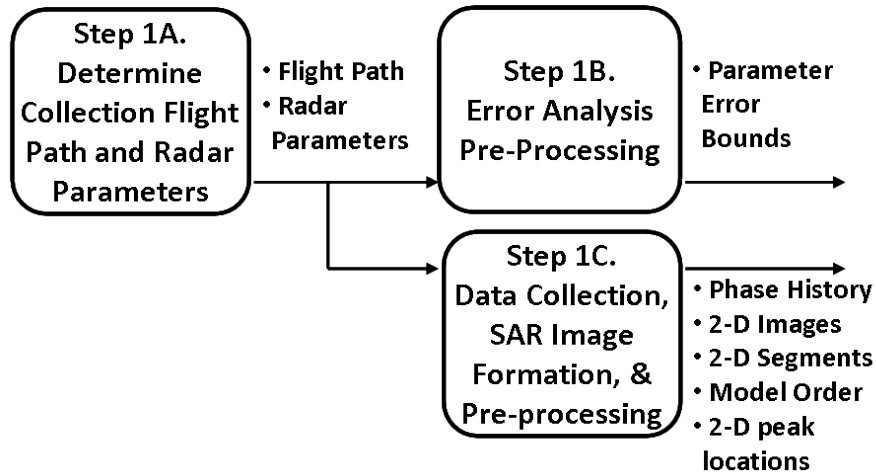


Figure 3.1: Step 1 process flow diagram. A chosen flight path and radar from Step 1A are analyzed to determine the errors that the system can produce in Step 1B pre-processing. If sufficient, in Step 1C the data is collected and pre-processed for Step 2.



Step 1A in Section 3.1 details how flight path diversity in azimuth and elevation is evaluated and discusses how the radar parameters affect the precision of the collected data. Step 1B in Section 3.2 specifies pre-processing of the collection parameters to determine the posterior range of possible errors for parameter estimation used in Step 2. In Step 1C in Section 3.3, the PH data is collected and pre-processed. The pre-processing includes creating and segmenting 2-D SAR images, determining scattering locations in the images, and estimating model order.

### **3.1 Step 1A: Collection Flight Path and Radar Parameters Analysis**

A radar collects PH data that includes amplitude and phase information. Each sample is stored as a complex value where the magnitude is the amplitude and complex angle is the phase. The flown flight path and radar parameters determines the collection angles and number of spatial frequency samples. Data is not available for all aspect angles and spatial frequencies.

Once PH data is collected over a flight path, the path is partitioned into segments with sufficient azimuth and elevation diversity as discussed in Section 3.1.1. The necessary diversity for each shape is explained in Section 3.1.1.1 with mathematic support following in Section 3.1.1.2. The collection flight path to support the needed diversity is discussed in Section 3.1.1.3. A planned collection flight path diversity can be analyzed prior to collection by calculating the grazing and tilt angles for each partition. The grazing and tilt angles affect layover and are discussed prior in Section 2.1.

The radar collection parameters determine the resolution and size of the scene that can be surveyed without aliasing. Section 3.1.2 provides the equations that determine the relationships between radar parameters and collection.

### 3.1.1 Collection Flight Path.

Diversity in the collection flight is necessary to produce a unique PH as discussed in [1, Section 4.1]. The PH of a plate and dihedral, for example, have the same scattering response for a single polarization for a level flight path.

Collection flight path diversity also provides unique layover angles when creating 2-D images from unique partitions of the flight path. The unique layover is needed for 3-D location estimation. An object's 3-D location  $(x, y, z)$  is estimated using 2-D SAR images. The LS mathematic solution for the 3-D location is in Section 3.1.1.2. To understand the unique layover needed for each shape type, shape geometry and associated layover is detailed first.

#### 3.1.1.1 Shape geometry.

The geometry of each shape creates unique layover equations. Shape geometry and flight path affect the location of the return. The flat shapes have the same layover equations because the 3-D location is the center of their peak location in a 2-D image. The shapes with radius are detailed individually since each has unique geometry with the radar return coming away from the shape center.

The locations for the plate, dihedral, and trihedral in the image ground plane,  $(x_g, y_g)$  are specified mathematically equivalently. The range and cross-range 2-D image locations are determined by the 3-D location  $(x, y, z)$  according to [13, Section 2.5]

$$x_g = x + z \tan \psi, \quad (3.1)$$

and

$$y_g = y + z \tan \eta, \quad (3.2)$$

where  $x$  and  $y$  account for the position offset relative to scene center and the second term accounts for layover. The grazing angle  $\psi$  and tilt angle  $\eta$  are the range and cross-range layover angles, respectively.

The radius of the sphere, cylinder, and top-hat move the surface of the object closer to the radar than the center location. The layover equations begin with the terms from the flat shapes to get to the shape center. Two additional terms are added to account for the radius with

$$x_g = (x + \Delta x) + (z + \Delta z) \tan \psi, \quad (3.3)$$

and

$$y_g = (y + \Delta y) + (z + \Delta z) \tan \eta, \quad (3.4)$$

The radius moves the reflection point in the  $x - y$  plane as  $\Delta x$  and  $\Delta y$  from the object's center. The radius changes the reflection  $z$ -location by  $\Delta z$  which affects the amount of layover. The offset values for each radius shape are determined.

The sphere radius moves the reflection point further from the sphere center. The  $x$  offset is  $\Delta x = r \cos \tilde{\theta} \cos \tilde{\phi}$  and the  $y$  offset is  $\Delta y = r \cos \tilde{\theta} \sin \tilde{\phi}$ . The  $z$  offset is  $\Delta z = r \sin \tilde{\theta}$ .

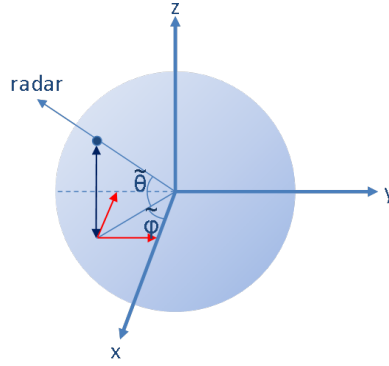


Figure 3.2: Shown with the red arrows, the sphere radius creates translation from the sphere center in the  $x - y$  plane:  $\Delta x = r \cos \tilde{\theta} \cos \tilde{\phi}$  and  $\Delta y = r \cos \tilde{\theta} \sin \tilde{\phi}$ . The vertical black arrow shows the sphere radius increases in the  $z$ -location of  $\Delta z = r \sin \tilde{\theta}$ .

Adding the radius offset terms, the sphere layover equations are

$$x_g = x + z \tan \psi + r \cos \tilde{\theta} \cos \tilde{\phi} + r \sin \tilde{\theta} \tan \psi; \quad (3.5)$$

$$y_g = y + z \tan \eta + r \cos \tilde{\theta} \sin \tilde{\phi} + r \sin \tilde{\theta} \tan \eta. \quad (3.6)$$

The cylinder radius moves the reflection point from the cylinder center. The  $x$  offset is  $\Delta x = r \cos \tilde{\theta}$ . The  $z$  offset is  $\Delta z = r \sin \tilde{\theta}$ . Adding the radius offset terms, the cylinder

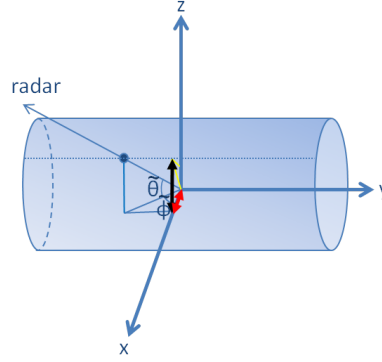


Figure 3.3: Shown in red, the cylinder radius creates translation from the cylinder center in the  $x$  direction by  $\Delta x = r \cos \tilde{\theta}$ . The black arrow shows the cylinder radius increases the  $z$ -location by  $\Delta z = r \sin \tilde{\theta}$ .

layover equations are

$$x_g = x + z \tan \tilde{\theta} + r \cos \tilde{\theta} + r \sin \tilde{\theta} \tan \psi; \quad (3.7)$$

$$y_g = y + z \tan \eta + r \sin \tilde{\theta} \tan \eta. \quad (3.8)$$

The radius of the top-hat creates an offset from the location parameters  $(x, y, z)$  to the incident surface for the radar return. The double bounce puts the reflection range at the corner between the flat and upright position. The  $x$  offset is  $\Delta x = r \cos \tilde{\phi}$  and the  $y$  offset is  $\Delta y = r \sin \tilde{\phi}$ . There is no offset in the  $z$  direction. Adding the radius offset terms, the top-hat layover equations are:

$$x_g = x + z \tan \tilde{\theta} + r \cos \tilde{\phi}; \quad (3.9)$$

$$y_g = y + z \tan \eta + r \sin \tilde{\phi}. \quad (3.10)$$

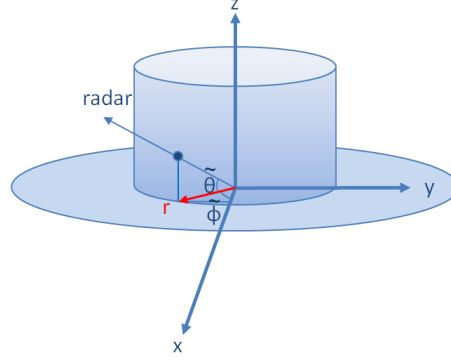


Figure 3.4: The top-hat radius creates translation from the top-hat center in the  $x - y$  plate by  $\Delta x = r \cos \tilde{\phi}$  and  $\Delta y = r \sin \tilde{\phi}$ .

### 3.1.1.2 Mathematic solution.

For each shape, two or more distinct observed ground locations  $(x_g, y_g)$  for an object creates a system of linear equations that may be solved to estimate the object's 3-D location  $(x, y, z)$  and radius, when applicable. The standard form of the equations is  $v = \chi[x \ y \ z]^T$  for the flat shapes or  $v = \chi[x \ y \ z \ r]^T$  for the curved shapes. This section demonstrates the vectors and matrices for two images, but  $v$  and  $\chi$  can be extended if more images are included. The observations,  $v = [x_{g1} \ y_{g1} \ x_{g2} \ y_{g2}]^T$ , are used to determine the unknowns.

The transfer function,  $\chi$ , for each shape is found by combining two sets of the layover equations, one from each of the two images. The combined transfer functions are

$$\chi_{plate,dihedral,trihebral} = \begin{bmatrix} 1 & 0 & \tan \psi_1 \\ 0 & 1 & \tan \eta_1 \\ 1 & 0 & \tan \psi_2 \\ 0 & 1 & \tan \eta_2 \end{bmatrix}; \quad (3.11)$$

$$\chi_{sphere} = \begin{bmatrix} 1 & 0 & \tan \psi_1 & \cos \tilde{\theta}_1 \cos \tilde{\phi}_1 + \sin \tilde{\theta}_1 \tan \psi_1 \\ 0 & 1 & \tan \eta_1 & \cos \tilde{\theta}_1 \sin \tilde{\phi}_1 + \sin \tilde{\theta}_1 \tan \eta_1 \\ 1 & 0 & \tan \psi_2 & \cos \tilde{\theta}_2 \cos \tilde{\phi}_2 + \sin \tilde{\theta}_2 \tan \psi_2 \\ 0 & 1 & \tan \eta_2 & \cos \tilde{\theta}_2 \sin \tilde{\phi}_2 + \sin \tilde{\theta}_2 \tan \eta_2 \end{bmatrix}; \quad (3.12)$$

$$\chi_{cylinder} = \begin{bmatrix} 1 & 0 & \tan \psi_1 & \cos \tilde{\theta}_1 + \sin \tilde{\theta}_1 \tan \psi_1 \\ 0 & 1 & \tan \eta_1 & \sin \tilde{\theta}_1 \tan \eta_1 \\ 1 & 0 & \tan \psi_2 & \cos \tilde{\theta}_2 + \sin \tilde{\theta}_2 \tan \psi_2 \\ 0 & 1 & \tan \eta_2 & \sin \tilde{\theta}_2 \tan \eta_2 \end{bmatrix}; \quad (3.13)$$

$$\chi_{top-hat} = \begin{bmatrix} 1 & 0 & \tan \psi_1 & \cos \tilde{\phi}_1 \\ 0 & 1 & \tan \eta_1 & \sin \tilde{\phi}_1 \\ 1 & 0 & \tan \psi_2 & \cos \tilde{\phi}_2 \\ 0 & 1 & \tan \eta_2 & \sin \tilde{\phi}_2 \end{bmatrix}. \quad (3.14)$$

The least-squares system solution is determined using the pseudoinverse as

$$\begin{aligned} \nu &= \chi[x \ y \ z \vdots r]^T. \\ \chi^H \nu &= \chi^H \chi[x \ y \ z \vdots r]^T. \\ [x \ y \ z \vdots r]^T &= (\chi^H \chi)^{-1} \chi^H \nu. \end{aligned} \quad (3.15)$$

The  $\vdots r$  symbols indicate that the fourth entry is only used the sphere, cylinder, and top-hat. For a square matrix, the pseudoinverse can be replaced by the matrix inverse shown to be

$$\begin{aligned} \nu &= \chi[x \ y \ z \vdots r]^T. \\ \chi^{-1} \nu &= \chi^{-1} \chi[x \ y \ z \vdots r]^T. \\ [x \ y \ z \vdots r]^T &= \chi^{-1} \nu. \end{aligned} \quad (3.16)$$

The LS solutions is not viable if the transfer matrix  $\chi$  or the matrix  $\chi^H \chi$  is singular. In this case the inverse or pseudoinverse is undefined. Singularity is determined by the flight paths for each shape type. Flight path analysis is provided in Section 3.1.1.3. Non-singularity is achieved through diversity in azimuth and elevation which provide unique grazing and tilt angles.

The needed diversity is demonstrated for the top-hat transfer matrix for two images. A matrix is singular if its determinant equals zero. The top-hat transfer matrix determinant is

$$\begin{aligned}
\det(\chi_{top-hat}) &= \begin{vmatrix} 1 & 0 & \tan \psi_1 & \cos \tilde{\phi}_1 \\ 0 & 1 & \tan \eta_1 & \sin \tilde{\phi}_1 \\ 1 & 0 & \tan \psi_2 & \cos \tilde{\phi}_2 \\ 0 & 1 & \tan \eta_2 & \sin \tilde{\phi}_2 \end{vmatrix}. \\
&= 1 \begin{vmatrix} 1 & \tan \eta_1 & \sin \tilde{\phi}_1 \\ 0 & \tan \psi_2 & \cos \tilde{\phi}_2 \\ 1 & \tan \eta_2 & \sin \tilde{\phi}_2 \end{vmatrix} + 1 \begin{vmatrix} 0 & \tan \psi_1 & \cos \tilde{\phi}_1 \\ 1 & \tan \eta_1 & \sin \tilde{\phi}_1 \\ 1 & \tan \eta_2 & \sin \tilde{\phi}_2 \end{vmatrix}. \\
&= (\sin \tilde{\phi}_1 - \sin \tilde{\phi}_2)(\tan \psi_1 - \tan \psi_2) - (\cos \tilde{\phi}_1 - \cos \tilde{\phi}_2)(\tan \eta_1 - \tan \eta_2).
\end{aligned} \tag{3.17}$$

The determinant of  $\chi_{top-hat}$  is zero if the azimuth angles for both flight paths are equal  $\tilde{\phi}_1 = \tilde{\phi}_2$ . This result is understandable geometrically. Diversity in azimuth provides unique look angles in order to estimate the radius of the top-hat.

### 3.1.1.3 *Flight Paths.*

Section 3.1.1.2 provides the mathematic solution for estimating the 3-D location along with the radius parameter. The example of top-hat demonstrates how the geometry of the object requires certain diversity in the flight path. Different attributes of each canonical shapes necessitate specific minimum flight path diversity.

In this thesis, partitions of a flight path for data collection in Step 1C are chosen to achieve sufficient diversity in azimuth and elevation. The partitions are evaluated to ensure they generate non-singular matrices for each shape type. The flight paths are in Table 3.1. The corresponding layover grazing angles,  $\psi$ , and tilt angles,  $\eta$ , are in Table 3.2. The flight paths are shown graphically in Figure 3.5. The shapes in a scene are not known a priori.

Therefore, the combined data from all the flight segments are needed to estimate the scene shapes and parameters.

Table 3.1: Flight path azimuth and elevation ranges. The specific shape reflection geometries need specific flight path diversity for parameter estimation. Table 3.3 matches the flight path to each shape.

Flight Path	Imaging Segment 1	Imaging Segment 2
Up-down	$\tilde{\phi} \in [-10^\circ, 0^\circ], \tilde{\theta} \in [27.5^\circ, 32.5^\circ]$	$\tilde{\phi} \in [0^\circ, 10^\circ], \tilde{\theta} \in [32.5^\circ, 27.5^\circ]$
Disjoint	$\tilde{\phi} \in [-20^\circ, -10^\circ], \tilde{\theta} \in [27.5^\circ, 27.5^\circ]$	$\tilde{\phi} \in [0^\circ, 10^\circ], \tilde{\theta} \in [32.5^\circ, 27.5^\circ]$
Two-pass	$\tilde{\phi} \in [-5^\circ, 5^\circ], \tilde{\theta} \in [27.5^\circ, 32.5^\circ]$	$\tilde{\phi} \in [-5^\circ, 5^\circ], \tilde{\theta} \in [37.5^\circ, 37.5^\circ]$

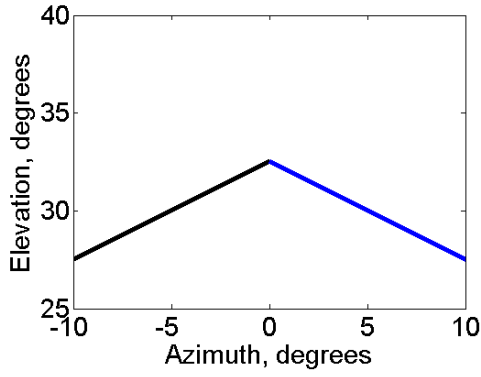
Table 3.2: The grazing angles,  $\psi$ , and tilt angles,  $\eta$ , for each flight partition in the thesis. The angles are those of the slant plane in the range and cross-range, respectively.

Flight Segment	Grazing angle, $\psi$	Tilt angle, $\eta$
Up-down 1	32.5°	31.6°
Up-down 2	32.5°	-31.6°
Disjoint 1	26.8°	-7.7°
Disjoint 2	32.5°	-31.6°
Two-pass 1	30.2°	33.8°
Two-pass 2	37.6°	0.0°

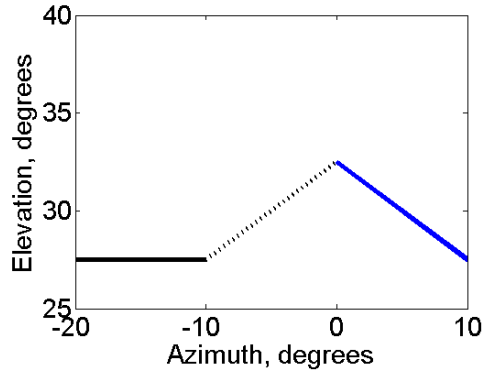
The partitions chosen for each shape type are provided in Table 3.3. The determinant of the transfer matrix for each shape type determines if the flight partitions can be used to solve for the 3-D location.

The amplitude response equations from Table 2.3 correspond to the geometry of each shape and determine why the flight partitions work. The plate, dihedral, and cylinder have a small azimuthal specular response. The sinc function in the equations shows the narrow response mathematically. The small range of specular response necessitates the flight paths for each image be connected or overlap so both images capture specular.

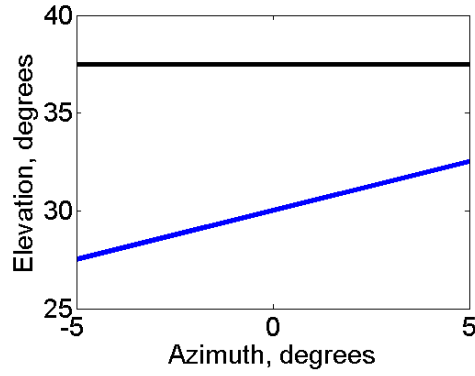




(a) “Up-down” flight path.



(b) “Disjoint” flight path.



(c) “Two-pass” flight path.

Figure 3.5: Flight path partitions shown in azimuth and elevation. Unique tilt angles produce unique layover projection angles in range and cross-range. Imaging segment one is in black. Imaging segment two is in blue. The dotted portion of the Disjoint flight path partitions include segment one from the up-down flight path. It is not used for calculations of the Disjoint partitions.

The sphere, cylinder, and top-hat have a radius parameter. The radius estimate improves for diversity in azimuth and elevation. Just as the top-hat requires azimuth diversity, the cylinder requires elevation diversity. For large rotations, the diversity needs can lie along a different flight path parallel to the shape curvature. The sphere needs diversity in at least one direction for a sufficient radius estimate from the location estimate.

The Up-down flight path provides coverage for limited specular response in azimuth and elevation. The Up-down is the only flight path that sees specular for the plate tested

Table 3.3: The determinant of the flight path partition transfer matrix is shown. A determinant of 0 means the matrix is singular. The chosen flight segments for each shape type are bold and underlined. The disjoint partitions are not applicable for the plate, dihedral, and cylinder due to their limited azimuth response width. There is a gap of 5 degrees in the disjoint flight path, so both formed images would not see the shape.

	<b>Up-down</b>	<b>Disjoint</b>	<b>Two-pass</b>
plate	<b><u>3.0</u></b>	N/A	1.0
dihedral	3.0	N/A	<b><u>1.0</u></b>
trihedral	3.0	0.5	<b><u>1.0</u></b>
sphere	0	<b><u>0.1</u></b>	0
cylinder	0	N/A	<b><u>0.01</u></b>
top hat	0	<b><u>0.1</u></b>	0

in the simulations in Chapters 4 and 5. The Disjoint flight path provides the most diversity for radius estimation. Disjoint is used for the sphere and top-hat to give the best radius estimate. The Two-pass provides coverage for limited specular along the azimuth path and also has diversity in elevation for radius estimate. Two-pass is used for the cylinder to cover its limited specular and give diversity for the radius estimate. Although it has a smaller determinant, the Two-pass is used over the Up-down flight path for the dihedral and trihedral because it has diversity in both the grazing and tilt angles from Table 3.2.

The partitions of the collected PH that correspond these flight partitions are used in Step 1C to form images. From the images, the shapes' 2-D locations are determined for 3-D location estimation in Step 2B.

### ***3.1.2 Collection Radar Parameters.***

Along with the flight path, the radar parameters affect the collection data. The radar parameters determine the range and cross-range resolution and the range and cross-range scene extent. Resolution determines how close two objects can be in a scene and still be

resolved. Scene extent discussed in the technical overview of Section 2.1 determines the 2-D size of the unaliased scene.

The generic equations are provided along with the chosen parameters for this thesis in Equations (3.18) - (3.21). After the resolution and scene extent values are provided, Table 3.4 is provided to summarize the radar collection parameters in this thesis.

The range resolution is

$$\text{resolution}_{\text{range}} = \frac{c}{2B} = \frac{3 \times 10^8 \text{ m/s}}{2(3 \times 10^9 \text{ s}^{-1})} = 0.05 \text{ m}, \quad (3.18)$$

where  $c$  is the speed of light, and  $B$  is the radar total bandwidth. A bandwidth of 3 GHz is beyond the capability of most radars but is used to match the simulated target sizes of the thesis.

The cross-range resolution is

$$\text{resolution}_{\text{cross-range}} = \frac{\lambda_c}{2\Delta\tilde{\phi}} = \frac{0.15 \text{ m}}{2(10^\circ \cdot \frac{\pi}{180^\circ})} = 0.43 \text{ m}, \quad (3.19)$$

where  $\lambda_c$  is the center wavelength, and  $\Delta\tilde{\phi}$  is the azimuth collection extent. The center wavelength is the wavelength corresponding to the center frequency  $\lambda_c = \frac{c}{f}$ . The azimuth scene extent of  $10^\circ$  is near that used by [2] so final estimation results can be compared.

The sample size in azimuth and bandwidth set the scene extent for 2-D SAR images.

The range scene extent is

$$E_{\text{range}} = \frac{c}{2\delta f} = \frac{3 \times 10^8 \text{ m/s}}{2 \cdot (3 \times 10^9 \text{ s}^{-1}/128)} = 6.4 \text{ m}, \quad (3.20)$$

where  $\delta f$  is the frequency sample size. The frequency sample size is determined by dividing the bandwidth by the number of samples. The number of frequency samples is chosen to produce a scene extent without aliasing. The objects simulated and estimated are within the range and cross-range scene extent.

The cross-range scene extent is

$$E_{\text{cross-range}} = \frac{\lambda_{\min}}{2\delta\phi} = \frac{0.0857 \text{ m}}{2 \cdot (2^\circ \cdot \frac{\pi}{180^\circ})} = 12.3 \text{ m}, \quad (3.21)$$

where  $\lambda_{min}$  is the minimum wavelength, and  $\delta\phi$  is the sample size in azimuth. The azimuth sampling is chosen to prevent aliasing like the frequency sampling choice.

Table 3.4: The simulated radar parameters are provided. The parameters are the radar total bandwidth, the number of frequency samples, center frequency, the azimuth extent per flight partition, and the azimuth sample step size. Each parameter affects the 2-D imaging performance and are tied to specific equations with references provided. The center frequency is used to determine the center wavelength and minimum wavelength for the cross-range equations using  $\lambda = \frac{c}{f}$ .

<b>Radar Parameter</b>	<b>Parameter Value</b>	<b>Parameter Determines ...</b>	<b>Determining Equation</b>
Bandwidth, $B$	3 GHz	range resolution	Equation (3.18)
Frequency Samples	128	range scene extent	Equation (3.20)
Center frequency, $f_c$	2.5 GHz	cross-range resolution	Equation (3.19)
		cross-range scene extent	Equation (3.21)
Azimuth Extent	10°	cross-range resolution	Equation (3.19)
Azimuth Sample Size	0.2°	cross-range scene extent	Equation (3.21)

### 3.2 Step 1B: Error Analysis Pre-Processing

For radar data collection, the flight and radar parameters are known. These collection parameters determine the ability to estimate parameters in a surveyed scene. A theoretical flight path that collects over infinite bandwidth at all azimuth and elevation locations would provide perfect information about a scene.

In reality, the collection flight path and radar collection parameters are limited. The limited collection parameters determine the minimum and maximum errors in the parameter estimates. In Step 1B, the collection parameters are tested over all shape types and shape parameters to produce error bounds. With limited resources, testing over “all” parameters is limited to a representative set. This pre-processing step finds the possible range of errors for any estimate. The error ranges can be applied to initial estimates in Step 2 with no prior information of the objects in a scene.

Using a representative set of parameters for each shape type, the range of possible errors are determined for each parameter of location, size, and orientation. The representative set of parameters is determined for the flight path in this thesis in Section 3.2.1. The same set is used for the location and size error analysis. For the orientation parameters, the combinations of orientation are coupled, so a Monte Carlo simulation is used to find error ranges.

### ***3.2.1 Representative Parameter Set.***

In order to calculate the range errors possible, the estimation steps of the algorithm are tested over “all” possible parameter combinations. Testing all combinations is computationally impossible, so a representative set of parameters is tested. The representative set includes the range of parameters that are detectable.

Step 1C detects scatterers in a scene from PH data. Detection is based on the amplitude of the peaks detected in a 2-D SAR image. If the amplitude meets a certain threshold, it is detected and its parameters are estimated. The user defined threshold chosen for this thesis is 15 dB. The amplitude is measured relative to the peak response of each shape, which occurs when the specular response occurs within the flight path.

For each shape type, the representative set includes the extrema of parameters that the radar will detect. The location and size parameters are all on the order of 1 m, so the representative set uses parameters near  $x = 1$  m,  $y = 1$  m,  $z = 1$  m,  $L = 1$  m  $H = 1$  m, and  $r = 1$  m. The orientation angles are adjusted until the shape is not detected. The orientation limits for each shape type in the representative set are in Table 3.5.

Table 3.5: The representative parameter set orientation angles for each shape. The limits are chosen for when the each shape type is still detected in a 2-D SAR image for the flight parameters of this thesis. The detection limit is set to 15 dB from the peak specular response.

Shape	Size	Orientation Bounds	Result Figure
plate	L = 1 m; H = 1 m	$[\gamma \in (-2^\circ, 2^\circ), \theta \in (-30^\circ, -35^\circ), \phi \in (-2^\circ, 2^\circ)]$	Figure 3.6
	L = 2 m; H = 2 m	$[\gamma \in (-1^\circ, 1^\circ), \theta \in (-30^\circ, -33^\circ), \phi \in (-1^\circ, 1^\circ)]$	Figure 3.7
dihedral	L = 1 m; H = 1 m	$[\gamma \in (-15^\circ, 17^\circ), \theta = 0^\circ, \phi \in (-8^\circ, 8^\circ)]$	Figure 3.8
trihedral	H = 1 m	$[\gamma \in (-90^\circ, 90^\circ), \theta \in (0^\circ, 90^\circ), \phi \in (-45^\circ, 45^\circ)]$	Figure 3.9
sphere	$r \in [0.5, 3.0]$	N/A	Figure 3.10
cylinder	L = 1 m; r = 1 m	$[\gamma \in (-13^\circ, 13^\circ), \theta = 0^\circ, \phi \in (-5^\circ, 5^\circ)]$	Figure 3.11
top-hat	H = 1 m; r = 1	$[\gamma \in (-10^\circ, 10^\circ), \theta \in (0^\circ, 60^\circ), \phi = 0^\circ]$	Figure 3.12

Similar analysis may be performed for any flight path and object sizes. Thus, this pre-processing step applies to general cases and can be tuned to expected targets in a scene.

### 3.2.2 Location Error Analysis.

Three-dimensional location error analysis is completed prior to data collection to find the range of possible errors. The range of possible location errors is determined from the errors of a representative set of shapes. The minimum and maximum errors measured from the set are taken. The errors bounds are used in Step 2C to limit the location parameters once an initial location estimate is made for an unknown scatterer.

The 3-D location  $(x, y, z)$  is estimated using 2-D SAR images. Section 2.1 and Figure 2.2 detail how the flight path affects the imaging ground plane due to layover. The mathematic solution for the 3-D location estimate is in Section 3.1.1.2.

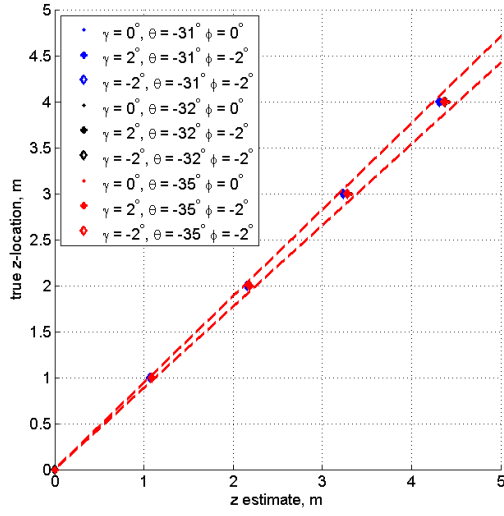
The values for the parameters of the representative set for location error analysis are in Table 3.7. The  $x$  and  $y$  location only translate an object in the 2-D image plane and do not add error, so the representative location parameters are all for  $x = 0$  and  $y = 0$ . The error

Table 3.6: The representative parameter set for location error analysis is provided. The limits are chosen for when the each shape type is still detected in a 2-D SAR image for the flight parameters of this thesis. The detection limit is set to 15 dB from the peak specular response.

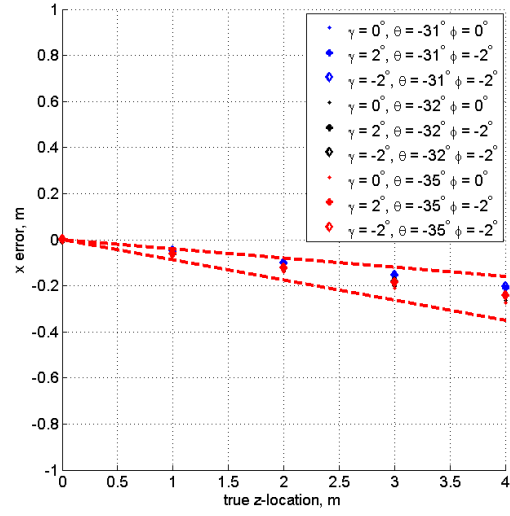
Parameter	Values	Reasoning
x	0	No change in error for x location
y	0	No change in error for y location
z	[1,4]	Error increases with z location due to layover
L,H,r	1	Representative size for the simulations of this thesis
$\gamma, \theta, \phi$	Table 3.5	Representative angles per shape type are used

occurs when the shape is projected into the ground plane, so the  $z$  parameter can effect the error. Therefore, the  $z$  location parameter changes in the representative set.

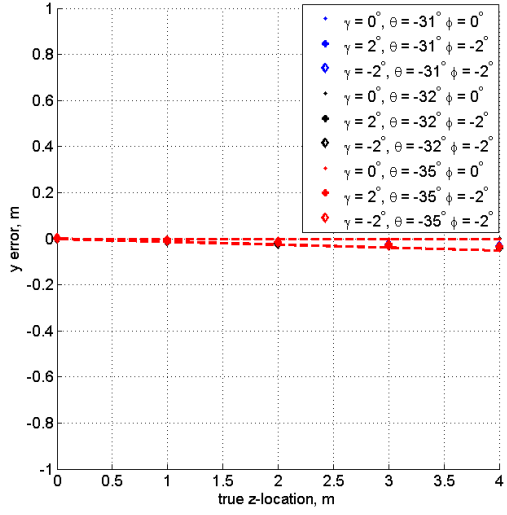
The size parameters of the representative set use  $L = 1$ ,  $H = 1$ , and  $r = 1$  to coincide with the order of magnitude of the targets in this thesis. One exception is that the plate was also tested with  $L = 2$  and  $H = 2$ . The orientation angles from the detection ranges in Table 3.5. The orientation angle combinations tested for each shape type are provided on each error plot legend in Figure 3.6-Figure 3.12. The errors are plotted as a function of the  $z$  parameter because the error increases as  $z$  increases. The figures plot the measurement errors, and the worst case of the possible errors are bounded using red dotted lines.



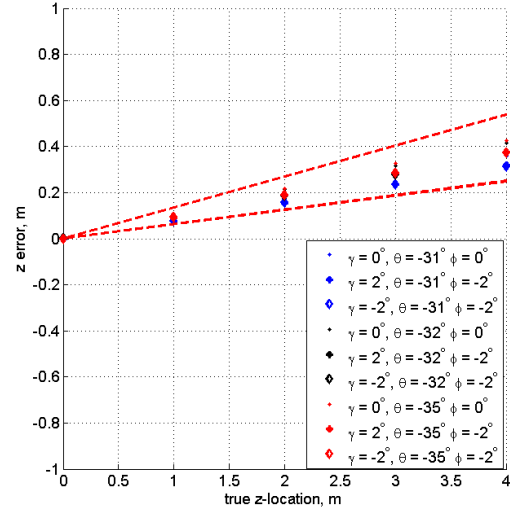
(a) Z location for z estimate



(b) Plate x error



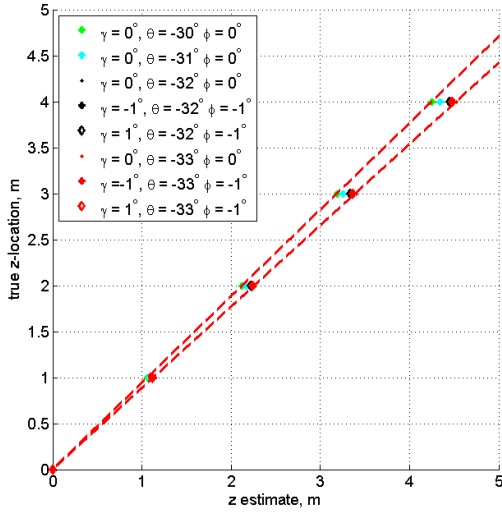
(c) Plate y error



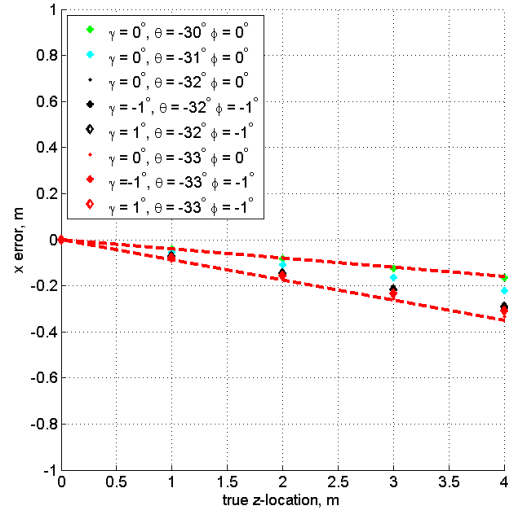
(d) Plate z error

Figure 3.6: Location estimation errors for a plate of  $L = 1$  m,  $H = 1$  m at varying z-locations. The points are the calculated errors at the sample points for the corresponding shape orientations. The red lines are the bounds on the error.

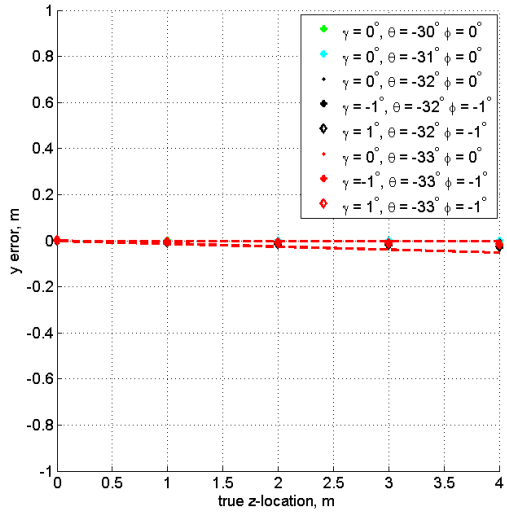




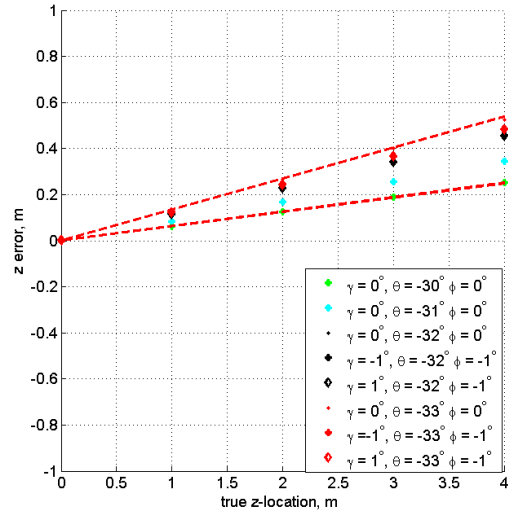
(a) Z location for z estimate



(b) Plate x error

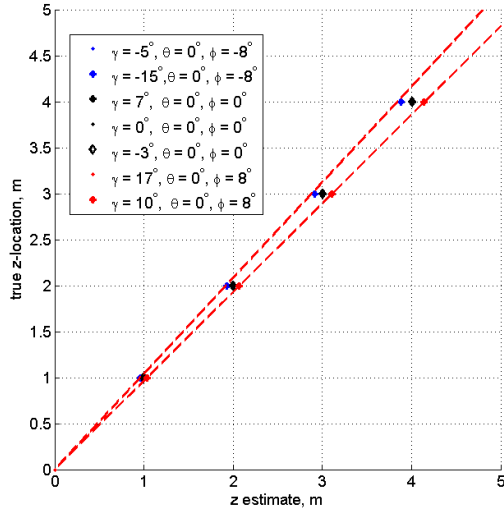


(c) Plate y error

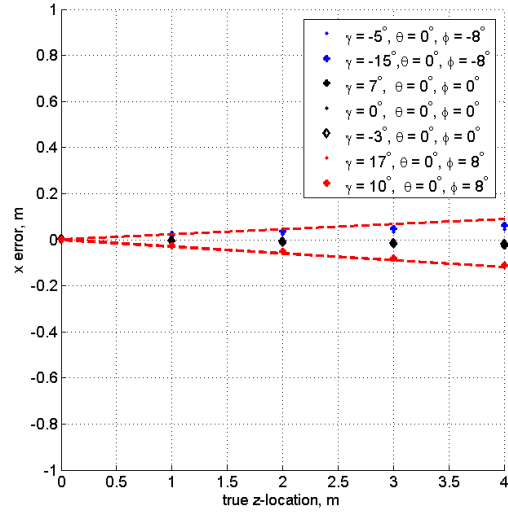


(d) Plate z error

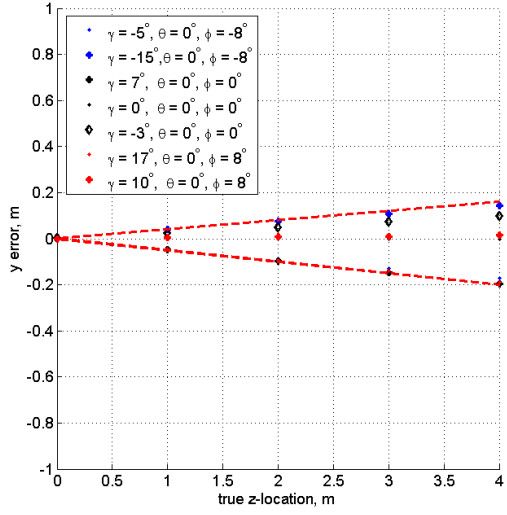
Figure 3.7: Location estimation errors for a plate of  $L = 2$  m,  $H = 2$  m at varying z-locations. The points are the calculated errors at the sample points for the corresponding shape orientations. The red lines are the bounds on the error.



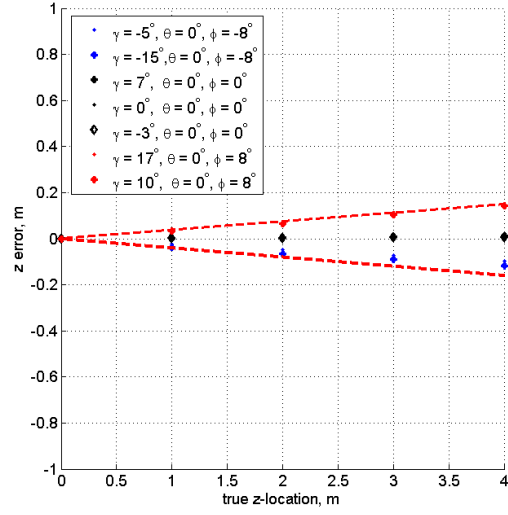
(a) Z location for z estimate



(b) Dihedral x error

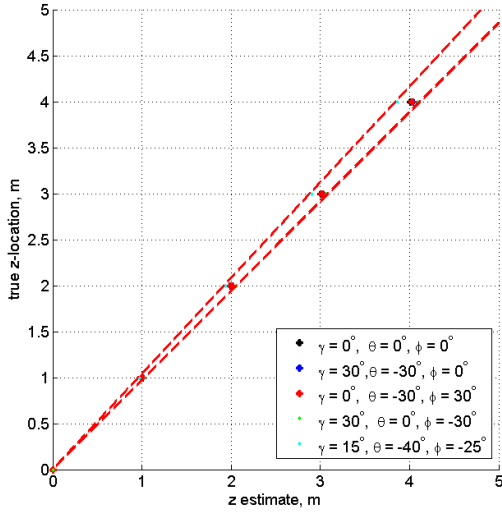


(c) Dihedral y error

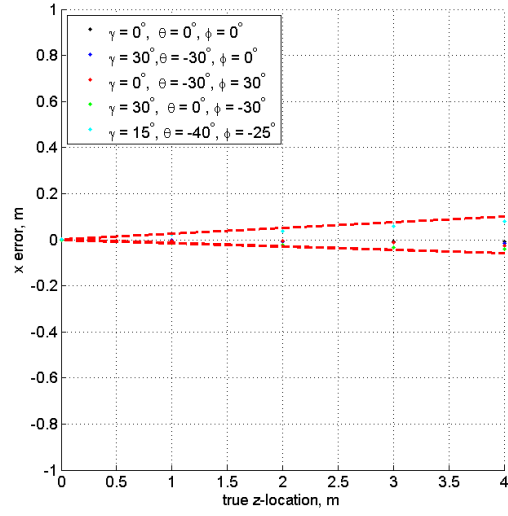


(d) Dihedral z error

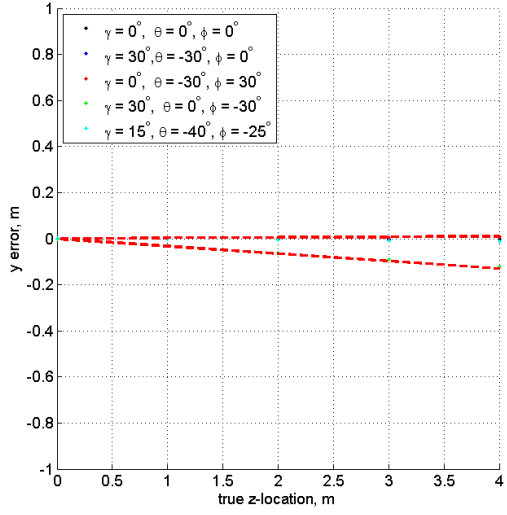
Figure 3.8: Location estimation errors for a dihedral of  $L = 1$  m,  $H = 1$  m at varying z-locations. The points are the calculated errors at the sample points for the corresponding shape orientations. The red lines are the bounds on the error.



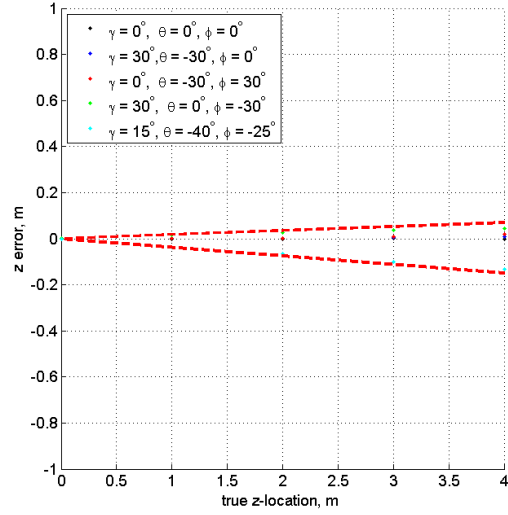
(a) Z location for z estimate



(b) Trihedral x error

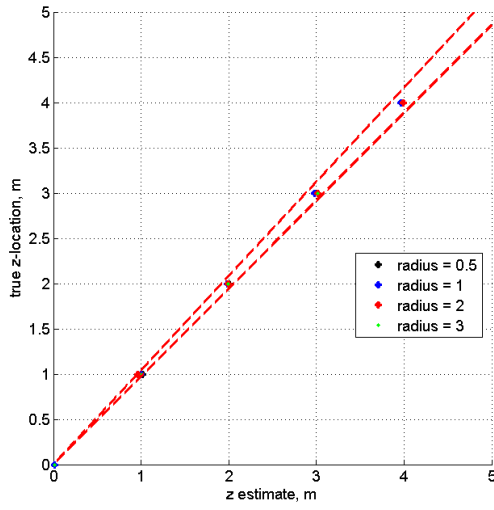


(c) Trihedral y error

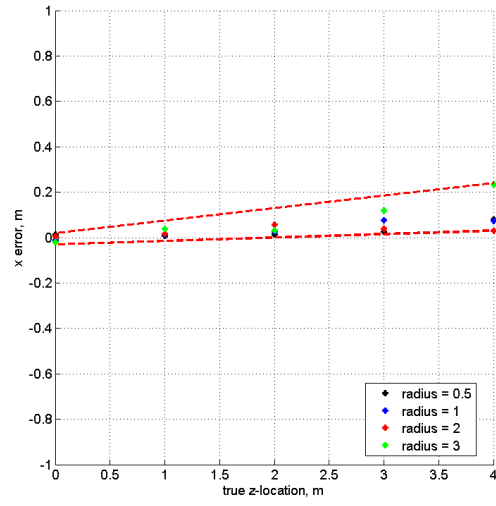


(d) Trihedral z error

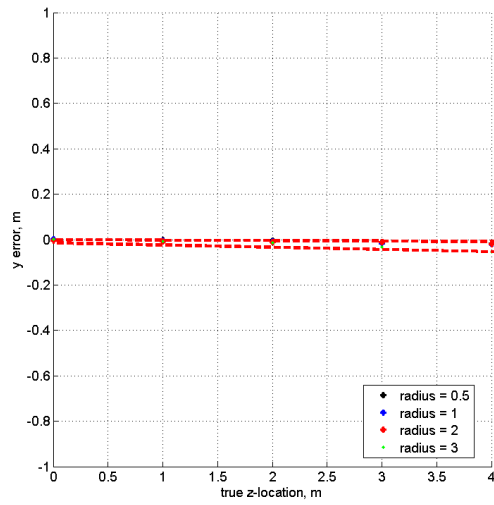
Figure 3.9: Location estimation errors for a trihedral of  $H = 1$  m at varying  $z$ -locations. The points are the calculated errors at the sample points for the corresponding shape orientations. The red lines are the bounds on the error.



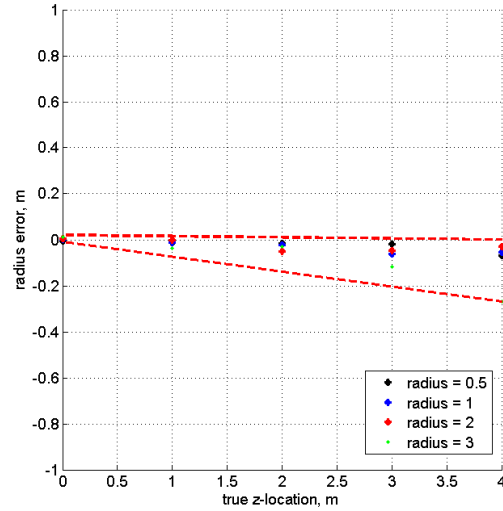
(a) Z location for z estimate



(b) Sphere x error

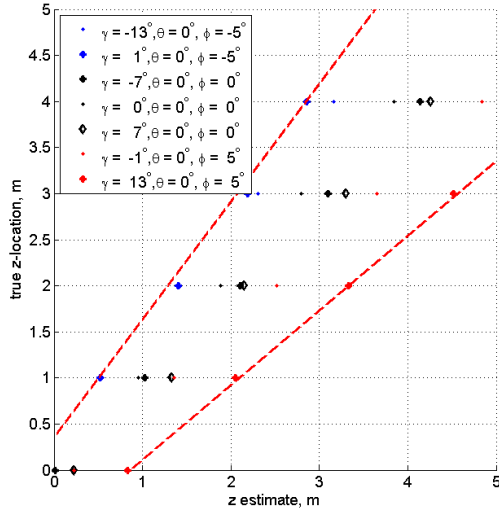


(c) Sphere y error

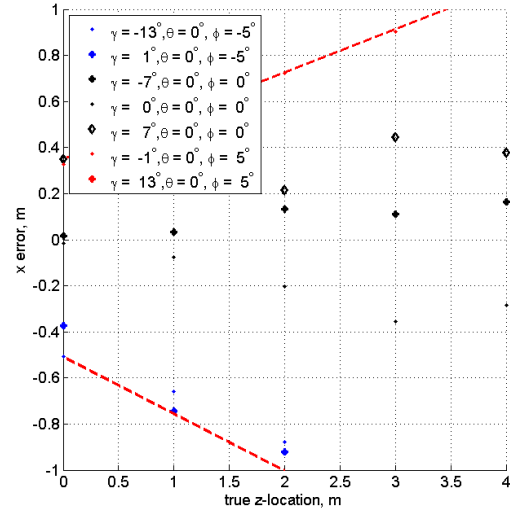


(d) Sphere radius error

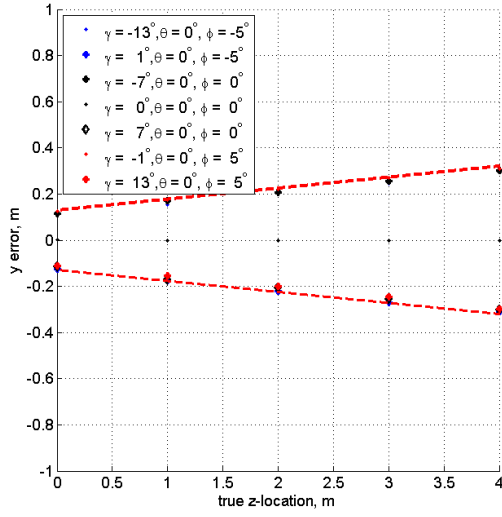
Figure 3.10: Location and radius estimation errors for a sphere of  $r = (0.5, 1, 2, 3)$  m at varying z-locations. The points are the calculated errors at the sample points. The red lines are the bounds on the error.



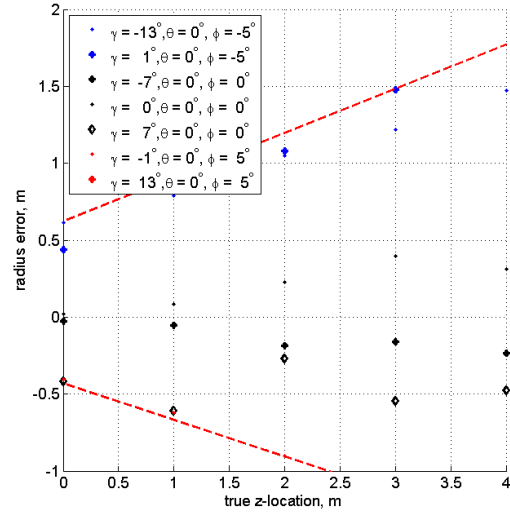
(a) Z location for z estimate



(b) Cylinder x error

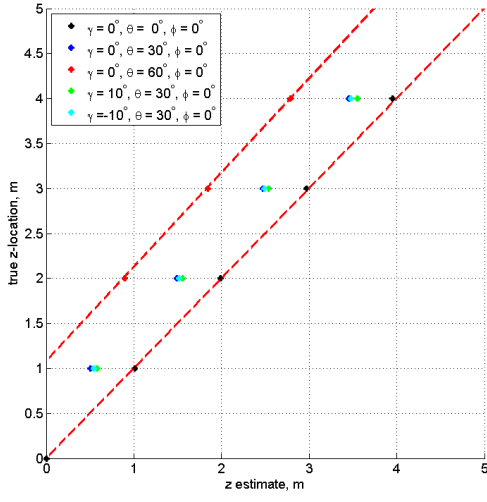


(c) Cylinder y error

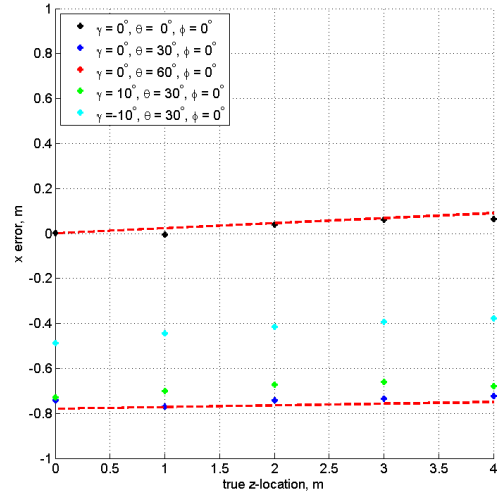


(d) Cylinder radius error

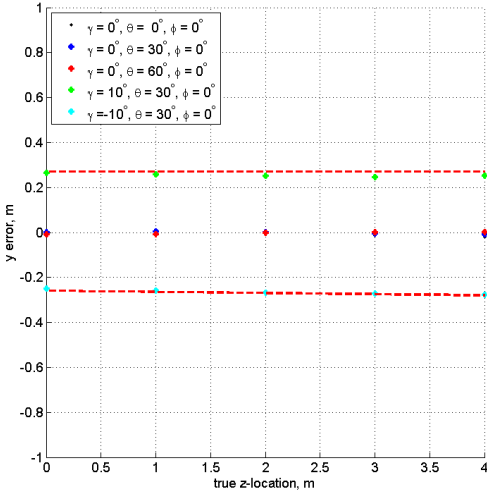
Figure 3.11: Location and radius estimation errors for a cylinder of  $L = 1$  m,  $r = 1$  m at varying z-locations. The points are the calculated errors at the sample points for the corresponding shape orientations. The red lines are the bounds on the error.



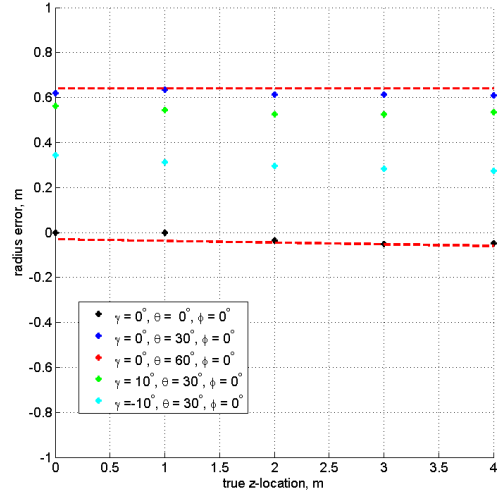
(a) Z location for z estimate



(b) Top-hat x error



(c) Top-hat y error



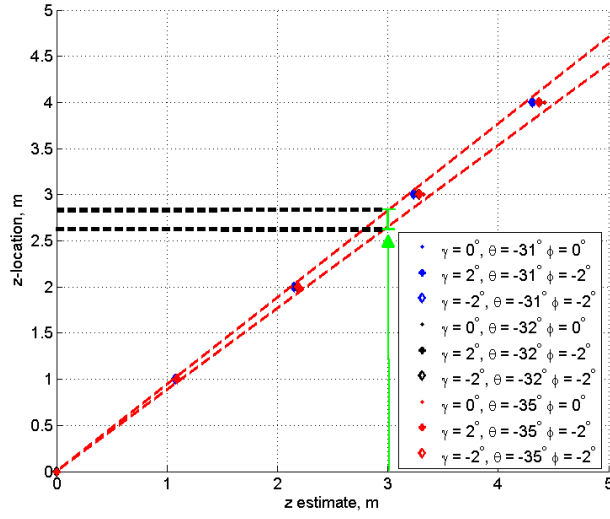
(d) Top-hat radius error

Figure 3.12: Location and radius estimation errors for a top-hat of  $H = 1$  m,  $r = 1$  m at varying z-locations. The points are the calculated errors at the sample points for the corresponding shape orientations. The red lines are the bounds on the error.

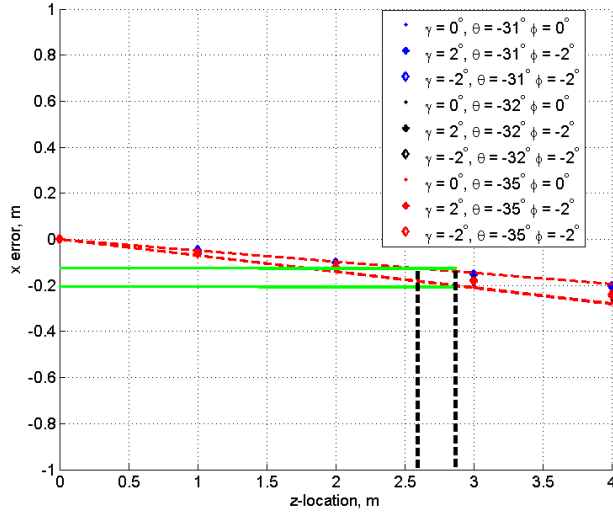
Once an initial estimate is made in Step 2C, the pre-processed errors bounds from this section are used to bound the possible range for each location parameter. The method of applying the bounds is shown graphically in Figure 3.13 as an example. The figures for the example are from the plate in Figures 3.6(a) and 3.6(b). The example is for an initial estimate of  $z = 3$  m; the true value is unknown. Figure 3.13(a) shows the possible range of  $z$  locations for an estimate of  $z = 3$  m. The error bounds relate an estimate of  $z = 3$  m to a possible true  $z$  value within  $z \in [2.6 \text{ m}, 2.8 \text{ m}]$ .

The range of possible  $z$  values determine the error range to apply to the other location parameters. This is demonstrated for the  $x$  parameter in Figure 3.13(b). The range of  $z$  values denoted by the black dotted lines intersect the  $x$  error bars. The minimum and maximum  $x$  errors on the graph are applied to the  $x$  estimate as  $x_{true} \in [x_{est} - x_{max \text{ error}}, x_{est} - x_{min \text{ error}}]$ . The parallel computation is done to find the range of the true  $y$  parameter and the true  $r$  parameter, if applicable.

In the example in Figure 3.13(b),  $x_{error} \in [-0.2 \text{ m}, -0.1 \text{ m}]$ . The range of true  $x$  values are  $x_{true} = [x_{est} - (-0.1 \text{ m}), x_{est} - (-0.2 \text{ m})]$ , or  $x_{true} = [x_{est} + 0.1 \text{ m}, x_{est} + 0.2 \text{ m}]$ .



(a) Plate z location estimate



(b) Plate x error

Figure 3.13: Graphical depiction of the 3-D location error bound calculations using the error data. The 3-D location estimates are a function of the z location. The first step to determining the range for the location and radius parameters is determining the z range. Figure 3.13(a) takes the z estimate and finds the z range. Figure 3.13(b) shows how the z range is used to find the x errors. The errors are applied to the initial x estimate to get the x range. The z range is similarly used to find the y and radius ranges.



### 3.2.3 Size Error Analysis.

The size parameters are length, height, and radius. Like the 3-D location error bounding, the size parameter errors are pre-processed using a representative set of parameter combinations. The radius parameter is coupled with the location so its error bounds are already calculated with the location errors in Section 3.2.2.

The length parameter is estimated using the 2-D segment length in the 2-D image from Step 1C. The details of the the estimation are in Section 4.4. The height parameter estimate is calculated using the RCS estimates and other size parameters and is also detailed in Section 4.4. For each representative shape tested, the size estimates and errors are determined.

Table 3.7: The representative parameter set for size error analysis is provided. The limits are chosen for when the each shape type is still detected in a 2-D SAR image for the flight parameters of this thesis. The detection limit is set to 15 dB from the peak specular response.

Parameter	Values	Reasoning
$x$	0	No change in error for x location
$y$	0	No change in error for y location
$z$	0	Minor changes in error for changes in the z location
$L$	[0.2, 3.0]	Full range of parameter used in this thesis
$H$	[0.5, 3.0]	Full range of parameter used in this thesis
$r$	0.5	Minor changes in error for changes in the radius
$\gamma, \theta, \phi$	Table 3.5	Representative angles per shape type are used

The location has little effect on the size estimation error so the parameters are set for the size error pre-processing. The length and height parameters are estimated using the same detectable orientation angles from Section 3.2.2. The orientation combinations are tested for lengths and heights in the range of [0.2 m, 3.0 m].

The length parameter estimate for the plate, dihedral, and cylinder is the measured length of radar image segment. Segmentation is discussed in Step 1C in Section 3.3.

A scatterer's length causes the segment peak to spread in the 2-D image. The length is measured using a threshold roll-off from the scatterer peak amplitude. The thresholds discussed previously are provided in Table 3.8. The thresholds are chosen to achieve minimum error for the standard orientation.

Table 3.8: Length estimate segment thresholds and standard orientations.

<b>Shape</b>	plate	dihedral	cylinder
<b>Threshold</b>	1.2 dB	6.5 dB	6.5 dB
<b>Standard Orientation</b>	$(0^\circ, -32^\circ, 0^\circ)$	$(0^\circ, 0^\circ, 0^\circ)$	$(0^\circ, 0^\circ, 0^\circ)$
<b>Results Figure</b>	Figure 3.14	Figure 3.15	Figure 3.16

Each shape length is estimated for  $L \in [0.2 \text{ m}, 3.0 \text{ m}]$ . The other size parameters are held constant at  $H = 1 \text{ m}$  or  $r = 0.5 \text{ m}$ .

The length error results and bounds are provided in Figures 3.14 - 3.16. The length estimates in each figure show that the estimates do not go below 0.4 m for any shape. The estimate minimum coincides with cross-range resolution of 0.43 m.

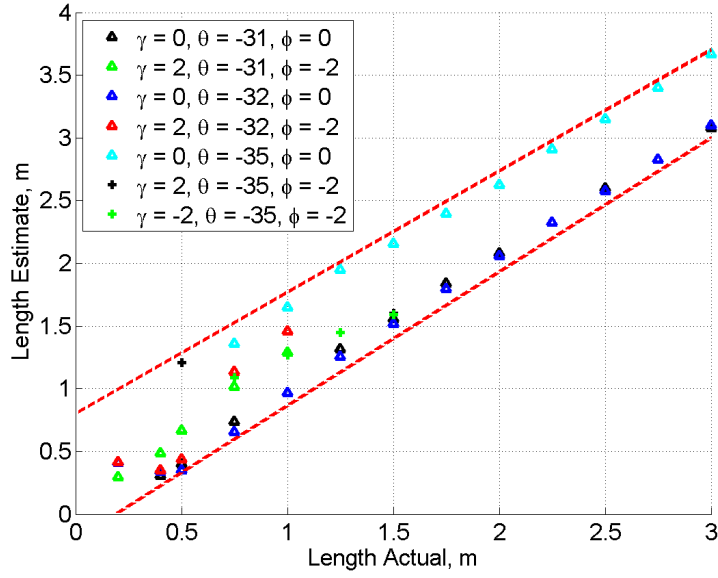


Figure 3.14: Length estimation errors for a plate of  $L \in [0.2 \text{ m}, 3.0 \text{ m}]$ . The height is set to  $H = 1 \text{ m}$ . The points are the calculated errors at the sample points for the corresponding shape orientations. The red lines are the bounds on the error.

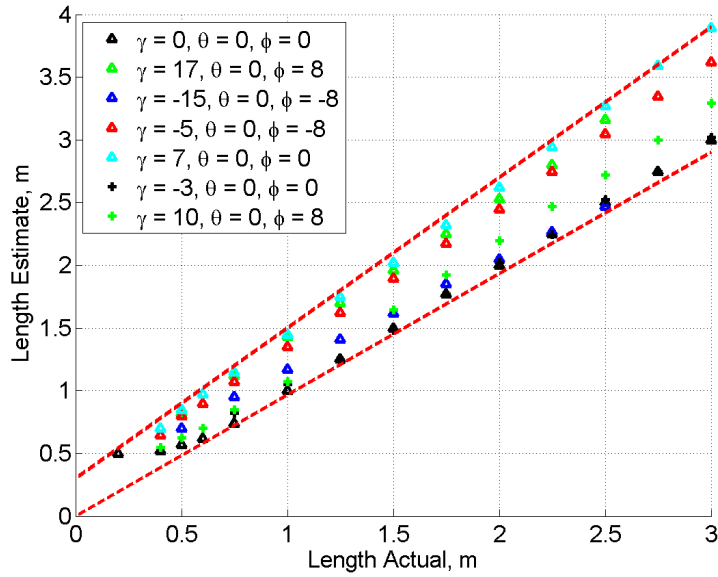


Figure 3.15: Length estimation errors for a dihedral of  $L \in [0.2 \text{ m}, 3.0 \text{ m}]$ . The height is set to  $H = 1 \text{ m}$ . The points are the calculated errors at the sample points for the corresponding shape orientations. The red lines are the bounds on the error.

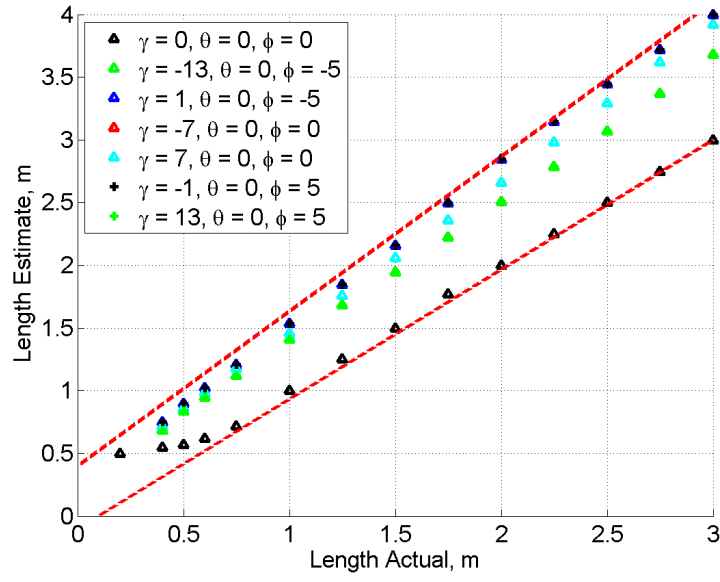


Figure 3.16: Length estimation errors for a cylinder of  $L \in [0.2 \text{ m}, 3.0 \text{ m}]$ . The radius is set to  $r = 0.5 \text{ m}$ . The points are the calculated errors at the sample points for the corresponding shape orientations. The red lines are the bounds on the error.

The length estimate figures also demonstrate that the length estimate can increase as the shape is skewed from the baseline orientation. As the orientation skews, the apparent length increases along the flight path. This skew is demonstrated in Figure 3.17.

The orientation angle of a shape relative to the flight path can also decrease the length estimate. The shape of the PH can widen if the flight path does not hit the peak. The Fourier relation of widening in the PH domain transforms to narrowing in the spatial domain.

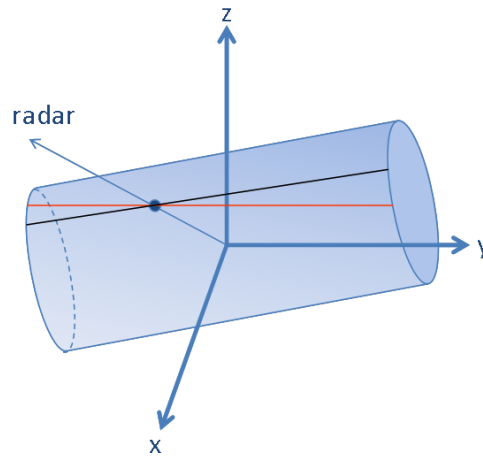


Figure 3.17: The actual length (black line) is shorter than the apparent length (red line) when captured by the radar and projected into a 2-D SAR image.

The length parameter is bound using the maximum and minimum error bounds. Calculating the length error is shown in Figure 3.18. The height parameter estimates and errors found next are recorded the same way as the length estimates and errors; therefore, the height error bounds for dictionary formation are done the same way as the length.

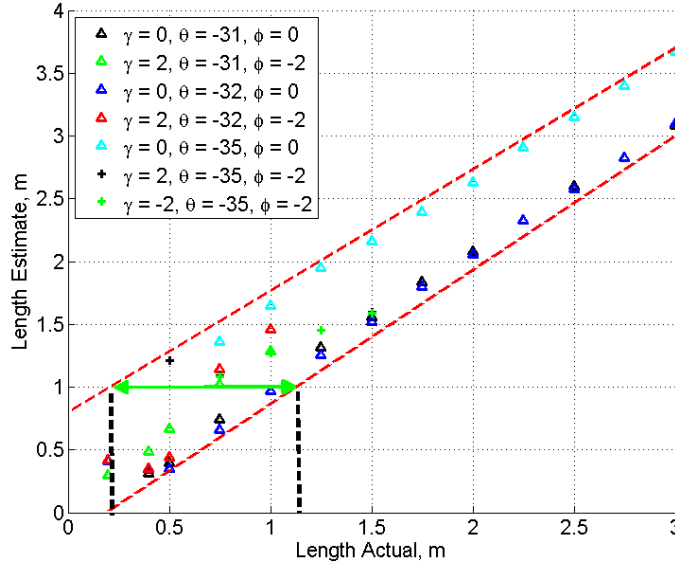


Figure 3.18: The length error minima and maxima are used to bound the length parameter from the initial length estimate. The plate example show that for an initial estimate of  $L = 1$  m, the length parameter is bound by  $L \in [0.2 \text{ m}, 1.2 \text{ m}]$ . The same procedure is used for bounding the height parameter.

The height estimates for the plate, dihedral, trihedral, and top-hat are calculated using the prior estimates of the other size parameters (length and radius) and the RCS estimate and is discussed in Section 4.4. If the shape specular direction, or direction of maximum reflectivity, and the flight path do not intersect, the peak RCS estimate is less than the true peak RCS of the scatterer. Since the height estimation equations derived in Table 3.9 come from the peak RCS equations in Table 4.6, a reduced RCS estimate results in a lower height estimate.

Each shape height is estimated for  $H \in [0.5 \text{ m}, 2.0 \text{ m}]$  with the other size parameters constant at  $L = 1 \text{ m}$  or  $r = 0.5 \text{ m}$ . The actual versus estimated height values are in Figures 3.19 - 3.22. From an initial estimate, the height bounds are taken as the minimum and maximum corresponding error. In this thesis, the height size is bound on the high

Table 3.9: Height equations from the peak RCS, L, and r estimates. The height estimates for each shape are provided in the results figures listed.

Shape	Height equation	Results Figure
plate	$\sqrt{\frac{RCS \cdot \lambda^2}{4\pi L^2}}$	Figure 3.19
dihedral	$\sqrt{\frac{RCS \cdot \lambda^2}{8\pi L^2}}$	Figure 3.20
trihedral	$\left(\frac{RCS \cdot \lambda^2}{12\pi}\right)^{1/4}$	Figure 3.21
sphere	N/A	–
cylinder	N/A	–
top-hat	$\sqrt{\frac{RCS \cdot \lambda \sqrt{2}}{8\pi r}}$	Figure 3.22

side by  $H = 2$  m. This helps reduce the dictionary size to a reasonable size. The height parameter, as with the others, can be tailored for a specific application.

As expected, as the shape is oriented further from specular, the height estimate decreases. The farther the flight path is from specular, the smaller the RCS estimate due to roll off of the return amplitude envelope.

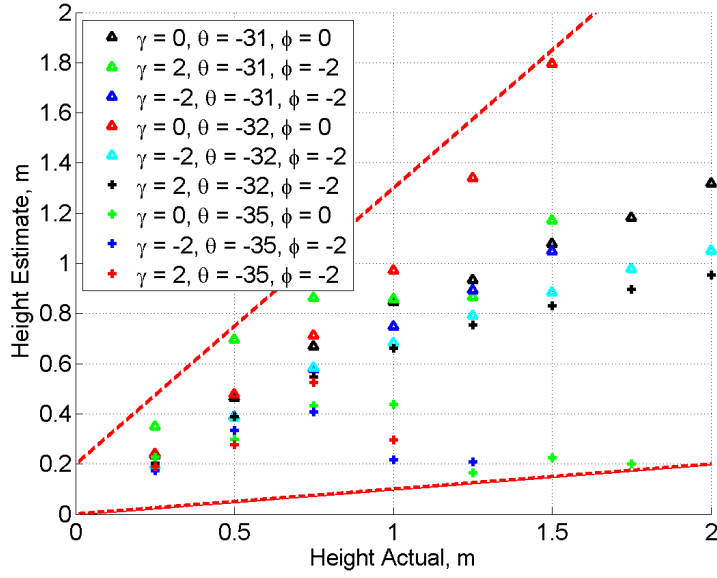


Figure 3.19: Height estimation errors for a plate of  $H \in [0.5 \text{ m}, 2.0 \text{ m}]$ . The length is set to  $L = 2 \text{ m}$ . The points are the calculated errors at the sample points for the corresponding shape orientations. The red lines are the bounds on the error.

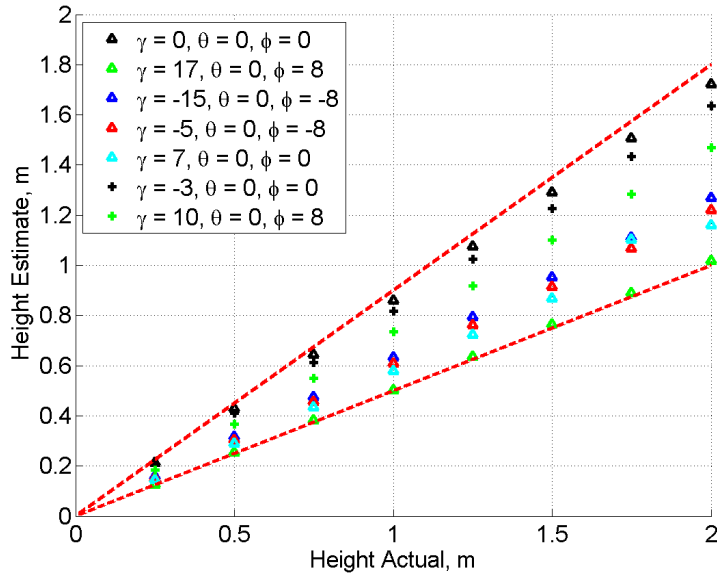


Figure 3.20: Height estimation errors for a dihedral of  $H \in [0.5 \text{ m}, 2.0 \text{ m}]$ . The length is set to  $L = 2 \text{ m}$ . The points are the calculated errors at the sample points for the corresponding shape orientations. The red lines are the bounds on the error.



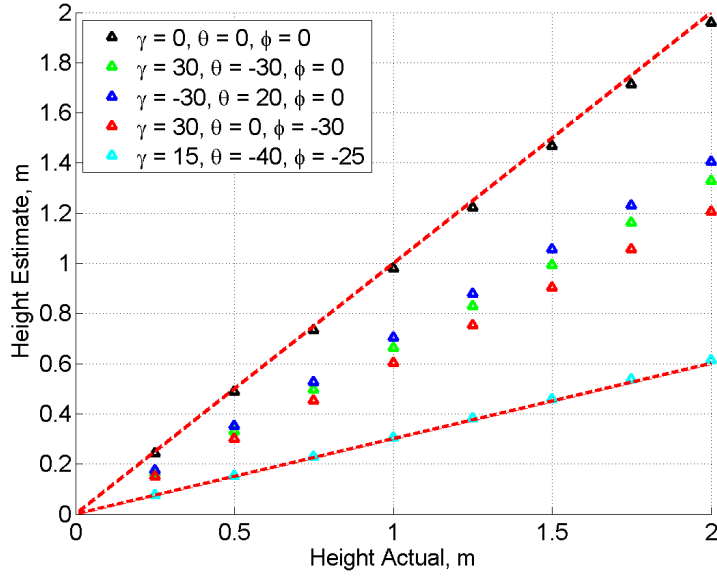


Figure 3.21: Height estimation errors for a trihedral of  $H \in [0.5 \text{ m}, 2.0 \text{ m}]$ . The points are the calculated errors at the sample points for the corresponding shape orientations. The red lines are the bounds on the error.

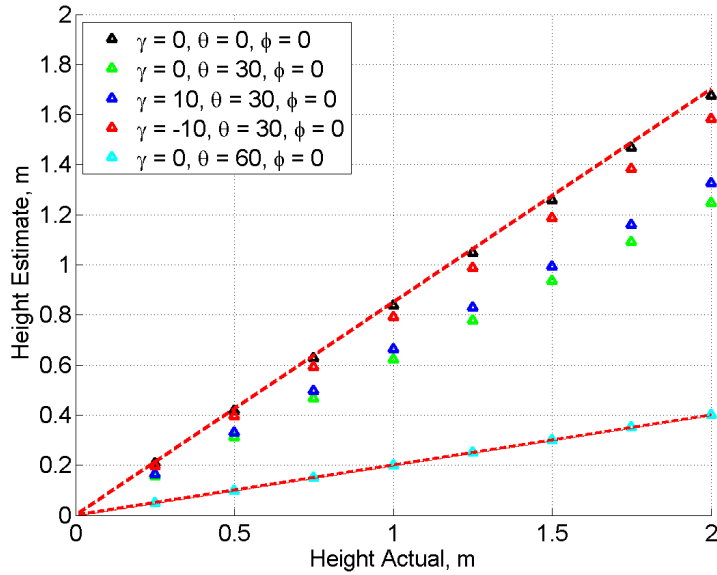


Figure 3.22: Height estimation errors for a top-hat of  $H \in [0.5 \text{ m}, 2.0 \text{ m}]$ . The radius is set to  $r = 0.5 \text{ m}$ . The points are the calculated errors at the sample points for the corresponding shape orientations. The red lines are the bounds on the error.

The radius estimates for the cylinder and top-hat come with the 3-D location estimates and are provided in Figures 3.11(d) and 3.12(d). The radius error figures show that there is large error in the radius estimate from the orientations skew from the standard orientation of  $(\gamma, \theta, \phi) = (0^\circ, 0^\circ, 0^\circ)$ . The error occurs because of the apparent radius changes. Apparent radius is demonstrated with profile view of the top-hat. Figure 3.23(a) shows that the blue top-hat at standard orientation has the correct radius, shown in red. Figure 3.23(b) shows that as the top-hat is pitched (in black), the apparent radius (in red) is shorter than the true radius (in black). The apparent 3-D location is moved as well.

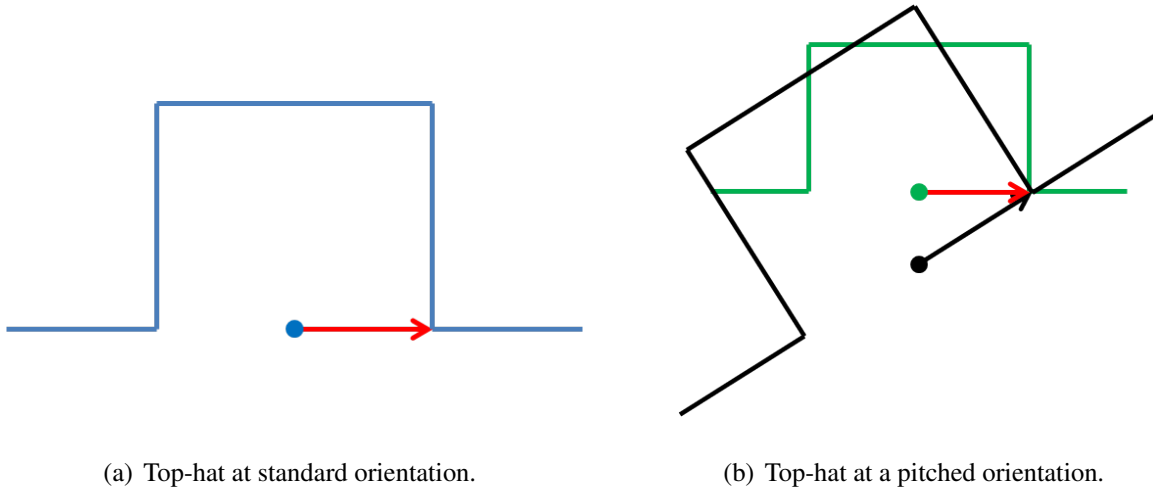


Figure 3.23: The top-hat true radius and apparent radius depends on the orientation. The top-hat profile is shown. In (a) the blue top-hat is at standard orientation so the true radius and apparent radius are the same (red). (b) shows the top-hat is pitched (black). The true top-hat (black) is estimated at the standard orientation (green). The apparent parameters are that of the green top-hat. The 3-D location changes and the radius decreases.

The sphere radius parameter could be bound with the 3-D location estimate; however, the radius estimate can also be calculated using the peak RCS estimate and peak RCS equation,  $RCS_{peak} = \pi r^2$ , from Table 4.6 in Section 4.4. The geometry of the sphere provides peak RCS from any collection angle. In this thesis, the PH data is generated from the scatterer model equations without error, so there is no error in the sphere radius

estimate. If noise or other interference is added to the signal, error analysis can be done on the RCS determined radius estimate and the location coupled radius estimate to determine which method gives less error.

### 3.2.4 Orientation Error Analysis.

The orientation parameter possible error ranges are left to be determined. Unlike the previous parameter error pre-processing, the orientation errors are more difficult to determine in a linear fashion because they are coupled. Therefore the possible errors are determined using a Monte Carlo simulation. The number of Monte Carlo trials per shape type is 200.

For each trial, the orientation parameters are estimated and the errors are recorded. The details of how the parameters are estimated is detailed in Chapter 4 in Section 4.5. The location and size parameters used for the trials are provided in Table 3.10.

Table 3.10: The Monte Carlo random variable distributions for each parameter. The location and orientation random variables are normally distributed to get estimates over the range of the scene. The absolute value of the  $z$  parameter is taken to keep the shape above the ground plane. The true size parameters are not random.

Shape	Parameter	Distribution
All	x and y 3-D location	$\mathcal{N} \sim (\mu = 0 \text{ m}, \sigma = 1 \text{ m})$
All	z 3-D location	$ \mathcal{N} \sim (\mu = 0 \text{ m}, \sigma = 1 \text{ m}) $
All	Size	$L = 1 \text{ m}, H = 1 \text{ m}, r = 0.5 \text{ m}$
All except the plate	Orientation	$\mathcal{N} \sim (\mu = 0^\circ, \sigma = 10^\circ)$
Plate	Orientation	$\mathcal{N} \sim (\mu = -32^\circ, \sigma = 1^\circ)$

For each Monte Carlo trial the true orientation and 3-D location parameters are drawn from a Gaussian random distribution, with the  $z$  value only chosen to be positive. The size parameters are fixed. The orientation of the plate is limited relative to the other shapes because its detection orientation is limited as shown in Table 3.5.

For each Monte Carlo trial, the location and size parameters are estimated according to the estimation methods in Chapter 4, Sections 4.3 and 4.4. The orientation angles are estimated according the method detailed in Section 4.5. For each orientation estimate, the errors are calculated relative to the true values. A summary of the errors are provided in Table 3.11. The minimum error, maximum error, and standard deviation of the 200 trials is recorded.

Table 3.11: The minimum error, maximum error, and standard deviation,  $\sigma$ , for all three orientation parameters: roll ( $\gamma$ ), pitch, ( $\theta$ ), and yaw ( $\phi$ ). Values are from 200 Monte Carlo trials.

Shape	roll min error	roll max error	roll $1\sigma$	pitch min error	pitch max error	pitch $1\sigma$	yaw min error	yaw max error	yaw $1\sigma$
plate	$-0.1^\circ$	$0.2^\circ$	$0.06^\circ$	$-0.01^\circ$	$0.02^\circ$	$0.003^\circ$	$-0.01^\circ$	$0.01^\circ$	$0.005^\circ$
dihedral	$-2.0^\circ$	$7.5^\circ$	$1.0^\circ$	$-9.2^\circ$	$15.0^\circ$	$4.7^\circ$	$-3.4^\circ$	$7.5^\circ$	$1.3^\circ$
trihedral	$-63.2^\circ$	$47.9^\circ$	$10.4^\circ$	$-17.9^\circ$	$3.3^\circ$	$2.7^\circ$	$-35.4^\circ$	$31.5^\circ$	$6.3^\circ$
sphere	N/A	N/A	N/A	N/A	N/A	N/A	N/A	N/A	N/A
cylinder	$-2.7^\circ$	$1.8^\circ$	$0.4^\circ$	$-39.4^\circ$	$32.5^\circ$	$13.5^\circ$	$-10.5^\circ$	$5.5^\circ$	$2.6^\circ$
top-hat	$-15.2^\circ$	$11.7^\circ$	$2.5^\circ$	$-8.8^\circ$	$17.3^\circ$	$2.7^\circ$	$-35.8^\circ$	$66.1^\circ$	$13.1^\circ$

The errors and standard deviation for the plate are less than  $1^\circ$ . The small errors result from the small range of orientations from which the plate can be detected. Thus the allowable orientation parameters are limited.

Table 3.11 demonstrates that shapes with symmetry about a given axis produce the largest error for the orientation parameter coinciding with that axis. The dihedral and cylinder have the largest error in pitch angle. For  $0^\circ$  roll angle, the dihedral has similar shaped PH for any pitch angle and the cylinder PH is identical for any pitch angle. The top-hat has the largest error in yaw angle. For  $0^\circ$  roll angle and pitch angles, the top-hat PH is identical for any yaw angle.

The orientation bounds for dictionary formation are chosen to be three standard deviations from each parameter's initial estimate. The  $3\sigma$  values are in Table 3.12. An example of how the orientation parameters are bound is shown in Equation (3.22) for a dihedral with initial estimates of  $[\gamma_{est}, \theta_{est}, \phi_{est}] = [10^\circ, 10^\circ, 10^\circ]$ .

$$\begin{aligned}
[\gamma_{bound}, \theta_{bound}, \phi_{bound}] &= [(\gamma_{est}, \theta_{est}, \phi_{est}) + (\gamma_{3\sigma}, \theta_{3\sigma}, \phi_{3\sigma})]. \\
&= [(10^\circ, 10^\circ, 10^\circ) + (\pm 5.4^\circ, \pm 12.9^\circ, \pm 3.9^\circ)]. \\
&= [(4.6^\circ, 15.4^\circ), (-2.9^\circ, 22.9^\circ), (6.1^\circ, 13.9^\circ)].
\end{aligned} \tag{3.22}$$

Table 3.12: The  $3\sigma$  error values of the orientation estimates are provided. The given values bound the orientation parameters for dictionary formation.

Shape	roll ( $\gamma$ ) $3\sigma$	pitch ( $\theta$ ) $3\sigma$	yaw ( $\phi$ ) $3\sigma$
plate	$\pm 0.18^\circ$	$\pm 0.01^\circ$	$\pm 0.02^\circ$
dihedral	$\pm 3.1^\circ$	$\pm 14.0^\circ$	$\pm 3.9^\circ$
trihedral	$\pm 31.3^\circ$	$\pm 8.2^\circ$	$\pm 18.9^\circ$
sphere	—	—	—
cylinder	$\pm 1.1^\circ$	$\pm 40.4^\circ$	$\pm 7.7^\circ$
top-hat	$\pm 7.4^\circ$	$\pm 8.2^\circ$	$\pm 39.2^\circ$

With the errors determined for each parameter, the pre-processing for parameter bounding is complete. All of the error bounds are input into Step 2. Once parameter estimates of a detected scatterers are made in Step 2, the error bounds are applied giving the ranges of possible parameter values. The bound parameter are then used in Step 3 in Chapter 5 for dictionary formation.

### 3.3 Step 1C: Data Collection, SAR Image Formation, and Pre-Processing

In Step 1A the collection parameters are chosen and analyzed. In Step 1B, the flight path and radar parameters from Step 1A are tested for each shape type over “all” possible

parameter combinations to determine the minimum and maximum error for any initial estimate. The pre-collection processing is complete, and in Step 1C actual scene data collection commences.

In general, radar returns are transformed into PH as discussed in Section 2.1. This thesis generates simulated PH directly from the 3-D models in [1] according to Equation (2.8). The data used for the entire thesis is generated directly from the scatterer models; no noise, path attenuation, or clutter are added to the observed signals. Each addition would introduce signal error that could affect the results as the signal-to-noise-plus-interference ratio (SINR) degrades.

The complex returns are output as a vector of complex numbers. The complex data PH is used directly for 2-D image formation. For coherency and LS calculations, the data is stored in an atom as a vector of the real and imaginary parts to preserve the amplitude and phase information shown as

$$a(k, \Lambda; \Theta) = \begin{bmatrix} \text{real}(s(\Theta)) \\ \text{imag}(s(\Theta)) \end{bmatrix}. \quad (3.23)$$

After the PH data is generated, 2-D SAR images are formed using the backprojection algorithm according to Equation (2.1) from the technical overview of Chapter 2. Once the images are formed, the image peaks are segmented. The segments are detected and grouped using the watershed algorithm discussed in Section 3.3.1 from [24]. The 2-D SAR images and segments in the image plane are provided in Figures 3.24 - 3.35. The images and segments are used for model order estimation, 2-D location estimation, and peak association.

### ***3.3.1 2-D SAR Image Formation and Segmentation.***

The full flight path is partitioned in order to form multiple 2-D images, one image for the PH of each partition. Flight path partition diversity discussed in Step 1A is required to produce unique scatterer 2-D locations in the images. The diversity creates unique slant

planes for each partition so the projection to the 2-D image ground plane are unique. The mathematical solutions for sufficient flight path diversity is provided in Section 3.1.1.2.

Objects in a scene appear as peaks in the 2-D images. Each peak in an image must be detected and segmented for parameter estimation. Peak detection is necessary to determine the model order, or number of objects in the scene. The location estimation in Section 4.3 uses the segment 2-D locations to triangulate the 3-D location. The 2-D location is calculated using the center of mass of the segment in Section 3.3.3. The size estimation in Section 4.4 uses the length of the segment in the image to estimate length.

The peaks are detected and segmented using a watershed algorithm from [25]. The implementation of the watershed algorithm is taken from [24]. Three user defined thresholds are used to accept or reject pixels, create initial segments, and combine segments. This thesis keeps pixels that are within 20 dB of the peak pixel in the image for segmentation. Initial segmentation starts from pixels that are a local maxima and includes adjacent pixels that have an amplitude within 12 dB of the peak. Initial segments are combined if the lowest pixel amplitude between the segments is within a threshold 12 dB from the peak.

In this thesis, the flight partitions are established in Step 1A in Section 3.1.1.3. For the PH to be generated and processed, truth scenarios are created. The algorithm performance is evaluated using three scenarios. The scenarios range from a single shape to seven shapes. The estimated parameters are compared to the true parameter values.

Scenario 1 parallels Hammond's [2] scenario 1 where a single shape is in the scene whose parameters correspond to one of the dictionary atoms. Scenario 2 likewise parallels Hammond's [2] scenario 2 with a single shape whose parameters are between two dictionary atoms. Scenario 3 with seven shapes replicates the evaluated scenario in [1]. The results of the scenarios are compared directly to the result from [2] and [1].

After the Scenario parameters are presented, the 2-D SAR images and segmented peaks for those images are displayed in Figures 3.24 - 3.35.

Table 3.13: Scenario 1 plate parameters. The parameters are chosen to parallel Scenario 1 from [2]. All the parameters are chosen to be samples of the formed dictionary. The  $x$ ,  $y$ ,  $z$ ,  $L$ ,  $H$ ,  $r$  parameters are in meters, and  $\gamma$ ,  $\theta$ ,  $\phi$  are in degrees.

Shape	x	y	z	L	H	r	$\gamma$	$\theta$	$\phi$
plate	0	0	0	1.0	1.0	–	0	-32	0

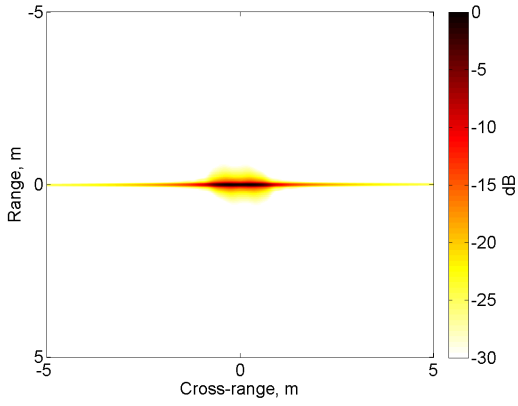
Table 3.14: Scenario 2 plate parameters. The parameters are chosen to parallel Scenario 2 from [2] where not all parameters are in the dictionary parameter samples. Each case includes a different parameter off the dictionary sampling with Case 4 including a parameter off dictionary for each parameter group: location, size, and orientation. The  $x$ ,  $y$ ,  $z$ ,  $L$ ,  $H$ ,  $r$  parameters are in meters, and  $\gamma$ ,  $\theta$ ,  $\phi$  are in degrees.

Case	Shape	x	y	z	L	H	r	$\gamma$	$\theta$	$\phi$
1	plate	0	0	1.05	1.0	1.0	–	0	-32	0
2	plate	0	0	0	1.05	1.0	–	0	-32	0
3	plate	0	0	0	1.0	1.0	–	0	-33.5	0
4	plate	0	0	1.05	1.05	1.0	–	0	-33.5	0

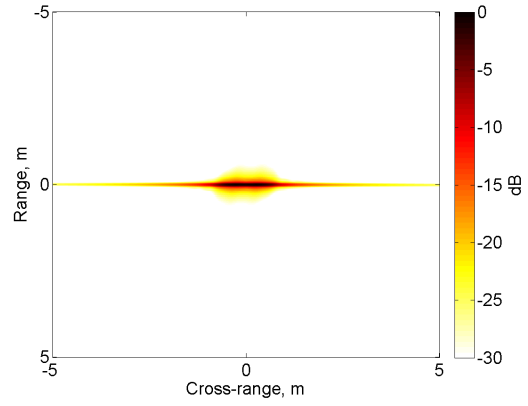
Table 3.15: Scenario 3 scatterer parameters. The parameters are from the evaluated scene in [1]. The set of scatterers include shapes with parameters all in the dictionary and others off dictionary. The  $x$ ,  $y$ ,  $z$ ,  $L$ ,  $H$ ,  $r$  parameters are in meters, and  $\gamma$ ,  $\theta$ ,  $\phi$  are in degrees.

Shape	x	y	z	L	H	r	$\gamma$	$\theta$	$\phi$
plate	-0.3	0	0.3	0.6	0.3	–	0	-30	0
dihedral <sub>1</sub>	0.25	0.5	0	0.6	0.2	–	0	0	0
dihedral <sub>2</sub>	0	1.1	2.5	0.6	0.30	–	-10	0	0
trihedral	0.75	0	0.5	–	0.18	–	0	0	0
sphere	-1.5	-1.0	0	–	–	0.75	–	–	–
cylinder	0.5	2.0	0	.5	–	1.5	0	0	-5
top-hat	0.25	-1.5	0	–	0.4	0.6	0	0	0

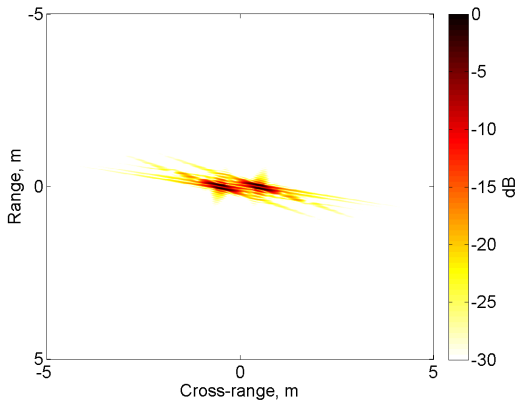




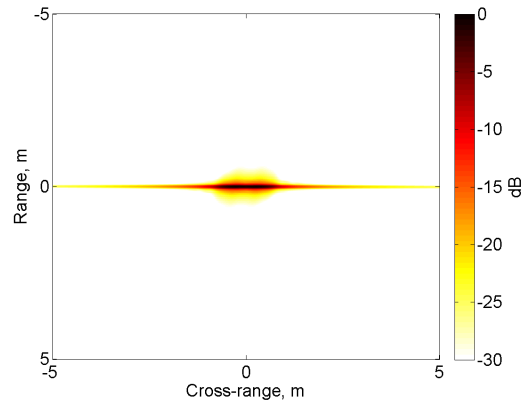
(a) Up-down flight path segment 1 image.



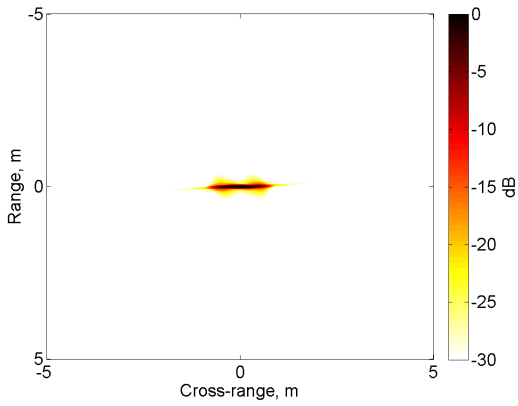
(b) Up-down flight path segment 2 image.



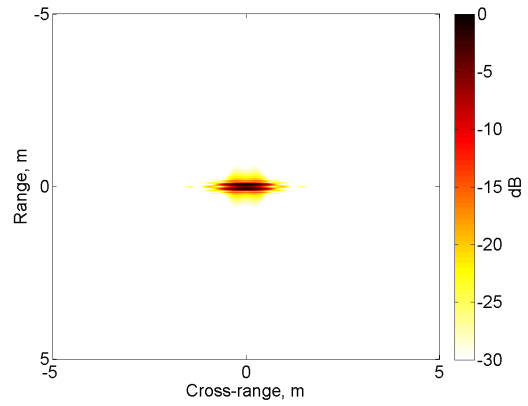
(c) Disjoint flight path segment 1 image.



(d) Disjoint flight path segment 2 image.

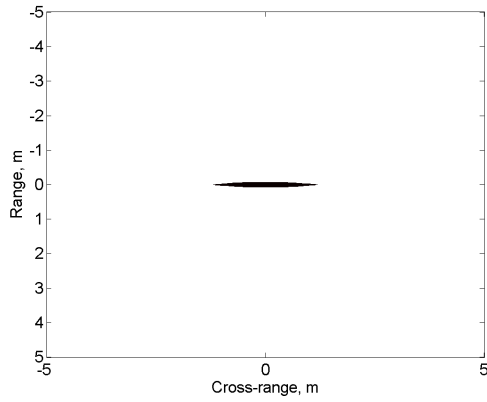


(e) Two-pass flight path segment 1 image.

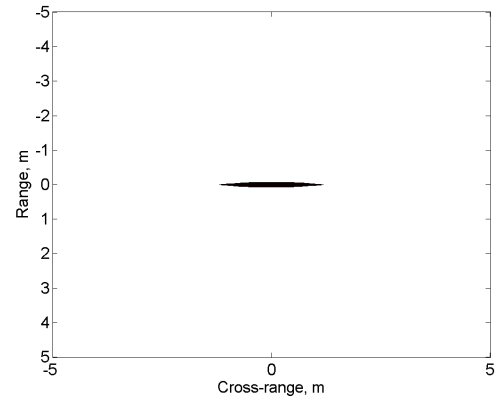


(f) Two-pass flight path segment 2 image.

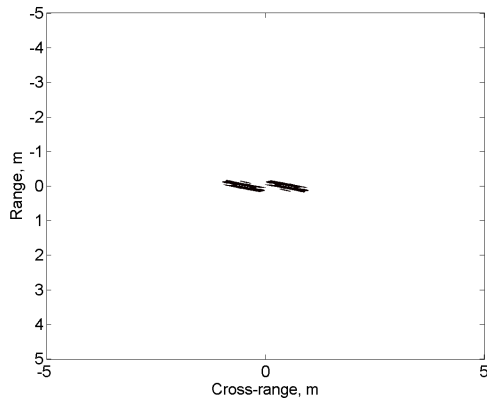
Figure 3.24: Scenario 1 2-D SAR images for each flight path segment.



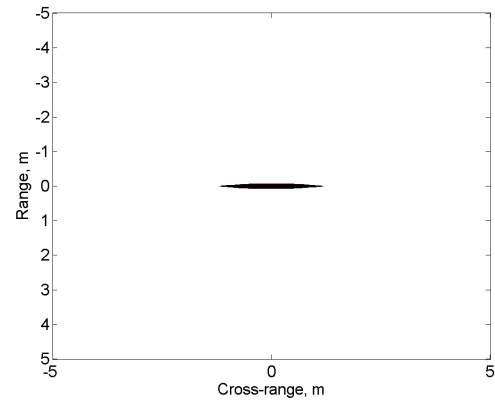
(a) Up-down flight path segment 1 image segment mask.



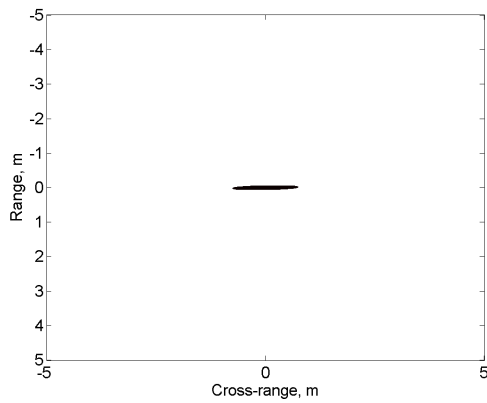
(b) Up-down flight path segment 2 image segment mask.



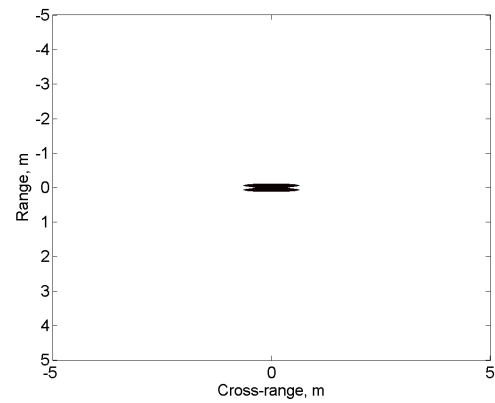
(c) Disjoint flight path segment 1 image segment mask.



(d) Disjoint flight path segment 2 image segment mask.

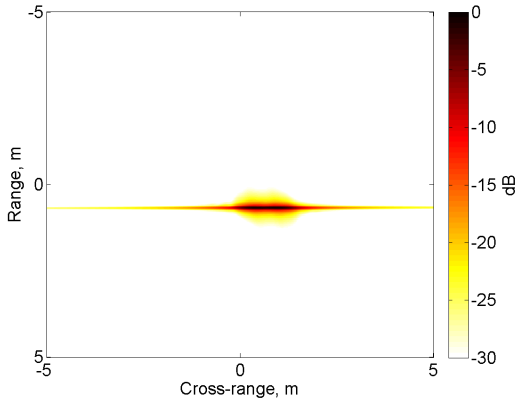


(e) Two-pass flight path segment 1 image segment mask.

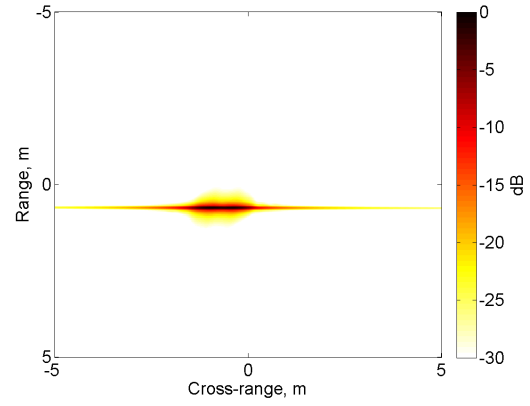


(f) Two-pass flight path segment 2 image segment mask.

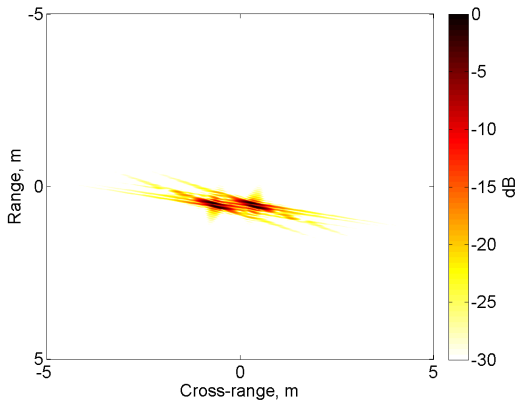
Figure 3.25: Scenario 1 segment masks for the 2-D SAR images for each flight path segment.



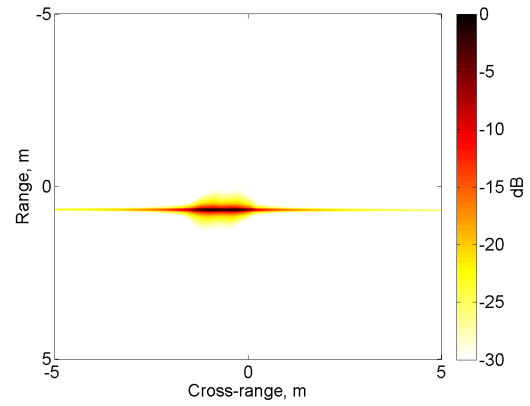
(a) Up-down flight path segment 1 image.



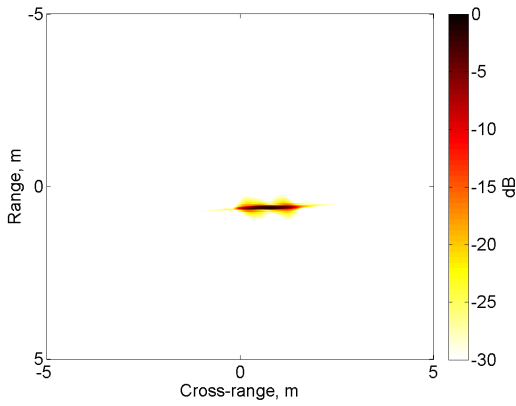
(b) Up-down flight path segment 2 image.



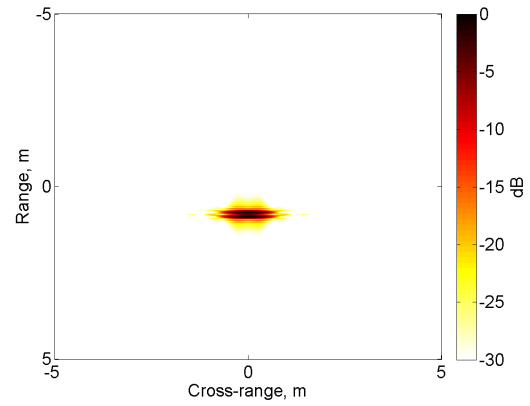
(c) Disjoint flight path segment 1 image.



(d) Disjoint flight path segment 1 image.

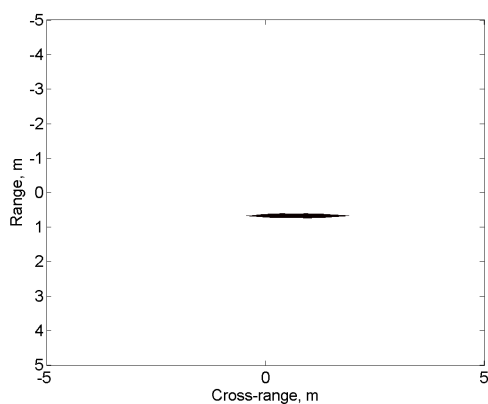


(e) Two-pass flight path segment 1 image.

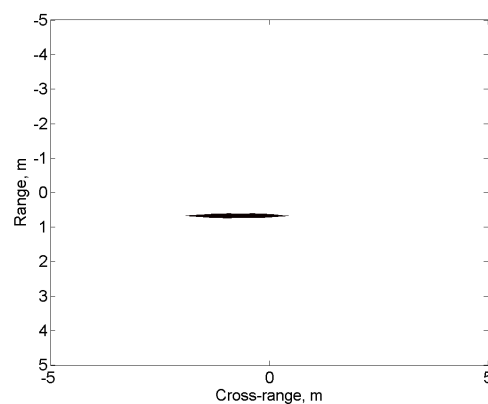


(f) Two-pass flight path segment 1 image.

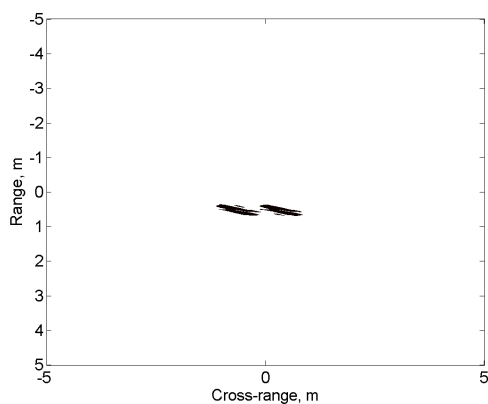
Figure 3.26: Scenario 2 Case 1 2-D SAR images for each flight path segment.



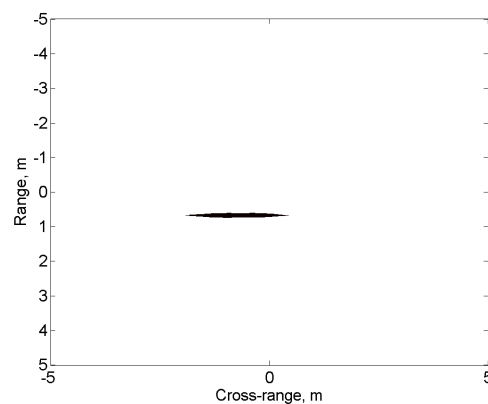
(a) Up-down flight path segment 1 image segment mask.



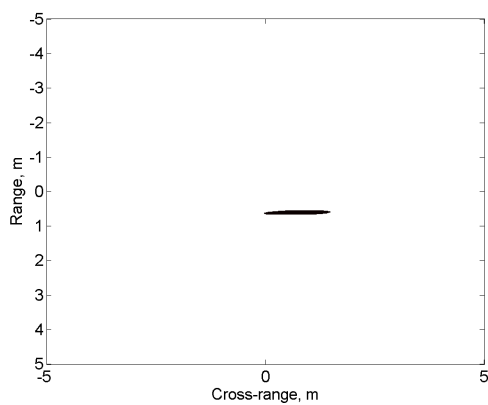
(b) Up-down flight path segment 2 image segment mask.



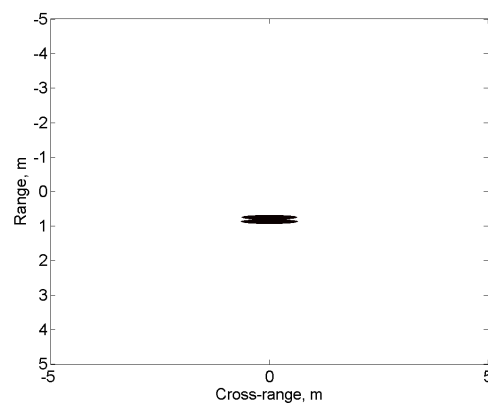
(c) Disjoint flight path segment 1 image segment mask.



(d) Disjoint flight path segment 2 image segment mask.

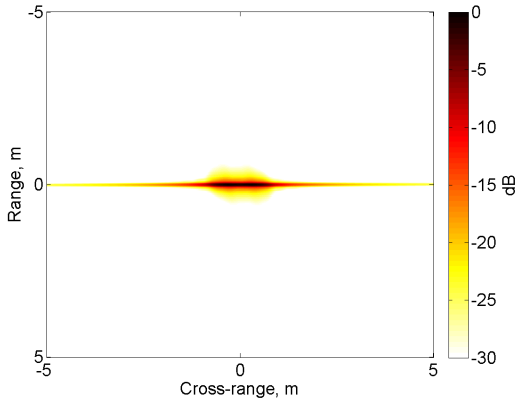


(e) Two-pass flight path segment 1 image segment mask.

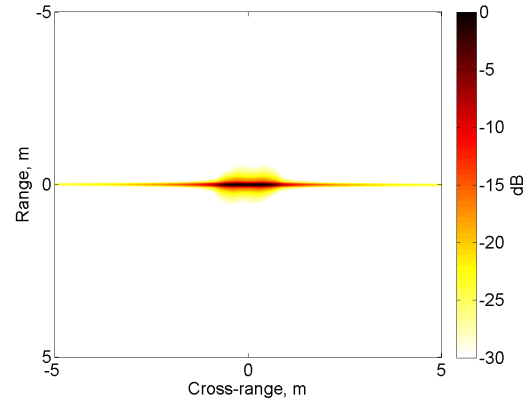


(f) Two-pass flight path segment 2 image segment mask.

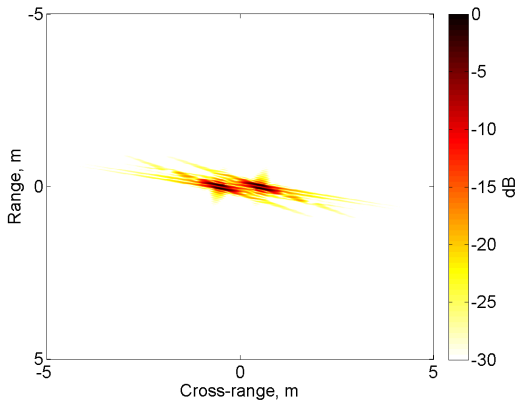
Figure 3.27: Scenario 2 Case 1 segment masks for the 2-D SAR images for each flight path segment.



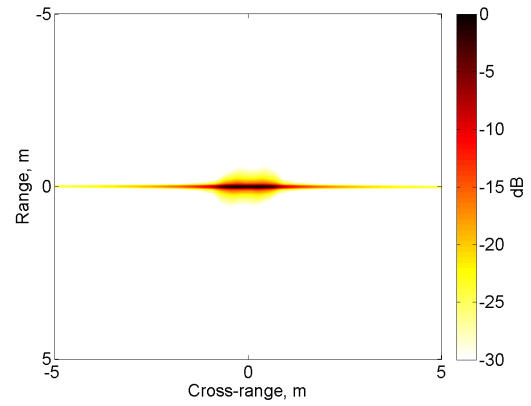
(a) Up-down flight path segment 1 image.



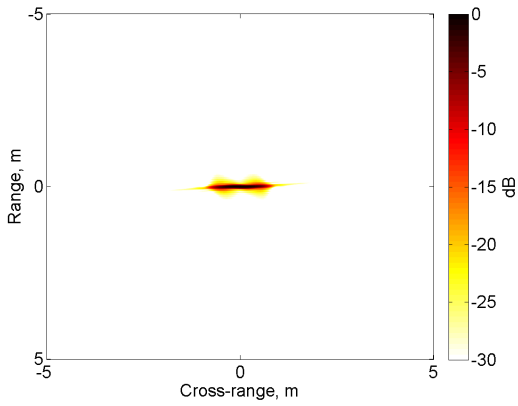
(b) Up-down flight path segment 2 image.



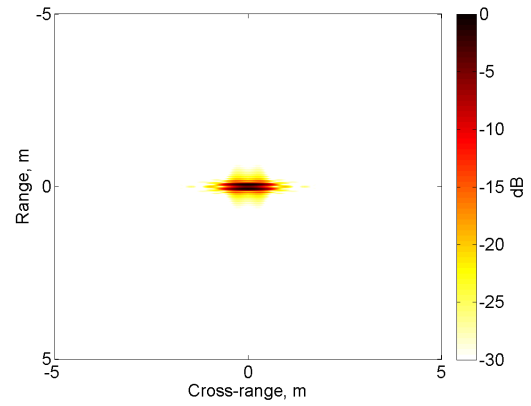
(c) Disjoint flight path segment 1 image.



(d) Disjoint flight path segment 1 image.

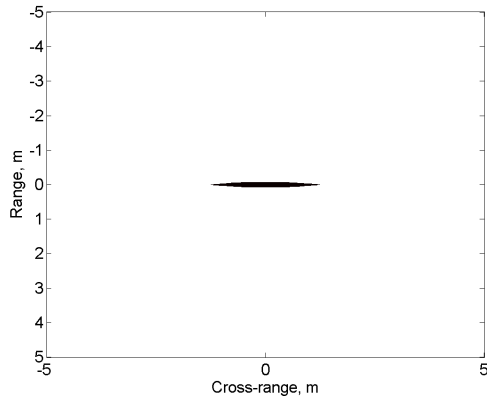


(e) Two-pass flight path segment 1 image.

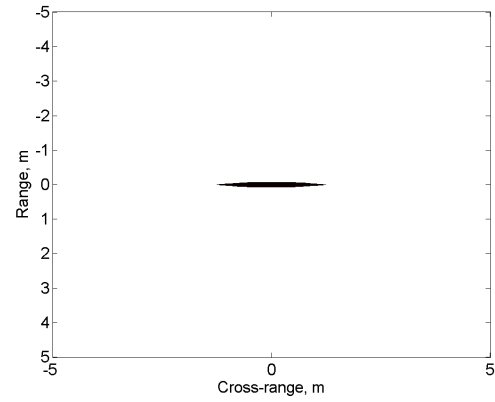


(f) Two-pass flight path segment 1 image.

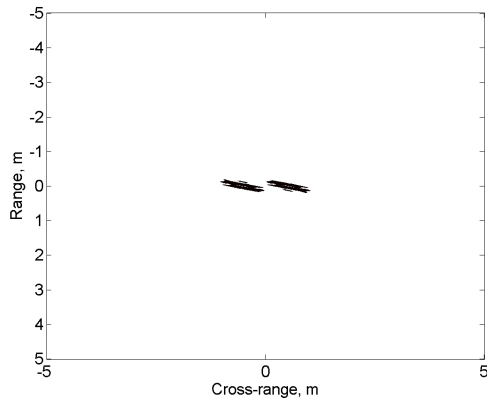
Figure 3.28: Scenario 2 Case 2 2-D SAR images for each flight path segment.



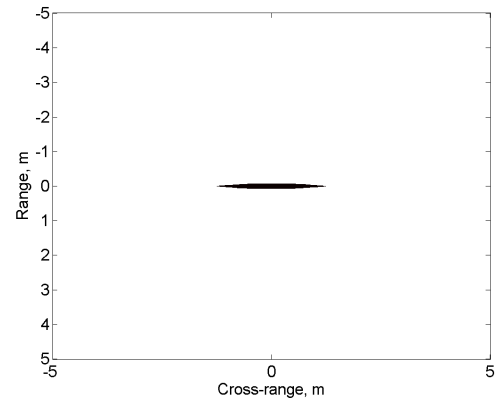
(a) Up-down flight path segment 1 image segment mask.



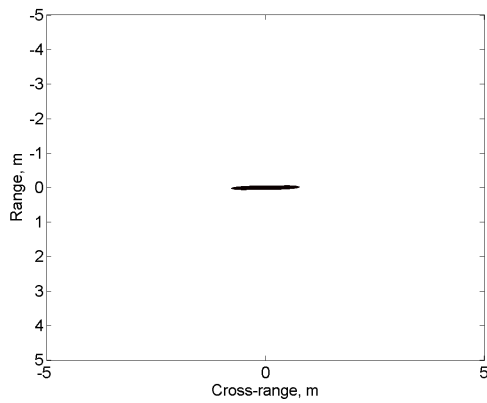
(b) Up-down flight path segment 2 image segment mask.



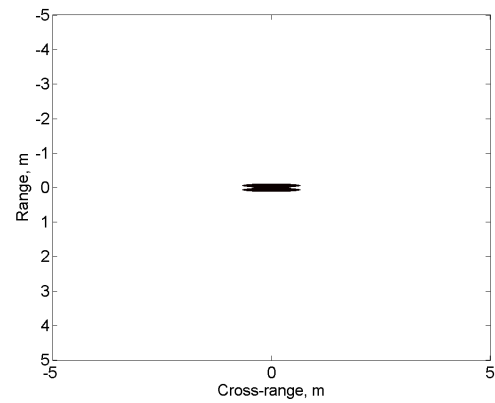
(c) Disjoint flight path segment 1 image segment mask.



(d) Disjoint flight path segment 2 image segment mask.

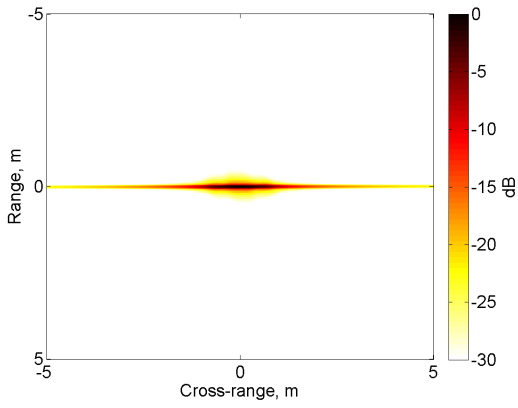


(e) Two-pass flight path segment 1 image segment mask.

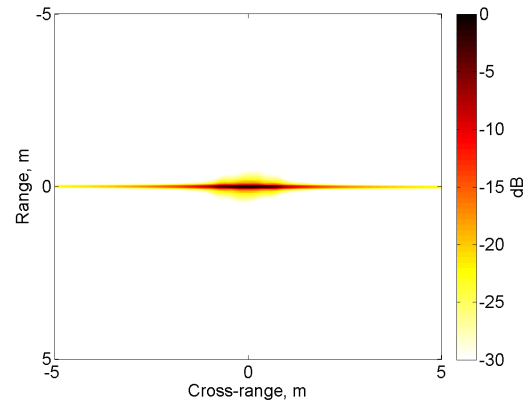


(f) Two-pass flight path segment 2 image segment mask.

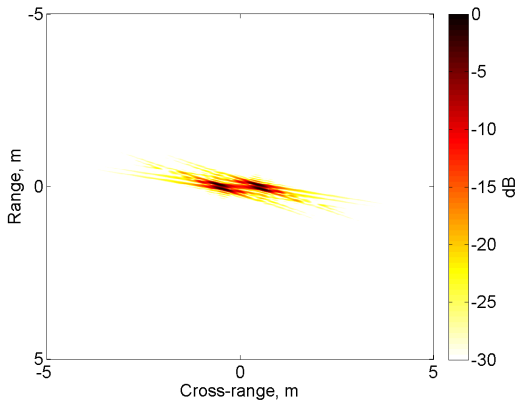
Figure 3.29: Scenario 2 Case 2 segment masks for the 2-D SAR images for each flight path segment.



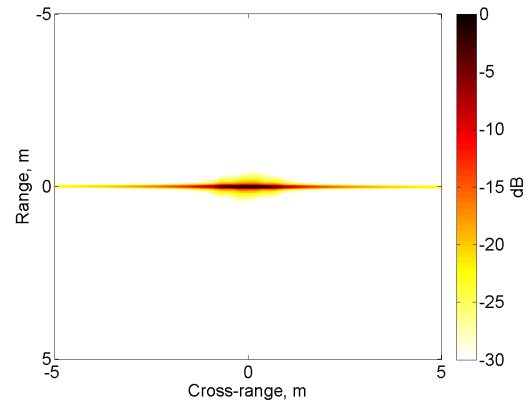
(a) Up-down flight path segment 1 image.



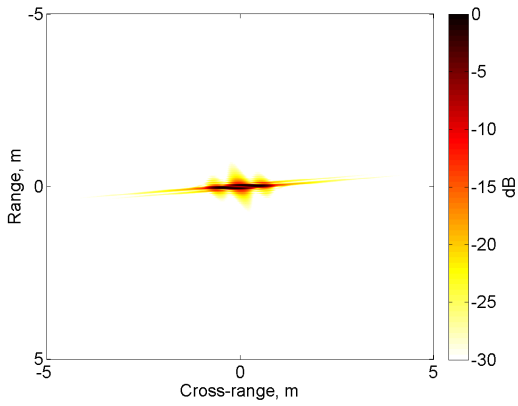
(b) Up-down flight path segment 2 image.



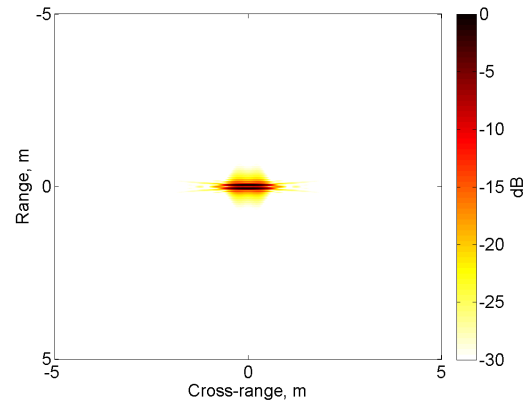
(c) Disjoint flight path segment 1 image.



(d) Disjoint flight path segment 1 image.

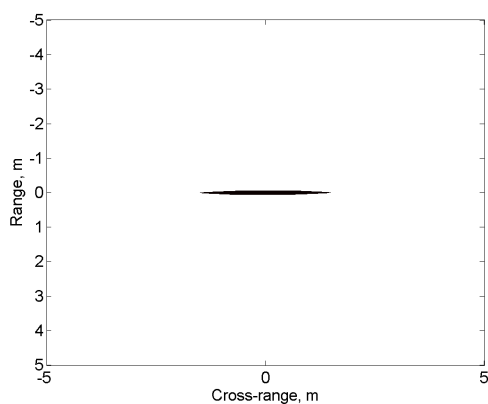


(e) Two-pass flight path segment 1 image.

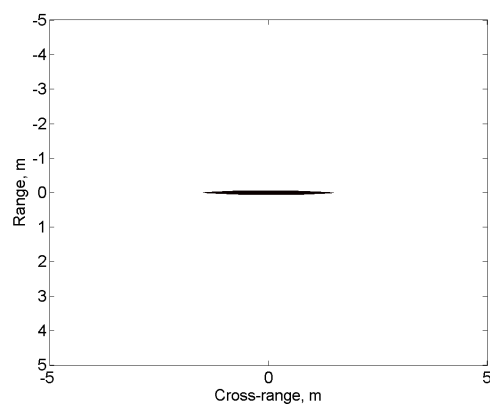


(f) Two-pass flight path segment 1 image.

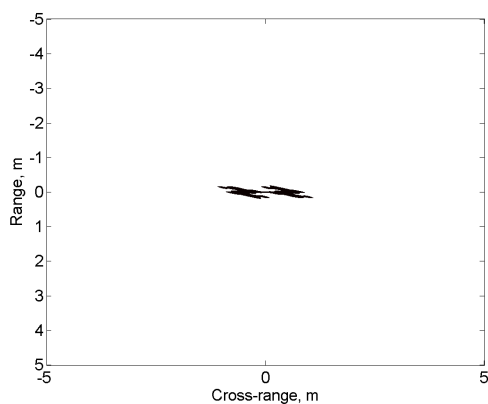
Figure 3.30: Scenario 2 Case 3 2-D SAR images for each flight path segment.



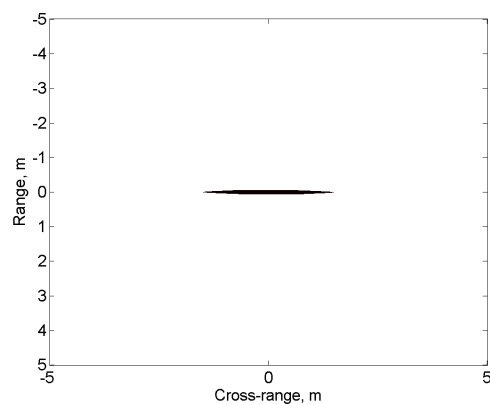
(a) Up-down flight path segment 1 image segment mask.



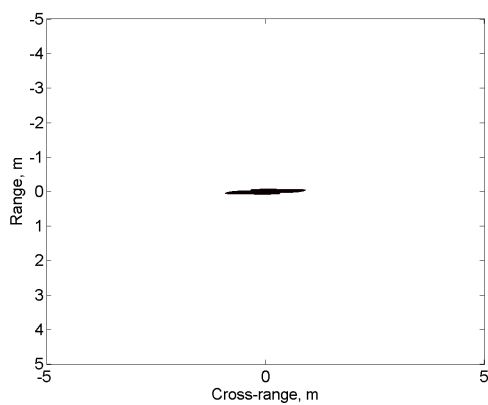
(b) Up-down flight path segment 2 image segment mask.



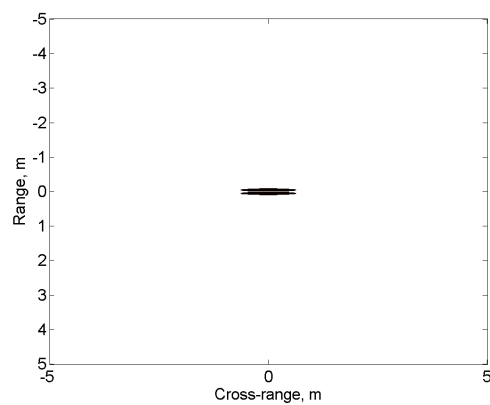
(c) Disjoint flight path segment 1 image segment mask.



(d) Disjoint flight path segment 2 image segment mask.



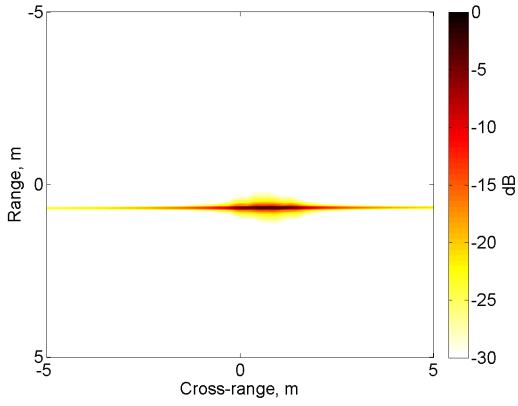
(e) Two-pass flight path segment 1 image segment mask.



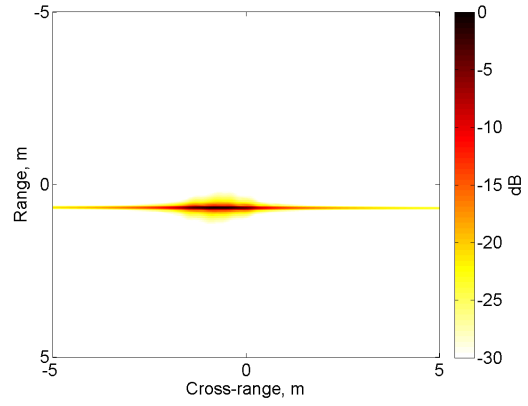
(f) Two-pass flight path segment 2 image segment mask.

Figure 3.31: Scenario 2 Case 3 segment masks for the 2-D SAR images for each flight path segment.

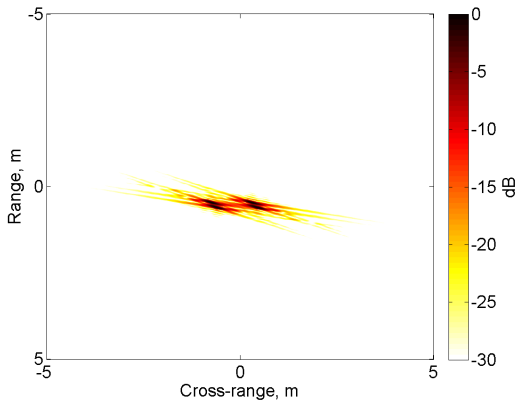




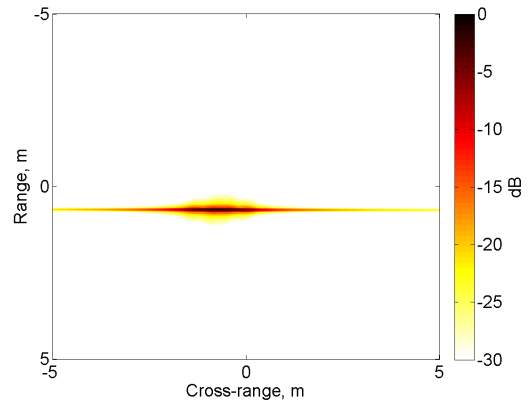
(a) Up-down flight path segment 1 image.



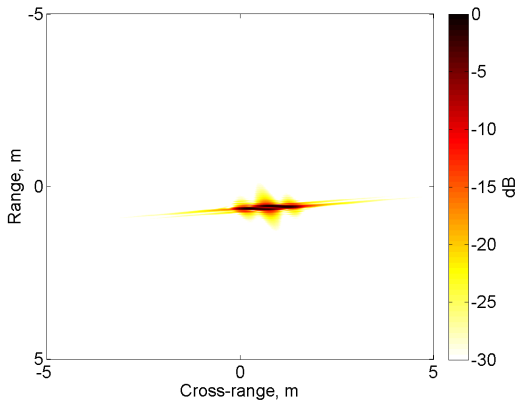
(b) Up-down flight path segment 2 image.



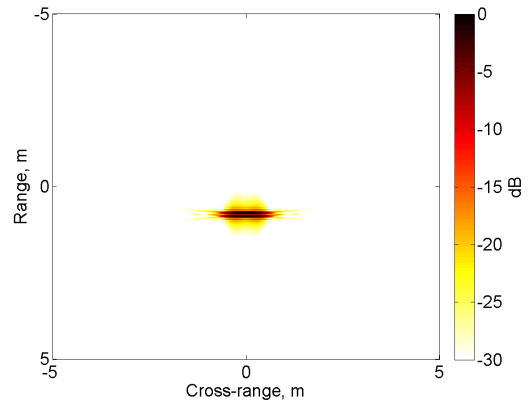
(c) Disjoint flight path segment 1 image.



(d) Disjoint flight path segment 1 image.

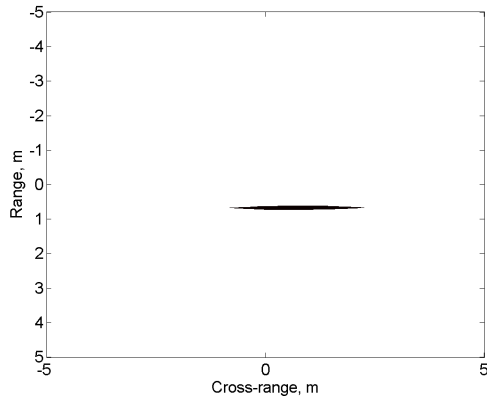


(e) Two-pass flight path segment 1 image.

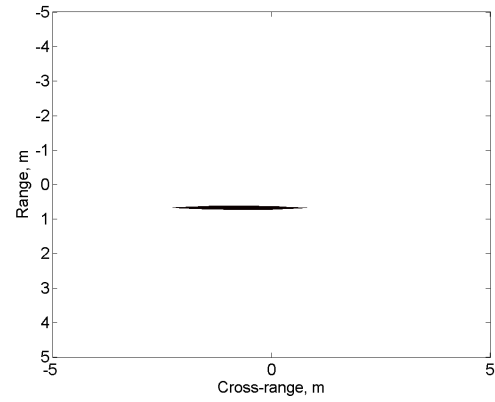


(f) Two-pass flight path segment 1 image.

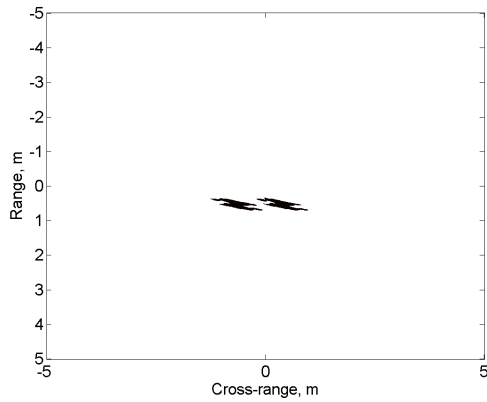
Figure 3.32: Scenario 2 Case 4 2-D SAR images for each flight path segment.



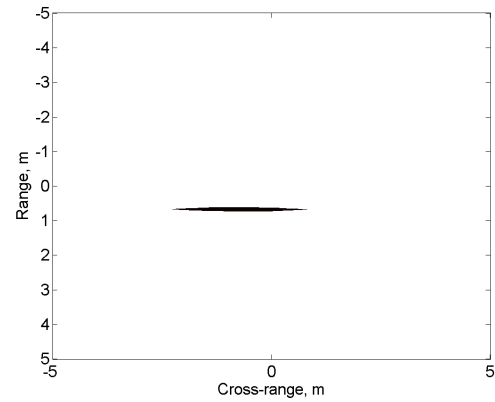
(a) Up-down flight path segment 1 image segment mask.



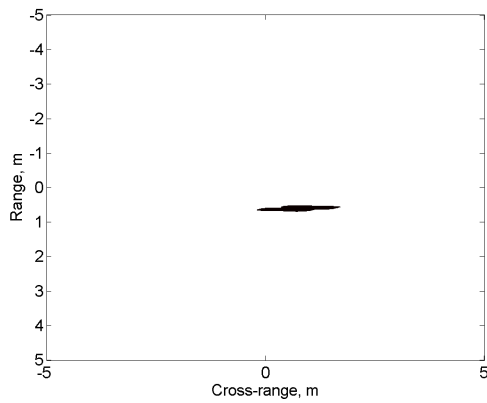
(b) Up-down flight path segment 2 image segment mask.



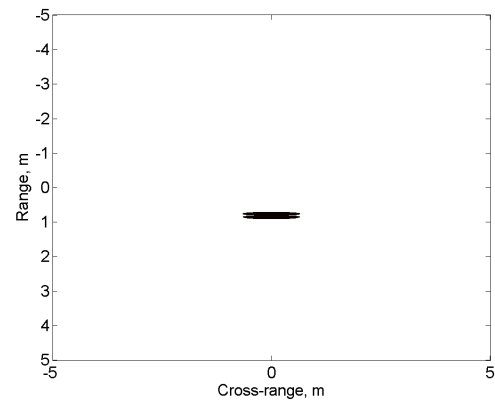
(c) Disjoint flight path segment 1 image segment mask.



(d) Disjoint flight path segment 2 image segment mask.

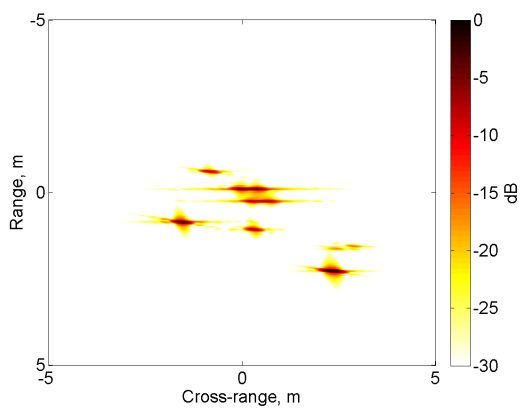


(e) Two-pass flight path segment 1 image segment mask.

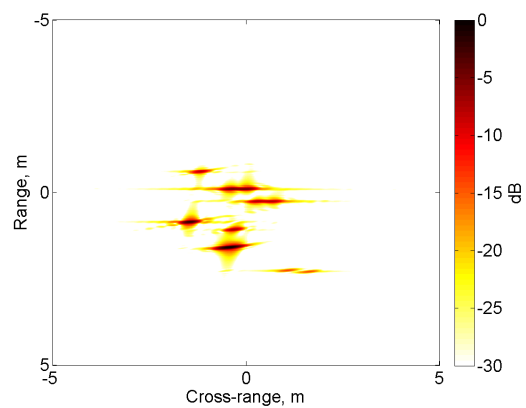


(f) Two-pass flight path segment 2 image segment mask.

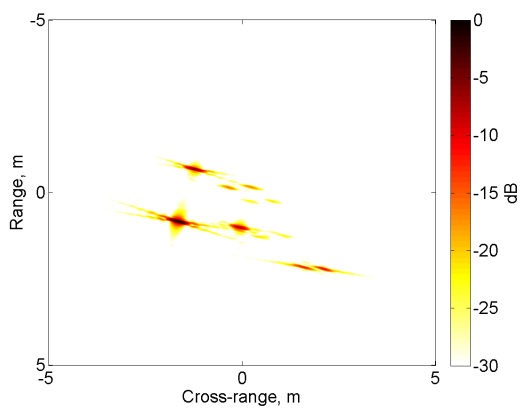
Figure 3.33: Scenario 2 Case 4 segment masks for the 2-D SAR images for each flight path segment.



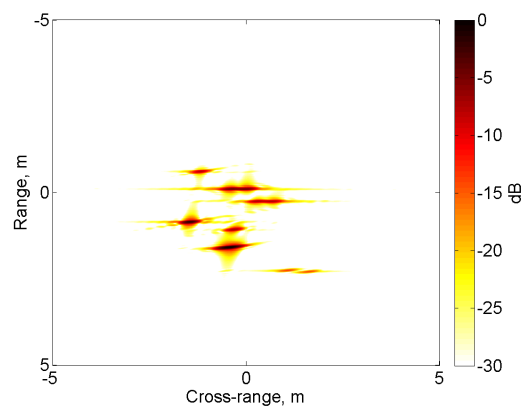
(a) Up-down flight path segment 1 image.



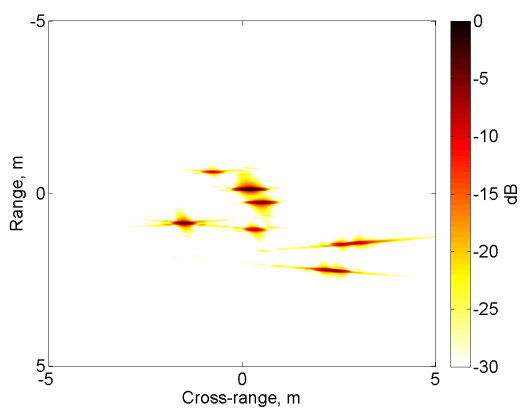
(b) Up-down flight path segment 2 image.



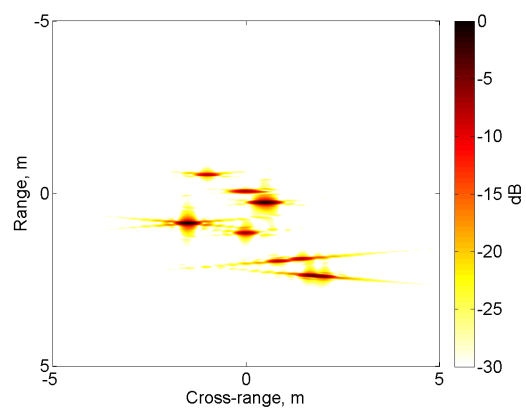
(c) Disjoint flight path segment 1 image.



(d) Disjoint flight path segment 2 image.

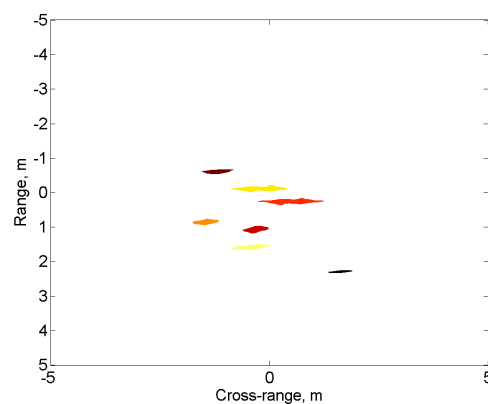
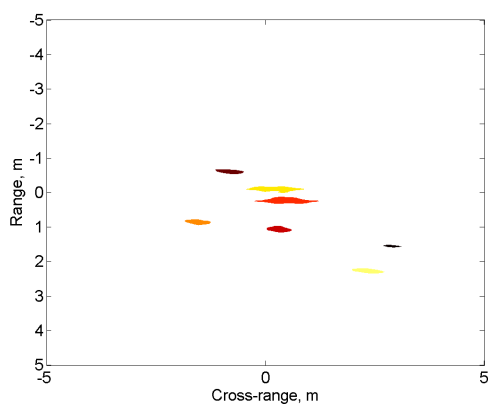


(e) Two-pass flight path segment 1 image.

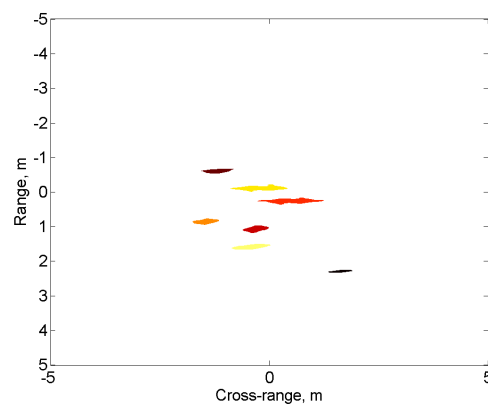
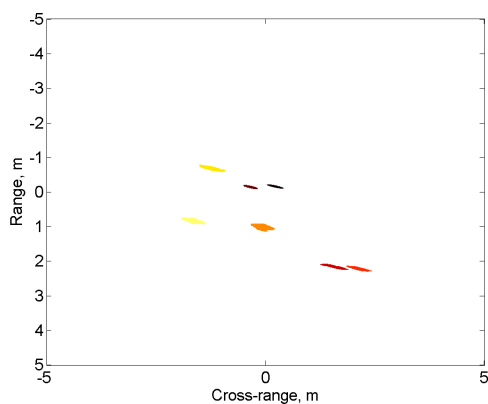


(f) Two-pass flight path segment 2 image.

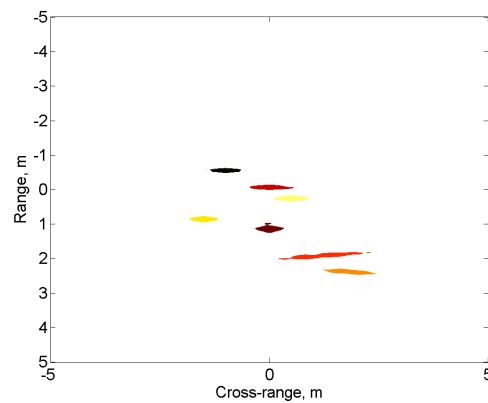
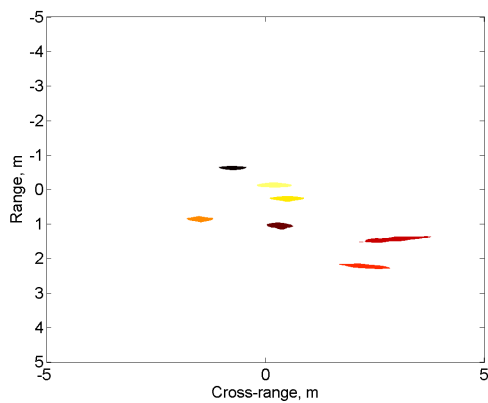
Figure 3.34: Scenario 3 2-D SAR images for each flight path segment.



(a) Up-down flight path segment 1 image segment mask. (b) Up-down flight path segment 2 image segment mask.



(c) Disjoint flight path segment 1 image segment mask. (d) Disjoint flight path segment 2 image segment mask.



(e) Two-pass flight path segment 1 image segment mask. (f) Two-pass flight path segment 2 image segment mask.

Figure 3.35: Scenario 3 segment masks for the 2-D SAR images for each flight path segment.

### 3.3.2 Model Order Estimation.

The number of scatterers in a scene is called the model order. Model order is estimated using the number of segments detected by the watershed algorithm. As demonstrated in Figures 3.26(b) and 3.27(b), a scatterer peak can split into two peaks in the image. The split phenomena occurs when an object with a length parameter is skew to the radar flight path and returns are summed in the backprojection equation. The pixel sums in the backprojection equation at the front and back of the object's length form higher peaks than pixels at the center of the object. The splitting supports the need for flight path diversity to capture the best return geometry. For example, a 1 m plate begins to split if the flight path is offset from the specular direction by more than two degrees.

In this thesis, model order is the average number of segments in the images. A segment is counted if it contributes at least 1% of the total energy in the scene. If there are 10 total unique segments, but 6 have less than 1% of the total energy, the model order would be 4. The model order estimates correctly identify a single scatterer in Scenario 1, each case of Scenario 2, and seven scatterers in Scenario 3. The image segments shown in Figures 3.25, 3.27, ... , 3.35 have an average number of segments equal to the model order.

A more complicated algorithm for model order estimation is possible; [18] associates peaks prior to model order estimation. Only scatterers that persist among each image are counted. This method could discount plates because a plate does not persist over varying flight segments due to its limited response extent. With that knowledge, the Scenarios in this thesis only see the plate because its orientation is always aligned near the flight path.

### 3.3.3 2-D Location Estimation.

Peak segmentation allows for accurate 2-D location estimation. A peak location is estimated using a center of mass calculation for the pixels included in the peak segment. The center of mass in the  $x$  direction is

$$\bar{x} = \frac{1}{A_{\text{total}}} \sum x_{gi} A_i, \quad (3.24)$$

where the index  $i$  is that of each pixel,  $A$  is the amplitude of the pixel, and  $x_{gi}$  is the pixel location in range. The same calculation is made in cross-range with

$$\bar{y} = \frac{1}{A_{\text{total}}} \sum y_{gi} A_i. \quad (3.25)$$

The 2-D locations are used to determine the 3-D location in Section 4.3 according to the mathematic solution in Section 3.1.1.2. Tables 3.16 - 3.18 provide the “true” 2-D locations and the 2-D center of mass results. The true 2-D locations are calculation using the layover equations in Chapter 3, Equations (3.1) - (3.10). These equations use the flight path grazing angle,  $\psi$ , and tilt angle,  $\eta$ . The derivation of these two angles for a flight path is in Appendix A. The grazing angles and tilt angles for the flight partitions used in this thesis are provided in Table 3.2.

Table 3.16: Scenario 1 2-D image segment true locations and center of mass calculated locations. The locations are given for each flight segment from Table 3.1. The locations are in meters.

Scenario/ Case	Flight Segment	True 2-D Location	Center of Mass 2-D Location
Scenario 1	Up-down 1	0.0, 0.0	0.0, 0.0
	Up-down 2	0.0, 0.0	0.0, 0.0
	Disjoint 1	0.0, 0.0	0.0, 0.0
	Disjoint 2	0.0, 0.0	0.0, 0.0
	Two-pass 1	0.0, 0.0	0.0, 0.0
	Two-pass 2	0.0, 0.0	0.0, 0.0

Table 3.17: Scenario 2 Cases 1-4 2-D image segment true locations and center of mass calculated locations. The locations are given for each flight segment from Table 3.1. The locations are in meters.

<b>Scenario/ Case</b>	<b>Flight Segment</b>	<b>True 2-D Location</b>	<b>Center of Mass 2-D Location</b>
Scenario 2/Case1	Up-down 1	0.67, 0.65	0.67, 0.72
	Up-down 2	0.67, -0.65	0.67, -0.72
	Disjoint 1	0.53, -0.14	0.53, -0.14
	Disjoint 2	0.67, -0.65	0.67, -0.72
	Two-pass 1	0.61, 0.70	0.61, 0.72
	Two-pass 2	0.81, 0.00	0.81, 0.00
Scenario 2/Case2	Up-down 1	0.0, 0.0	0.0, 0.0
	Up-down 2	0.0, 0.0	0.0, 0.0
	Disjoint 1	0.0, 0.0	0.0, 0.0
	Disjoint 2	0.0, 0.0	0.0, 0.0
	Two-pass 1	0.0, 0.0	0.0, 0.0
	Two-pass 2	0.0, 0.0	0.0, 0.0
Scenario 2/Case3	Up-down 1	0.0, 0.0	0.0, 0.0
	Up-down 2	0.0, 0.0	0.0, 0.0
	Disjoint 1	0.0, 0.0	0.0, 0.0
	Disjoint 2	0.0, 0.0	0.0, 0.0
	Two-pass 1	0.0, 0.0	0.0, 0.0
	Two-pass 2	0.0, 0.0	0.0, 0.0
Scenario 2/Case4	Up-down 1	0.67, 0.65	0.67, 0.72
	Up-down 2	0.67, -0.65	0.67, -0.72
	Disjoint 1	0.53, -0.14	0.53, -0.13
	Disjoint 2	0.67, -0.65	0.67, -0.72
	Two-pass 1	0.61, 0.70	0.61, 0.73
	Two-pass 2	0.81, 0.00	0.81, 0.00

Table 3.18: Scenario 3 2-D image segment true locations and center of mass calculated locations. The locations are given for each flight segment from Table 3.1. The shape types are not known a priori but shown here as information only. The locations are in meters.

Scenario/ Case	Shape Type	Flight Segment	True 2-D Location	Center of Mass 2-D Location
Scenario 3	plate	Up-down 1	-0.11, 0.18	-0.10, 0.21
		Up-down 2	-0.11, -0.18	-0.11, -0.20
		Disjoint 1	-0.15, -0.04	-0.15, -0.34
		Disjoint 2	-0.11, -0.18	-0.11, -0.20
		Two-pass 1	-0.13, 0.20	-0.13, 0.20
		Two-pass 2	-0.07, 0.00	-0.07, 0.01
Scenario 3	dihedral <sub>1</sub>	Up-down 1	0.25, 0.50	0.24, 0.49
		Up-down 2	0.25, 0.50	0.25, 0.50
		Disjoint 1	0.25, 0.50	-0.16, 0.22
		Disjoint 2	0.25, 0.50	0.25, 0.50
		Two-pass 1	0.25, 0.50	0.25, 0.49
		Two-pass 2	0.25, 0.50	0.25, 0.50
Scenario 3	dihedral <sub>2</sub>	Up-down 1	1.59, 2.64	2.27, 2.35
		Up-down 2	1.59, -0.44	1.58, -0.42
		Disjoint 1	1.26, 0.76	2.21, 2.13
		Disjoint 2	1.59, -0.44	1.58, -0.42
		Two-pass 1	1.45, 2.77	1.44, 2.92
		Two-pass 2	1.93, 1.10	1.91, 1.21
Scenario 3	trihedral	Up-down 1	1.07, 0.31	1.06, 0.31
		Up-down 2	1.07, -0.31	1.07, -0.31
		Disjoint 1	1.00, -0.07	1.01, -0.07
		Disjoint 2	1.07, -0.31	1.07, -0.31
		Two-pass 1	1.04, 0.33	1.04, 0.33
		Two-pass 2	1.14, 0.00	1.13, 0.00
Scenario 3	sphere	Up-down 1	-0.61, -0.82	0.62, -0.83
		Up-down 2	-0.61, -1.17	-0.61, -1.18
		Disjoint 1	-0.68, -1.22	-0.68, -1.22
		Disjoint 2	-0.61, -1.17	-0.61, -1.18
		Two-pass 1	-0.63, -0.75	-0.63, -0.75
		Two-pass 2	-0.55, -1.00	-0.55, -1.00
Scenario 3	cylinder	Up-down 1	2.28, 2.46	1.55, 2.89
		Up-down 2	2.28, 1.54	2.29, 1.63
		Disjoint 1	2.18, 1.91	2.15, 1.57
		Disjoint 2	2.28, 1.54	2.29, 1.63
		Two-pass 1	2.23, 2.50	2.22, 2.32
		Two-pass 2	2.39, 2.00	2.38, 1.84
Scenario 3	top-hat	Up-down 1	0.85, -1.55	0.85, -1.55
		Up-down 2	0.85, -1.45	0.85, -1.45
		Disjoint 1	0.83, -1.66	0.83, -1.65
		Disjoint 2	0.85, -1.45	0.85, -1.45
		Two-pass 1	0.85, -1.50	0.85, -1.50
		Two-pass 2	0.85, -1.50	0.85, -1.50



The 2-D location results in Tables 3.16 - 3.18 demonstrate the principle of layover. The plate in Scenario 1, Scenario 2 Cases 2 and 3, and  $\text{dihedral}_1$  from Scenario 3 all have their center reflection point in the image ground plane. Therefore, each of these cases show the same 2-D, non-projected location for each flight path.

Layover is demonstrated for the other objects not in the ground plane. Having their scattering reflection point above the ground plane projects their location to the image ground plane. The flight path partitions have different slant plane angles and accompanying projection angles. The unique layover is evident in the 2-D SAR images and segments in Figures 3.26 and 3.27. The plate is at  $(x = 0 \text{ m}, y = 0 \text{ m}, z = 1.05 \text{ m})$ . Being above the ground plane, each peak is projected to a unique location for each flight partition. The true and calculated locations in Tables 3.16 - 3.18 show the relative layover numerically. The Two-pass second segment is at the highest elevation; therefore, each range location is closer than the others. The Two-pass first segment has the largest tilt angle producing the largest cross-range 2-D locations.

The layover error occurs because the slant plane layover projection angles approximate the 2-D projection location in the ground plane. The backprojection integral in Equation (2.1) sums the return from each HRR. Each HRR is taken from a unique azimuth and elevation angle. The projection vector for each HRR is slightly different than the slant plane layover angles. Some offset can occur in the resultant sum of projected HRRs.

The layover error is evident in Scenario 3. The  $\text{dihedral}_2$  is the furthest from the ground plane at  $z = 2.50 \text{ m}$ . It has the second largest 2-D location errors,  $y_{g1,error} = 0.15 \text{ m}$ ,  $y_{g2,error} = 0.11 \text{ m}$ . The reflection point of the cylinder is the next highest at  $z \approx 1.5 \text{ m} \sin(30^\circ) = 0.75 \text{ m}$  and carries the largest errors,  $y_{g1,error} = 0.18 \text{ m}$ ,  $y_{g2,error} = 0.16 \text{ m}$ . The approximation in the height calculation is because each flight path grazing angle is slightly different. The errors in the 2-D locations are what cause the error in the

3-D location estimates as will be discussed in Section 4.3 where the 3-D estimates are provided.

The cylinder has a larger 2-D location error because the orientation yaw slightly tilts the cylinder. The amplitude of HRRs to the direction of the pitch are higher so the 2-D peak is slightly weighted. The center of mass calculation from Equation (3.25) shifts the peak center so the 2-D location has more error.

### **3.3.4 Peak Association.**

The peak locations are used to associate the peaks between each image pair. Association is needed to pair the correct 2-D location set from the image to compute the 3-D location. The image peak locations are matched using the relative layover angles.

An object's 2-D peak locations are used to estimate the 3-D location estimate. To make the 3-D estimate for an object, the peak corresponding to that object must be distinguished from the others in the scene. Association is the process of mapping the each peak in a scene to each object.

Peak association is accomplished using the layover projection angles from each flight partition. The derivation of the layover angles is provided in Appendix A. A flight partition at a higher elevation will project an object closer to the radar. The angle of flight path ascent or descent determines the angle of layover in the cross-range direction. The relative layover angles between two images limit how far a peak can move between the images. Association uses relative range and cross-range translation to match the peaks.

An allowable range translation example is given in Equation (3.27). The layover angles from Two-pass segment 1 and segment 2 are ( $\psi = 30.2^\circ$ ,  $\eta = 33.8^\circ$ ) and ( $\psi = 37.6^\circ$ ,  $\eta = 0.0^\circ$ ), respectively. Assuming a maximum object height of 4 m, the range that a scatterer in Two-pass segment 1 can move relative to the location in segment 2 is  $x_{g1} \in [x_{g2} - 0.75\text{m}, x_{g2}]$ . The cross-range that a scatter can move relative to the location

in segment 2 is  $y_{g1} \in [y_{g2}, y_{g2} + 2.68\text{m}]$ . The result is shown mathematically with

$$\begin{aligned}
x_{g1} &= x + z \tan \psi_1 \\
x_{g2} &= x + z \tan \psi_2 \\
x_{g1} - x_{g2} &= z(\tan \psi_1 - \tan \psi_2) \\
&= 4 \text{ m } (\tan(30.2^\circ) - \tan(37.6^\circ)) \\
&= -0.75 \text{ m} \\
x_{g1} &= x_{g2} - 0.75 \text{ m.}
\end{aligned} \tag{3.26}$$

and

$$\begin{aligned}
y_{g1} - x_{g2} &= z(\tan \eta_1 - \tan \eta_2) \\
&= 4 \text{ m } (\tan(33.8^\circ) - \tan(0^\circ)) \\
&= 2.68 \text{ m} \\
y_{g1} &= y_{g2} + 2.68 \text{ m.}
\end{aligned} \tag{3.27}$$

The example result is also shown graphically in Figure 3.36

In Figure 3.34 the different flight partition images show varying levels of amplitudes for each scatterer. Also, splitting occurs for some scatterer peaks. The shapes are oriented such that their specular is detected for their 2-D image pair from Table 3.3. Therefore, the split peaks do not affect the 2-D location estimates needed for the 3-D location estimation.

The splitting demonstrates why some 2-D location estimates are very far from their estimates. In Figure 3.34(c), the peaks for the sphere, top-hat, and trihedral do not split and are estimated correctly, as shown in Table 3.18. The splitting causes poor peak matches for the other shapes. Consequently the 2-D location estimates are poor. Splitting scatterer peaks causing poor 2-D location estimates provides areas of future work to account for splitting phenomena. The split peaks do not affect the results in this thesis, as all peaks are correctly associated using their location in each 2-D SAR image.

In summary, Step 1A analyzes the collection flight path and radar parameters. Step 1B pre-processes the range of possible errors that will be used for bounding in Step 2.

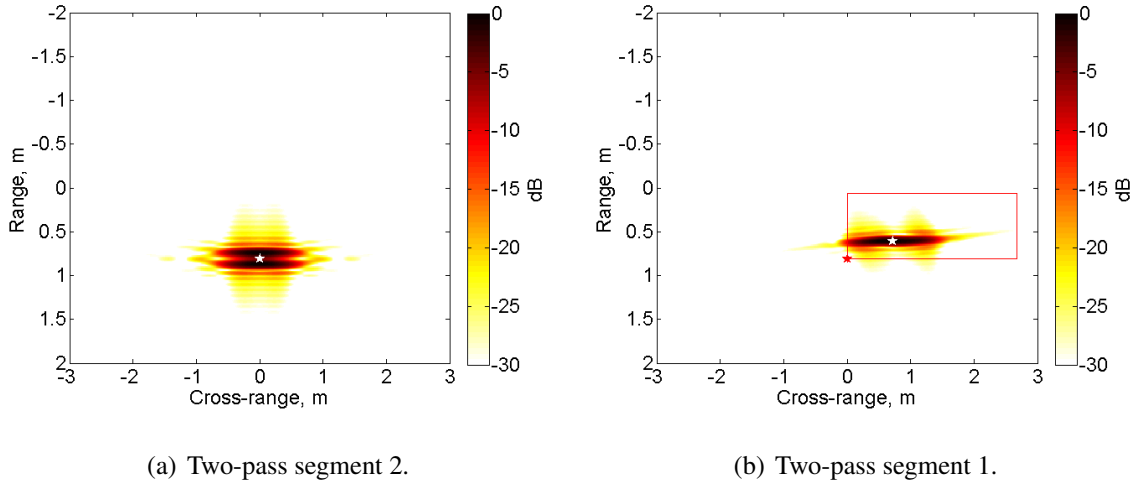


Figure 3.36: Using the Two-pass images from Scenario 2 Case 1, peak association is demonstrated. Starting with the peak location in segment 2 in Figure 3.36(a), the possible area allowed for layover, given the difference in grazing and tilt angles, is boxed in red in Figure 3.36(b). The red star denotes the peak location from segment 2 in Figure 3.36(a). The plate is at  $z = 1.05$ , so the layover location is different and falls within the possible layover range and cross-range.

By detecting the full range of possible errors, the estimates in Step 2 can be bound with confidence that the true parameter lies within the bound.

In Step 1C, the PH data of the scene under test is collected. In this thesis the PH data is generated according to the models from [1]. Two-dimensional SAR images are formed from each flight partition and then segmented. The model order, 2-D peak locations, and peak associations are all determined for use in Step 2.

The model order provides the number of scatterers to be estimated. The segment size is used for length estimation. The peak associations are necessary for 3-D location estimation. The 3 Scenarios will be carried through Chapters 4 and 5, so evaluation of each algorithm step can be analyzed.

#### IV. Initial Shape Type Estimation and Parameter Estimation and Bounding

Step 1 provides model order and image information necessary for parameter estimation. In Step 2, multiple steps accomplish initial parameter estimation. The estimation process is shown in Figure 4.1. Initial estimates are combined with preprocessed error analysis to limit the possible parameter subspace. The error analysis is completed in Step 1B using the chosen flight path in Step 1A for each shape type and multiple parameter permutations. The permutations are chosen to determine the worst errors for any shape parameter set that will be encountered; the scene scatterers and their parameters are not known a priori. The limited parameter subspace is output from Step 2 and allows for more accurate and efficient dictionary formation and search in Step 3, whose results are in Chapter 5.

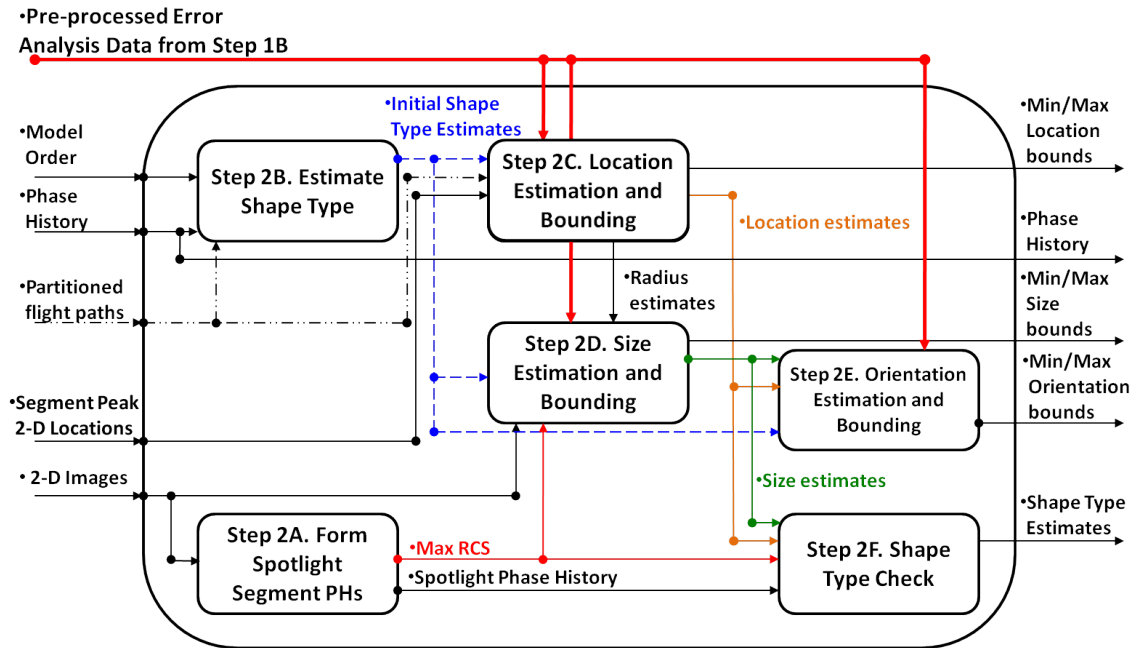


Figure 4.1: Steps to complete parameter estimation and bounding.

The pre-processed possible error ranges from Step 1 are input into Step 2, but one pre-estimation step is still needed. Step 2A spotlights the PH data to separate the PH data into the PH of each individual scatterer. The separation allows for better RCS estimation, which is used for size estimation in Section 4.4. The spotlight PHs allow for direct comparison against dictionary PHs with less error due to other scatterers' PHs. In this thesis, perfect spotlighting is assumed and individual PHs are generated for each shape instead.

Estimation commences with the completion of all the pre-processing. In Step 2B, The SPLIT algorithm [26] estimates the shape type using the frequency and polarization responses of scatterer peak pixels in the 2-D images. In Step 2C, the 3-D location of each scatterer is estimated using its 2-D image peak locations. Step 2D estimates the size parameters using the length of the segments in the images, the RCS from the spotlight PH, and the radius estimates found along with the location estimates. Step 2E estimates the orientations parameters using a coarse-to-fine PH correlation. In Step 2F, the initial parameter estimates from Step 2B are checked for feasibility. The final shape type estimates with their corresponding parameter bounds are passed to Step 3 for final estimation via dictionary formation and search.

#### **4.1 Step 2A: Spotlight Partitioned Flight Path Phase Histories**

Before estimating the shape type and object parameters, the 2-D images are used to produce spotlight PH data. Spotighting extracts the pixels for a single scatterer in an image using a window function. Generally, a rectangular window function is used. The image spotlight is transformed from the image domain back to the PH using an inverse backprojection. Although the theory of spotlighting exists, code has not been written for this data set to invert the backprojection integral in Equation (2.1).

In this thesis, the scatterer spotlight PHs are approximated by generating them directly from the scattering model equations for each object. The spotlight PHs are downsampled relative to the original collection sample sizes in frequency and azimuth.

The downsampling accounts for the decrease in scene extent of the rectangle window used to separate the peaks (see Equations (2.2) and (2.3)).

A window of 1 m in range and 2.5 m in cross-range appears to be the correct size for the peaks in the images. This window relates to sample number decreases to 21 samples in frequency and 11 samples in azimuth. The calculations for the number of samples are

$$\begin{aligned}
 E_{\text{range}} &= \frac{c}{2\delta f} \\
 \delta f &= \frac{c}{2E_{\text{range}}} \\
 &= \frac{3 \times 10^8 \text{ m/s}}{2(1 \text{ m})} \\
 &= 1.5 \times 10^8 \text{ Hz} \\
 N_{\text{samples},f} &= \frac{B}{\delta f} + 1 \\
 &= \frac{3 \times 10^9 \text{ Hz}}{1.5 \times 10^8 \text{ Hz}} + 1 \\
 &= 21 \text{ samples.}
 \end{aligned} \tag{4.1}$$

And

$$\begin{aligned}
 E_{\text{cross-range}} &= \frac{\lambda_{\min}}{2\delta\phi} \\
 \delta\phi &= \frac{\lambda_{\min}}{2E_{\text{cross-range}}} \\
 &= \frac{0.0857 \text{ m}}{2(2.5 \text{ m})} \\
 &= 0.017 \text{ radians} \approx 1^\circ \\
 N_{\text{samples},\phi} &= \frac{\text{azimuth extent}}{\delta\phi} + 1 \\
 &= \frac{10^\circ}{1^\circ} + 1 \\
 &= 11 \text{ samples.}
 \end{aligned} \tag{4.2}$$

The spotlighted PH serves two purposes. The squared magnitude of the maximum PH sample gives an estimate of the RCS. The spotlighted PH prevents a separate object in the

scene from adding significant energy to the maximum amplitude. The RCS is needed for size estimation in Step 2D in Section 4.4.

The segregated spotlight PHs secondly allow easier PH comparison. The initial orientation parameter estimation uses coherency matching against a single object's PH in Step 2E in Section 4.5. The final parameter estimates from dictionary search in Section 5.2 also compare PHs one object at a time. Correlation and LS fit of a single object are inherently poor with multiple objects' PH contributing.

The image data from Section 3.3 with the RCS and spotlighted PHs provide all the information needed for initial estimates. The following sections detail how these pieces of information are used for Steps 2B-2F from Figure 4.1.

#### **4.2 Step 2B: Initial Shape Type Estimate - The SPLIT Algorithm**

Shape type estimates decrease the number of computations needed. Without an estimate of shape type, calculations would be needed to estimate the parameters for each shape type. Later the estimated parameters would have to be examined to determine feasibility of each shape type. Radar PH data does not provide shape type information directly. Initial shape type estimates of each object are made using the spectrum parted linked image test (SPLIT) algorithm from [26].

The SPLIT algorithm estimates shape type using the frequency response and polarization response of the image data. The plate and sphere are classified together in the SPLIT algorithm; all other canonical shapes are uniquely classified. The shape type estimates include a confidence measure [26]. The confidence is a probabilistic measure of how well the selected shape type matches the frequency and polarization response integer values versus choosing the other shape types.

The frequency response is dependent on the curvature of an object. The response proportionality is shown with the proportionality

$$M \propto f^{\alpha/2}. \quad (4.3)$$



The  $M$  variable represents the PH response from Table 2.3. The dependence is determined from the GO and GTD. The alpha values for different shape types are given in Table 4.1.

Table 4.1: Frequency response values for each canonical shape type [1],[26, Sect. 2.2.1].

Scattering Geometry	$\alpha$
plate, dihedral, trihedral	2
cylinder, top-hat	1
sphere	0

The frequency dependencies are reflected in the canonical shape PH models from Table 2.3. The frequency term the PH models is in the wavenumber,  $k = \frac{2\pi f}{c}$ . The plate, dihedral, and trihedral equations all include the frequency term to the 1st power ( $\alpha = 2$ ,  $\alpha/2 = 1$ ). The cylinder and top-hat have  $k$  to the one half power. The sphere has no dependency on frequency.

The polarization response predicts either odd or even bounce behavior according to the number of radar wave reflections induced by the shape. Fuller [26, Sect. 2.2.3] uses a Krogager decomposition of the Sinclair scattering matrix to estimate odd/even bounce. If insufficient data is available for shape type determination, the odd or even bounce limits the shape type estimate to the odd (plate, trihedral, sphere, cylinder) or even (dihedral, top-hat) shapes.

In this thesis, the confidence measure is used as a threshold to determine whether or not to accept the shape estimate. The threshold used for shape type acceptance is 0.90. The exception is the trihedral that has a threshold of 0.80. The thresholds are set after running multiple trials of the SPLIT code and desiring a negligible probability of false alarm. The threshold was raised for each trial of a false positive. If the specific shape type does not meet the threshold, the shape type estimate defaults to the odd or even bounce behavior.

The SPLIT code graphically displays the shape type estimates and polarization bounce. The SPLIT image displays are shown in Figures 4.2 and 4.4. The shape

type estimate results with confidence measurements and final shape type choices for the scenarios are provided in Table 4.2. The even or odd polarization response are correct for each shape type and are indicated in the images by the green and red pixels. The spread of the polarization response occurs because the polarization response is tested per pixel. The pixel response is spread with the peaks due to the cross-range resolution.

In Scenario 1, the SPLIT algorithm correctly detects a plate/sphere response but the confidence does not meet the threshold so all odd shapes are estimated. In Scenario 2, Cases 1 and 2 correctly detect the plate/sphere with a confidence measure above the threshold a plate/sphere is the estimated type. Cases 3 and 4 from Scenario 2 do not detect a shape type, so all odd shape types are estimated.

In Scenario 3, all even or odd polarizations are correct. Only the trihedral, sphere, and top-hat have detected shape types. All three have sufficient confidence measures and are able to limit the shape type estimates as shown in Table 4.2.

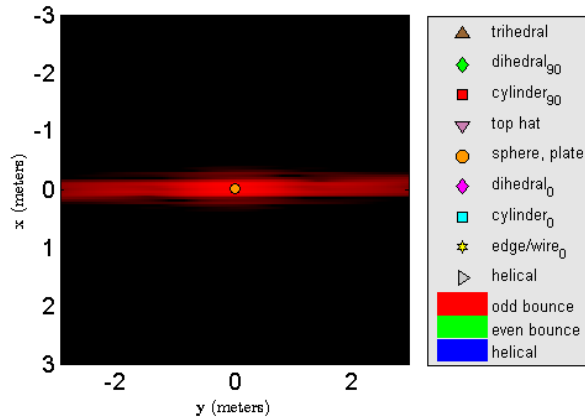


Figure 4.2: Scenario 1 SPLIT shape type estimate and polarization bounce image.

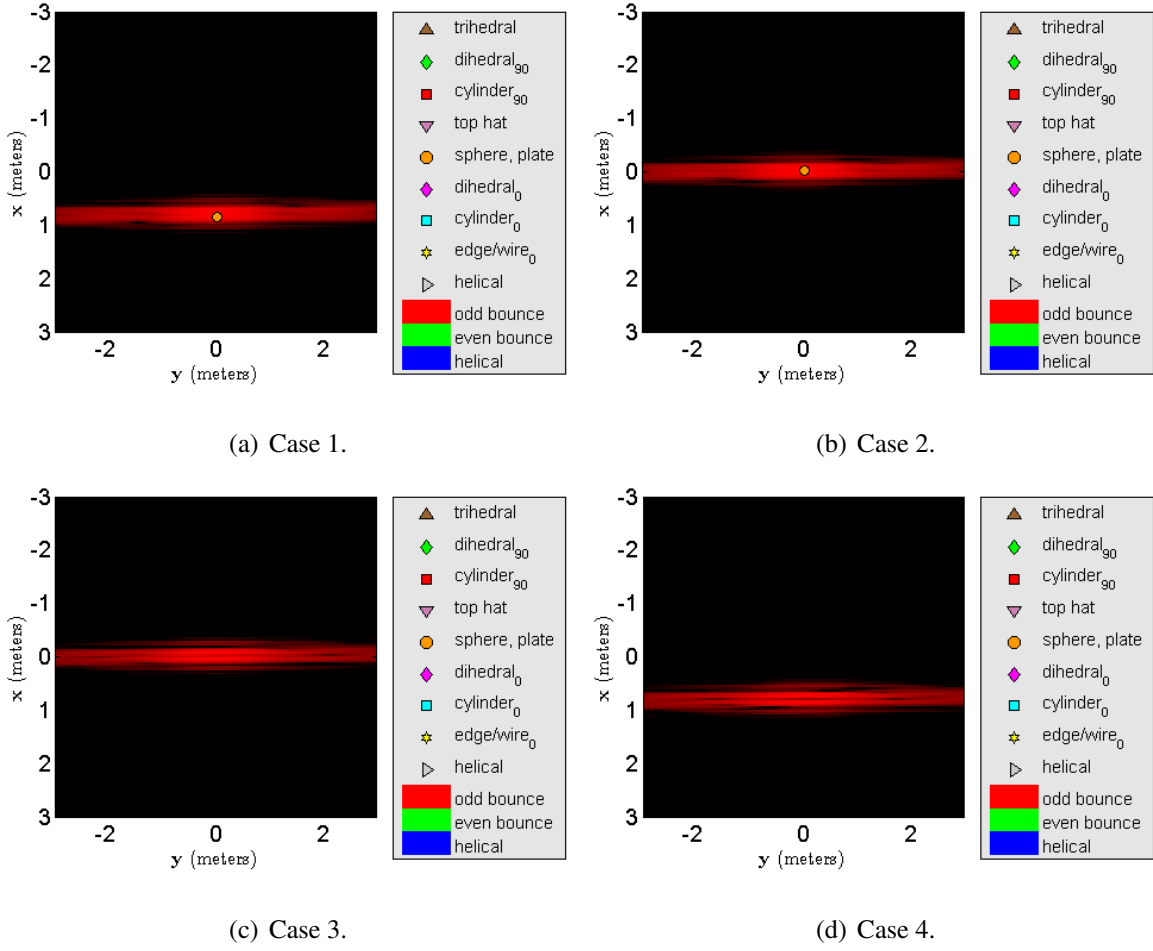


Figure 4.3: Scenario 2 SPLIT shape type estimate and polarization bounce images for each of the four cases.

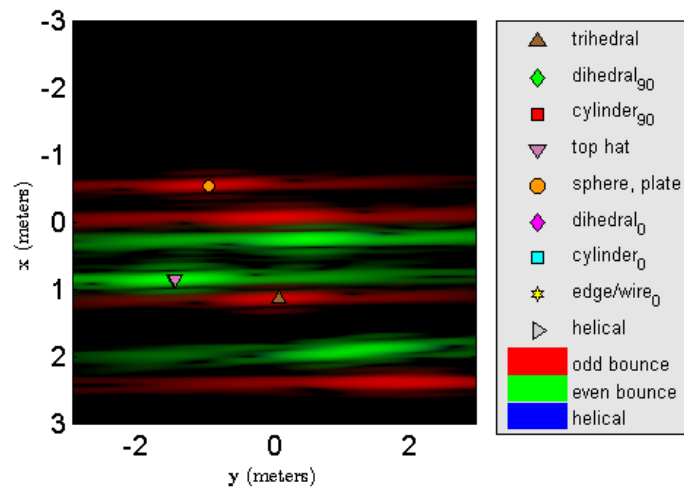


Figure 4.4: Scenario 3 SPLIT shape type estimates and polarization bounce image.

Table 4.2: True shape types and SPLIT algorithm shape type estimates for each scenario.

Scenario 1

<b>True shape type</b>	plate
<b>Detected shape type</b>	plate/sphere
<b>Confidence</b>	0.87
<b>Polarization</b>	odd
<b>Shape Estimate</b>	plate, trihedral, sphere, cylinder

Scenario 2

<b>Case 1</b>	<b>True shape type</b>	plate
	<b>Detected shape type</b>	plate/sphere
	<b>Confidence</b>	0.91
	<b>Polarization</b>	odd
	<b>Shape Estimate</b>	plate, sphere
<b>Case 2</b>	<b>True shape type</b>	plate
	<b>Detected shape type</b>	plate/sphere
	<b>Confidence</b>	0.92
	<b>Polarization</b>	odd
	<b>Shape Estimate</b>	plate, sphere
<b>Case 3</b>	<b>True shape type</b>	plate
	<b>Detected shape type</b>	–
	<b>Confidence</b>	–
	<b>Polarization</b>	odd
	<b>Shape Estimate</b>	plate, trihedral, sphere, cylinder
<b>Case 4</b>	<b>True shape type</b>	plate
	<b>Detected shape type</b>	–
	<b>Confidence</b>	–
	<b>Polarization</b>	odd
	<b>Shape Estimate</b>	plate, trihedral sphere, cylinder

Scenario 3

<b>True shape</b>	plate	dihedral <sub>1</sub>	dihedral <sub>2</sub>	trihedral	sphere	cylinder	top-hat
<b>Detected shape</b>	–	–	–	trihedral	plate/sphere	–	top-hat
<b>Confidence</b>	–	–	–	0.88	0.99	–	0.99
<b>Polarization</b>	odd	even	even	odd	odd	odd	even
<b>Shape Estimate</b>	plate, trihedral, cylinder, sphere	dihedral, top-hat	dihedral, top-hat	trihedral	plate, sphere	plate, trihedral, cylinder, sphere	top-hat

### 4.3 Step 2C: Initial Location Estimation and Bounding

The 3-D location estimate of a shape is solved using at least two peak locations in 2-D SAR images generated in Step 1C. The mathematic solution of solving for the 3-D location is detailed in Section 3.1.1.2. In this thesis, the peak locations of two images are used for each 3-D estimate. Each image is formed from a unique partition of the flight path. The flight path partitions for 2-D location estimation of each shape type are included in Table 3.3 with the previous discussion of the flight path analysis in Section 3.1.1.3.

The 2-D location estimates are provided in Section 3.3 in Tables 3.16 - 3.18. The 3-D locations calculated from the 2-D locations and flight path parameters are in Tables 4.3 - 4.5 in the  $x$ ,  $y$  and  $z$  columns. Tables 4.3 - 4.5 show all the results for Step 2, although Steps 2D - 2F have not yet been completed. Providing the results in a single table shows the initial estimation results more succinctly. The following sections refer back to the tables. In the shape type column, all shape types listed are the initial shape type estimates from the SPLIT algorithm in Step 2B. The shapes with a strikethrough are those removed in Step 2F by the shape type check. The  $x$ ,  $y$ ,  $z$  columns are for this Step 2C. The  $L$ ,  $H$ ,  $r$  columns are for the shape estimates in Step 2D. The  $\gamma$ ,  $\theta$ ,  $\phi$  columns are the orientation estimates in Step 2E. Finally, the Shape Check column provides the reason why a shape is discarded in Step 2F.

The accuracy of the 3-D location estimates are dependent on the location accuracy of the 2-D estimates. As determined in Section 3.3.3, the 2-D location estimate accuracy decreases as the location of a shape's reflection point moves away from the ground plane. Scenario 1, Scenario 2 Cases 2 and 3, and dihedral<sub>1</sub> from Scenario 3 are all in the ground plane. The resultant 3-D location estimates are within 0.01 m.

The 3-D location estimate errors increase for the plates in Scenario 2 Cases 1 and 4 and the other shapes in Scenario 3. In Scenario 2 Cases 1 and 4, the plates are at  $z = 1.05$

and the 3-D error increase to 0.12 m and 0.13 m, respectively. 3-D location estimation error is expected since the 2-D image layover locations have an inaccuracy of  $y_{g,error} = 0.07$  m.

Scenario 3 shows the same relation between 2-D location estimate error and 3-D location error when a shape reflection point is above the ground plane. Dihedral<sub>2</sub> is the furthest above the ground plane at  $z = 2.5$  m, has a 2-D location error of  $y_{g1,error} = 0.15$  m, and a 3-D location error of  $y_{error} = 0.11$  m. The cylinder has the largest 2-D location error of  $y_{g1,error} = 0.18$  m. As expected, the cylinder also has the largest 3-D location error of  $x_{error} = 0.51$  m. The cylinder 3-D location error is due to the layover and also the rotated orientation  $(\gamma, \theta, \phi)_{cylinder} = (0^\circ, 0^\circ, -5^\circ)$ . As described in the size error analysis in Section 3.2.3, a rotated orientation of the cylinder or top-hat creates an apparent 3-D location and radius estimate offset from the true values. This phenomena is due to the fact that the layover equations for the cylinder and top-hat are derived in Section 3.1.1.1 for the non-rotated orientation.

Table 4.3: Scenario 1 scatterer shape true parameters, parameter estimates, and shape check. The  $x$ ,  $y$ ,  $z$ ,  $L$ ,  $H$ ,  $r$  parameters are in meters, and  $\gamma$ ,  $\theta$ ,  $\phi$  are in degrees.

Truth or Estimate	Shape Type	Parameter								Shape Check	
		x	y	z	L	H	r	$\gamma$	$\theta$		$\phi$
Truth	plate	0	0	0	1.0	1.0	–	0	-32	0	–
Estimate	plate	0	0	0	0.97	0.99	–	0	-32.0	0	–
	trihedral	0	0	0	–	0.75	–	24.7	30.9	27.4	–
	sphere	0	0	0	–	–	0.0	–	–	–	$r \leq 0$
	cylinder	0	0	0	1.25	–	0.0	–	–	–	$r \leq 0$

Table 4.4: Scenario 2 scatterer shape true parameters, parameter estimates, and shape check. The  $x$ ,  $y$ ,  $z$ ,  $L$ ,  $H$ ,  $r$  parameters are in meters, and  $\gamma$ ,  $\theta$ ,  $\phi$  are in degrees.

Case #	Truth or Estimate	Shape Type	Parameter									Shape Check
			$x$	$y$	$z$	$L$	$H$	$r$	$\gamma$	$\theta$	$\phi$	
1	Truth	plate	0	0	1.05	1.0	1.0	–	0	-32	0	–
	Estimate	plate	-0.08	0.0	1.17	0.95	1.02	–	0.4	-32.0	0.0	–
		sphere	0.12	-0.03	1.19	–	–	-0.19	–	–	–	$r \leq 0$
2	Truth	plate	0	0	0	1.05	1.0	–	0	-32	0	–
	Estimate	plate	0	0	0	1.02	0.99	–	0.1	-32.0	0.0	–
		sphere	0	0	0	–	–	0.0	–	–	–	$r \leq 0$
3	Truth	plate	0	0	0	1.0	1.0	–	0	-33.5	0	–
	Estimate	plate	0	0	0	0.70	1.24	–	-4.8	-33.3	-0.8	–
		triangular	0	0	0	–	0.71	–	37.7	-26.4	49.2	–
		sphere	0	0	0	–	–	0.0	–	–	–	$r \leq 0$
		cylinder	0	0	0	1.60	–	0.0	–	–	–	$r \leq 0$
4	Truth	plate	0	0	1.05	1.05	1.0	–	0	-33.5	0	–
	Estimate	plate	-0.08	0.0	1.18	0.72	1.25	–	-3.8	-33.2	-0.79	–
		triangular	-0.03	0	1.08	–	0.72	–	37.7	-26.4	19.3	–
		sphere	0.16	-0.03	1.20	–	–	-0.21	–	–	–	$r \leq 0$
		cylinder	0.44	0.0	1.36	1.62	–	-0.54	–	–	–	$r \leq 0$



Table 4.5: Scenario 3 scatterer shape true parameters, parameter estimates, and shape check. The  $x$ ,  $y$ ,  $z$ ,  $L$ ,  $H$ ,  $r$  parameters are in meters, and  $\gamma$ ,  $\theta$ ,  $\phi$  are in degrees.

Truth or Estimate	Shape Type	Parameter									Shape Check
		$x$	$y$	$z$	$L$	$H$	$r$	$\gamma$	$\theta$	$\phi$	
Truth	plate	-0.3	0	0.3	0.6	0.3	–	0	-30	0	–
Estimate	plate	-0.32	0.01	0.33	0.60	0.30	–	0.0	-30.0	0.0	–
	trihedral	-0.29	0.01	0.28	–	0.32	–	17.2	32.4	18.8	–
	sphere	-0.80	-0.16	-0.20	–	–	-0.06	–	–	–	$r \leq 0$
	cylinder	-0.88	0.01	-0.06	1.15	–	0.68	-5.3	29.8	-5.5	–
Truth	dihedral <sub>1</sub>	0.25	0.5	0	0.6	0.2	–	0	0	0	–
Estimate	dihedral	0.26	0.50	-0.01	0.81	0.13	–	0.0	-0.1	0.0	–
	top-hat	-5.08	1.54	2.24	–	0.16	3.92	3.5	-26.6	-44.8	–
Truth	dihedral <sub>2</sub>	0	1.1	2.5	0.6	0.3	–	-10	0	0	–
Estimate	dihedral	-0.05	1.21	2.56	1.02	0.12	–	4.1	31.4	9.3	–
	top-hat	13.67	-0.94	-2.36	–	NaN	-10.63	–	–	–	$r \leq 0$
Truth	trihedral	0.75	0	0.5	–	0.18	–	0	0	0	–
Estimate	trihedral	0.76	0.0	0.49	–	0.18	–	0.0	0.0	0.0	–
Truth	sphere	-1.5	-1.0	0	–	–	0.75	–	–	–	–
Estimate	plate	-0.80	-1.00	0.29	0.20	0.28	–	–	–	–	$L \leq 0.3$
	sphere	-1.48	-1.00	0.01	–	–	0.75	–	–	–	–
Truth	cylinder	0.5	2.0	0	0.5	–	1.5	0	0	-5	–
Estimate	plate	1.26	2.27	1.03	0.22	0.72	–	–	–	–	$L \leq 0.3$
	trihedral	1.81	1.83	0.73	–	0.31	–	11.7	-2.7	1.3	–
	sphere	0.63	1.98	0.05	–	–	-0.06	–	–	–	$r \leq 0$
	cylinder	-0.01	1.84	-0.33	0.61	–	2.10	-9.5	-18.4	-6.9	–
Truth	top-hat	0.25	-1.5	0	–	0.4	0.6	0	0	0	–
Estimate	top-hat	0.25	-1.50	0.01	–	0.33	0.60	-0.1	-0.7	8.9	–

Once the initial location parameters are estimated, the error bounds from Step 1B in Section 3.2, Figures 3.6 - 3.12, are applied to set the upper and lower bounds for dictionary formation. The details of how the errors ranges are calculated and are applied to the initial estimates here are provided in Section 3.2.2. The error ranges are what are passed to Step 3 for dictionary formation.

#### **4.4 Step 2D: Initial Size Estimation and Bounding**

The size paramaters are estimated after the location estimates are complete. The length estimate is the measured length of the shape in the image segment. The height is calculated using the RCS, length, and radius estimates plugged into the peak RCS equation for the corresponding shape type. The height equations are provided previously in Table 3.9. The radius for the cylinder and top-hat is estimated with the 3-D location estimate, and the radius of the sphere is calculated using the RCS and peak RCS equation.

The length parameter is estimated from the image. The length parameter of the plate, dihedral, and cylinder cause a proportional spread of the peak in the image of each object. The length of the peak is measured using the length of the segment in the image. The segment length is defined as all pixels within a threshold of the peak amplitude. The chosen plate threshold is 1.2 dB, and chosen dihedral and cylinder threshold is 6.5 dB. The user defined thresholds are chosen for this thesis to minimize the error when a shape is at non-rotated orientation from Table 3.8.

The height parameter is estimated using the peak RCS and previous length and/or radius estimates. The RCS is estimated is from the HRR PH data provided by the spotlight algorithm from Step 2A in Section 4.1. The spotlight removes additional objects in the scene; other objects can affect an object's amplitude if at the same range in an HRR. The true RCS peak values are calculated using the peak RCS equations from [1] and are given in Table 4.6.

Table 4.6: Peak RCS equation for each shape. The peak values corresponds to the power received when collected at the specular direction from a shape. The specular direction is determined from the shape geometry. Specular can be determined by finding the relative angles to the radar that maximize the scatterer responses in Table 2.3.

Shape	Peak RCS
plate	$\frac{4\pi L^2 H^2}{\lambda^2}$
dihedral	$\frac{8\pi L^2 H^2}{\lambda^2}$
triangular	$\frac{12\pi H^4}{\lambda^2}$
sphere	$\pi r^2$
cylinder	$\frac{2\pi}{\lambda} r L^2$
top-hat	$\frac{8\pi r H^2}{\lambda \sqrt{2}}$

For the Scenarios tested in this thesis, the RCS estimates from the HRRs are in Table 4.7. The true values are provided from the peak RCS equations in Table 4.6.

Table 4.7: Shape true peak RCS values and measured RCS from the HRRs.

Scenario	Case	Shape	True Peak RCS (m <sup>2</sup> )	Estimated RCS (m <sup>2</sup> )
1	–	plate	558.5	520.2
2	1	plate	558.5	520.2
	2	plate	615.8	573.5
	3	plate	558.5	417.2
	4	plate	615.8	459.9
3	–	plate	18.1	18.1
	–	dihedral <sub>1</sub>	16.1	11.9
	–	dihedral <sub>1</sub>	36.2	17.2
	–	triangular	1.8	1.6
	–	sphere	1.8	1.8
	–	cylinder	15.7	14.8
	–	top-hat	11.4	7.9

The radius parameter is estimated and bounded with the 3-D location estimates using the peak location in the 2-D images. The radius is estimated at the previous step because the radius changes the location of the peak in each image.

The radius of the sphere is estimated when the 3-D location estimate is made. However, errors in the image can induce errors on the radius parameter. Therefore, the radius for the sphere is calculated using the RCS estimate. The amplitude returned from the sphere is constant, so the measured RCS is correct for any flight path.

The applicable parameters for each shape type and method of initial estimate are summarized in Table 4.8.

Table 4.8: Information used to determine the size parameter for each shape type. Length uses the peak segment width. Height is calculated from the peak RCS equation and other size parameters. Radius is estimated with the 3-D location estimate based on the image peak locations. In the case of the sphere, the radius is estimated using the peak RCS equation.

Shape	L	H	r
plate	Image	RCS	
dihedral	Image	RCS	
trihedral		RCS	
sphere			RCS
cylinder	Image		Image
top-hat		RCS	Image

The methodology to estimate each size parameter is evaluated using the thesis Scenarios. The estimated values are provided in Tables 4.3 - 4.5 with the true values in columns  $L$ ,  $H$ , and  $r$ . Scenarios 1 and 2 only have a plate in the scene. Scenario 1 and Scenario 2 Cases 1 and 2 have length and height estimates within 0.05 m. The accuracy of the length estimates are expected because the orientation of  $(\gamma, \theta, \phi)_{\text{plate}} = (0^\circ, -32^\circ, 0^\circ)$

was used to set the peak width threshold. The plate height estimate is determined using the peak RCS equation and is dependent on the RCS and length estimates for accuracy. Both the length and RCS estimates are lower than their true values; the two offset since  $H \propto \frac{\sqrt{RCS}}{L}$  such that the height estimate is within 0.02 m of the true value.

In Scenario 2 Cases 3 and 4, the pitch angle is increased to  $\theta = -33.5^\circ$ . The change in orientation angle changes the PH collection so that the peak is steeper in the image domain. The steeper peak causes a shorter length estimate. The length error is worse than Cases 1 and 2 with  $L_{error} \approx -0.30$  m. For Cases 3 and 4 the low RCS estimates are overcome by the low length estimates so the calculated height estimate is greater than the true value with an error of  $H_{error} \approx 0.25$  m for the two cases.

In Scenario 3, the same phenomena affect the size estimates as discussed in the size error analysis in Section 3.2.3. The plate length estimate matches the true value because the plate orientation angles are near the standard orientation of this thesis and within the flight path. The length estimates of the dihedrals and cylinder are longer than the true value because the shapes are skew to the flight path.

The radius of the sphere is calculated from the RCS value. The sphere estimate has no error because the received RCS value from any orientation is the peak RCS. The cylinder radius estimate is higher than the actual radius because the orientation is yawed creating a larger apparent radius. The top-hat radius has negligible error because it is at its standard orientation with the reflection point in the ground plane.

The height estimates are a function of the RCS estimate and other size estimates. The plate length and RCS estimates and trihedral RCS estimate are close to the true values, so their height estimates have near zero error. The dihedrals have low RCS estimates and high length estimates. Both factors decrease the final height estimates so the final dihedral height estimates are less than the true values with  $H_{error} = -0.07$  m. The top-hat radius estimate has no error and lends no error to the top-hat height estimate. However, the RCS

estimate is lower than the maximum, producing a low height estimate with an error of  $H_{error} = -0.07\text{m}$ .

Like the location parameters, the initial size parameter estimates are combined with the error analysis in Step 1B to bound the range of possible size parameters. The error range data for the length and height are in Figures 3.14 - 3.22. And the radius error range data for the cylinder and top-hat are in the location error analysis section in Figures 3.11(d) and 3.12(d).

#### 4.5 Step 2E: Initial Orientation Estimation and Bounding

With the location and size estimates initialized, the last parameters needed are orientation. The three orientation parameters are roll ( $\gamma$ ), pitch ( $\theta$ ), and yaw ( $\phi$ ). The orientation parameters determine rotation of a canonical shape from its baseline orientation in Figure 1.1. The roll, pitch, and yaw angles reference the right hand rule rotation about the  $x$ -axis,  $y$ -axis, and  $z$ -axis, respectively.

Initial orientation parameter estimates are done through a coarse-to-fine PH coherency match for each object in the scene. The initial 3-D location and size parameter estimates from Steps 2C and 2D are used in the search. The spotlight algorithm PHs of each scatterer are used so each scatterer can be estimated independently. Separating the PHs makes estimation simpler and decreases estimation error because the combined observed PH includes data for each scatterer. Both [1] and [2] search for the parameters iteratively using a form of sparse reconstruction such as basis pursuit (BP) or basis pursuit denoising (BPDN).

The coarse-to-fine coherency match is completed using the pseudo-code in Table 4.9

Table 4.9: Pseudo-code for orientation angle coarse-to-fine parameter estimation.

<p>Set <math>x, y, z</math> as the initial estimates from Step 2C.</p> <p>Set <math>L, H, r</math> as the initial estimates from Step 2D.</p> <p>Set <math>S</math>, the sample size for the <math>\gamma, \theta, \phi</math>.</p> <p>Set <math>C</math>, the number of coherency matches per iteration.</p> <p>Set <math>\gamma, \theta, \phi</math> to the maximum range:</p> $\gamma_{range} = [\gamma_{min}, \gamma_{max}]$ $\theta_{range} = [\theta_{min}, \theta_{max}]$ $\phi_{range} = [\phi_{min}, \phi_{max}]$ <p>Begin Coarse-to-Fine Iteration:</p> <p>Form atom dictionary. Use <math>S</math> samples of <math>\gamma, \theta, \phi</math> with equal spacing.</p> <p>Calculate coherencies: <math>\text{coherency}_i = \langle  \text{PH} ,  a_i  \rangle</math>.</p> <p>Choose <math>C</math> atoms with highest coherency: <math>a_{\text{set}} = \{a_{\text{max coh}(1)}, \dots, a_{\text{max coh}(C)}\}</math></p> <p>Set new <math>\gamma, \theta, \phi</math> range to range of <math>a_{\text{set}}</math>:</p> $\gamma_{range} = [\gamma_{min} a_{\text{set}}, \gamma_{max} a_{\text{set}}]$ $\theta_{range} = [\theta_{min} a_{\text{set}}, \theta_{max} a_{\text{set}}]$ $\phi_{range} = [\phi_{min} a_{\text{set}}, \phi_{max} a_{\text{set}}]$ <p>End iterations when the orientation ranges are within <math>\tau^\circ</math>:</p> $[(\gamma_{range} \ \& \ \theta_{range} \ \& \ \phi_{range}) < \tau^\circ]$ <p>Set <math>\gamma, \theta, \phi</math> initial estimates:</p> $\gamma_{est} = \frac{1}{2}(\gamma_{min} + \gamma_{max})$ $\theta_{est} = \frac{1}{2}(\theta_{min} + \theta_{max})$ $\phi_{est} = \frac{1}{2}(\phi_{min} + \phi_{max})$
---

At each iteration the orientation parameters are sampled for  $S$  samples with equal spacing. A dictionary is formed using the sampled orientation parameters. Therefore, the dictionary has  $S^3$  atoms. The  $C$  most coherency atoms are chosen. The minimum and maximum parameters orientation paramters of the most correlated atoms are chosen to bound the next iteration. The iteration ends when the range of each orientation parameter is within a chosen threshold,  $\tau$ .

The number of orientation samples,  $S$ , and number of correlated atoms chosen,  $C$ , per iteration are supplied in Table 4.10. The values chosen for  $S$  and  $C$  were chosen after testing all values between 5 and 11 using the Monte Carlos simulations from Step 1B. Values over 11 were not tested due to computation time constraints of running 200 trials for each combination. The stopping threshold of  $\tau = 1^\circ$  is chosen. The stopping threshold is chosen to be within the dictionary sampling size of  $5^\circ$  in Step 3A in Section 5.1.

Table 4.10: The number of samples and correlated atoms chosen for the coarse-to-fine orientation angle search. The values were chosen after testing all combination between the values of 5 and 11 using 200 Monte Carlo simulations. The values are those that gave the smallest standard deviation of error.

Shape	# Sample	# Atoms
plate	10	7
dihedral	10	8
triangular	11	7
sphere	N/A	N/A
cylinder	10	7
top-hat	11	7

The orientation estimates are provided with the 3-D location and size estimates in Tables 4.3 - 4.5. For Scenario 1, the true orientation angles are estimated using the coarse-to-fine correlation method. In Scenario 2, the worst case is Case 4 with a maximum error of  $\gamma_{error} = -3.8^\circ$ . For Scenarios 1 and 2, low orientation errors are expected because the detectable orientation angles of the plate are limited.

Scenario 3 tests all the shape types. Again, the plate errors are limited due to the small detection region; the plate orientation errors are less than  $0.1^\circ$ . Dihedral<sub>1</sub> and the triangular are both set at the standard orientation and have errors of less than  $0.1^\circ$  as well. The top-hat exhibits minor errors in the roll and pitch parameter estimates of no more than  $0.7^\circ$ . With



those two parameters near zero, the larger yaw error of  $\phi_{error} = 8.9^\circ$  is not unexpected since the yaw angle is ambiguous for zero roll and pitch for a top-hat due to its geometry.

Dihedral<sub>2</sub> and the cylinder have the largest orientation errors. The return of a dihedral is ambiguous across an azimuth cut due to its geometry. Therefore, the largest orientation error is for the pitch angle with  $\theta_{error} = 31.4^\circ$ . The coarse-to-fine correlation method uses the previous estimates of 3-D location and size. Dihedral<sub>2</sub> has errors in its location,  $y_{error} = 0.11$  m, and size,  $L_{error} = 0.43$  m,  $H_{error} = -0.18$  m. The location and size parameters estimates are used in the orientation angle estimates. The location and size errors lead to the orientation errors.

The cylinder similarly has errors in its 3-D location and size estimates. The errors of  $x_{error} = -0.51$  m,  $y_{error} = -0.16$  m,  $z_{error} = -0.33$  m,  $L_{error} = 0.11$  m, and  $r_{error} = 0.60$  m all contribute to poor orientation estimates. The cylinder has error in the three orientation parameters of  $(\gamma, \theta, \phi)_{error} = (11.7^\circ, -2.7^\circ, 1.9^\circ)$ .

The orientation initial estimates are bound using the  $3\sigma$  error values from Step 1A in Section 3.2.4. The bounds on the orientation angles are used in Step 3A in Section 5.1 for dictionary formation.

#### 4.6 Step 2F: Shape Type Check

The SPLIT algorithm in Step 2B may choose more than one shape type in Section 4.2 for a single scatterer. The size parameter estimates are used to determine if a shape type estimate is possible.

A shape size parameter cannot be less than or equal to zero. If a shape size estimate is zero or negative, the shape is discarded. This thesis utilizes the cross-range resolution to determine if a length estimate is feasible. The cross-range resolution spreads the peak width, which is used for length estimation. The cross-range resolution is 0.43 m, calculated in Equation (3.19). A shape is discarded if the length is less than 0.3 m.

The shape types selected from the SPLIT algorithm from Section 4.2 in Table 4.2 are investigated for discrepancies of their size estimates. The discarded shape types are indicated in Tables 4.3 - 4.5 with a line through the shape type name in the “Shape Type” column and a reason in “Shape Check” column.

In Scenarios 1 and 2, all the sphere and cylinder estimates are discarded because the radius parameter are estimated as less than or equal to zero. In each of these scenarios, the true scatterer is a plate. The 2-D locations are used to estimate the 3-D location. The layover locations come to a point when estimating the 3-D location. A shape with radius would have slightly different reflection points in 3-D to account for the look angle of the unique flight paths. The closest estimate for the sphere and cylinder are to have a zero radius estimate.

In Scenario 1 and 2, the trihedral cannot be discarded because the height parameter estimate is calculated from the RCS estimate. The RCS estimate cannot be negative, so the height cannot be negative.

In Scenario 3, the SPLIT algorithm correctly detects the trihedral, sphere, and top-hat. The trihedral and top-hat are chosen as the final shape type. The sphere is ambiguous with the plate in the SPLIT algorithm. The plate is discarded in the shape type because the length estimate is only 0.20 m. The sphere does not spread in the image like the shapes with a length parameter where return appear along the length of the object.

The other four shapes in Scenario 3 are only limited to the odd or even shape types. The plate and cylinder are initially estimated for the odd shapes: the plate, trihedral, sphere, or cylinder. Under the plate, the sphere is eliminated for having negative radius. Under the cylinder, the plate is eliminated for have a length less than 0.3 m and the sphere is eliminated for having a negative radius.

The two dihedrals are initially estimated as the even shapes: the dihedral or top-hat. The first dihedral check does not eliminate either shape type. The second dihedral shape type check discards the top-hat for having a negative radius estimate.

The shape check limits the number of dictionary formations and searches needed in Step 3. The shape type estimates not eliminated are passed to Step 3 along with the bounded parameters for each. In Step 3, the final parameter estimates for each shape type are made.

## V. Dictionary Formation and Dictionary Search

Step 2 in Chapter 4 provides the bounds for each object's parameters. Each parameter is sampled within the bounds for dictionary formation. In Step 3, the dictionary formation and search, performs the last functions to make the final shape type and parameter estimates for each scatterer. A simplified flow diagram of Step 3 is in Figure 5.1.

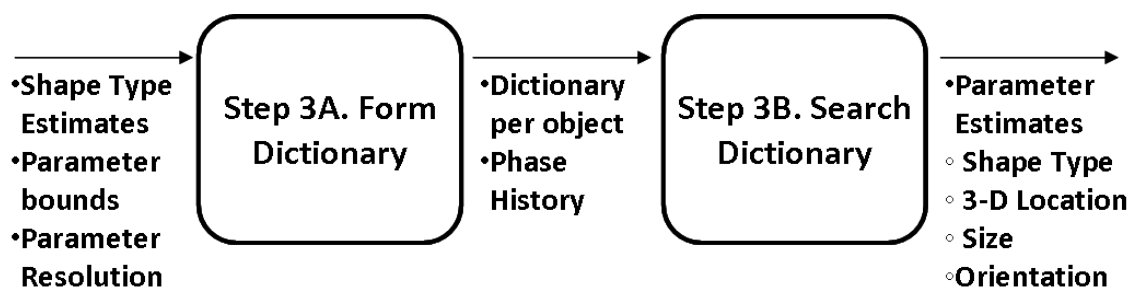


Figure 5.1: Steps to complete dictionary formation and search. The process is completed twice. The first round is for the molecule dictionary that takes into account ambiguities in a normalized dictionary. The second round samples the parameters that are ambiguous for the normalized molecule dictionary. In this second round, the ambiguity is removed by not normalizing the atoms.

A dictionary is formed by creating the PH for each permutation of the sampled parameters. The parameters of the dictionary PH that is most similar to the observed PH are the final parameter estimates. Two rounds of Step 3 are accomplished. The first round combines redundant atoms into single molecules. The second round searches the atoms within the chosen molecule. The two stage approach decreases the number of needed computations as compared to the algorithm in [2].

### 5.1 Dictionary Formation

The parameter bounds from Step 2 in Chapter 3 are used for dictionary formation. The full range of possible errors is applied to the initial estimates to form the parameter bounds,

so the true parameters must lie in this subspace. The bounds are extended by rounding the maximum up and minimum down to the nearest sampling increment. The true parameter falls in the error bounds for all Scenarios and Cases tested in this thesis.

Mathematically, the dictionary parameter range extension is demonstrated for the  $x$  parameter. This thesis uses a sampling of 0.1 m, so the bounds are calculated using

$$\begin{aligned} x_{\text{bounds}} &= [(\text{sample size}) \cdot \lfloor (x_{\min}/(\text{sample size})) \rfloor, (\text{sample size}) \cdot \lceil (x_{\max}/(\text{sample size})) \rceil] \\ &= [(0.1 \text{ m}) \lfloor (x_{\min}/0.1 \text{ m}) \rfloor, (0.1 \text{ m}) \lceil (x_{\max}/0.1 \text{ m}) \rceil]. \end{aligned} \quad (5.1)$$

Within the bounds each parameter is sampled to create a finite dictionary. The number of samples within the range is based on user parameter resolution needs. For example, for a 1 m bounded range with a desired 0.1 m resolution, eleven samples would be used. Sampling is done for each parameter separately. The resultant sampling is finer than that provided by Hammond [2] because the range is limited in Step 2. This provides more accurate results. To achieve the same sampling fidelity in [2], the number of samples grows by an order of magnitude. Sampling over a scene extent of 10 m at 0.1 m sample size would require 101 samples. The sampling used for this thesis is provided in Table 5.1.

Table 5.1: Parameter estimate sampling size used to calculate the number of samples per parameter for dictionary formation in this thesis.

Parameter	Parameter Sampling
x location	0.1 m
y location	0.1 m
z location	0.1 m
Length	0.1 m
Height	0.1 m
radius	0.1 m
roll ( $\gamma$ )	5°
pitch ( $\theta$ )	5°
yaw ( $\phi$ )	5°

A two stage dictionary approach decreases the dictionary size. First, a molecule dictionary is formed using normalized PHs. The normalization removes the amplitude from the scatterer equation. The  $H$  parameter only occurs in the amplitude term,  $A$ , (except for the plate where it is in the  $M$  term). Therefore, the two stages are used for the dihedral, trihedral, and top-hat. The  $L$  and  $r$  parameters affect more than the amplitude so are not ambiguous in a normalized PH. The  $L$  parameter is in the scatterer response,  $M$ , from Table 2.3. The  $r$  parameter is in the  $\Delta R$  phase term from Equations (2.8) and (2.9).

The atom dictionary is formed after the molecule dictionary is formed and searched. For the plate, sphere, and cylinder, only a single dictionary is formed with no clustering.

Forming the molecule dictionary by excluding the height parameter samples is more efficient than the clustering in [2]. In [2] coherency between every atom pair is calculated to cluster. Removing the coherency by checking each atom pair removes on the order of  $\sim N^2K$  calculations, where  $N$  is the number of atoms, and  $K$  is the number of samples in an atom.

Removing the ambiguous height parameter from the sample set in the molecule dictionary is what decreases the dictionary size. The reduction is demonstrated for a dihedral with  $S = 3$  samples for each parameter  $\Theta_{dihedral} = [x, y, z, L, H, \gamma, \theta, \phi]$  using Equation (2.12). The sum runs to  $J = 1$  because there is a single shape, and the product has  $Q = 8$  terms because the dihedral has 8 parameters. Combining all the permutations requires 6561 atoms shown in

$$\begin{aligned}
 N_{\text{combined}} &= \sum_{j=1}^1 \prod_{q=1}^8 (3), \\
 &= 3^8, \\
 &= 6561,
 \end{aligned} \tag{5.2}$$

The two stage approach reduces the number of dictionary entries formed and searched to 2190 shown with

$$\begin{aligned} N_{\text{molecule+atom}} &= \left[ \sum_{j=1}^1 \prod_{q=1}^7 (3) \right] + \left[ \sum_{j=1}^1 \prod_{q=1}^1 (3) \right], \\ &= 3^7 + 3, \\ &= 2190. \end{aligned} \tag{5.3}$$

The molecule dictionary is formed, searched, and the most coherent molecule is chosen using Equation (5.4) in Section 5.2. The chosen molecule retains its non-height parameters:  $(x, y, z, L, r, \gamma, \theta, \phi)$ . The atom dictionary is formed by sampling the height parameter,  $H$ . The atom dictionary is not normalized, and it is searched using LS according to Equation (5.5) in Section 5.2.

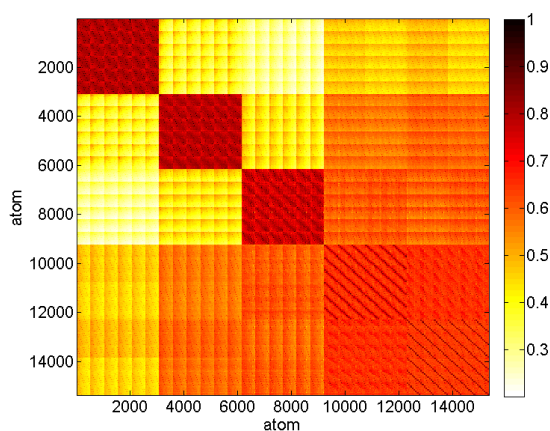
The two stage dictionary approach removes the redundant atoms in the normalized dictionary. Figures 5.2 and 5.3 show Gram matrices for  $\text{dihedral}_2$  of Scenario 3. Figure 5.2 shows how sampling all of the parameters creates redundant atoms from the height parameter. Figure 5.3 separates the molecule and atom dictionaries. Not only are less entries created, but the inter-entry coherency decreases. All of the coherency is not eliminated, as many off diagonal entries are still near 1.0.

## 5.2 Dictionary Search

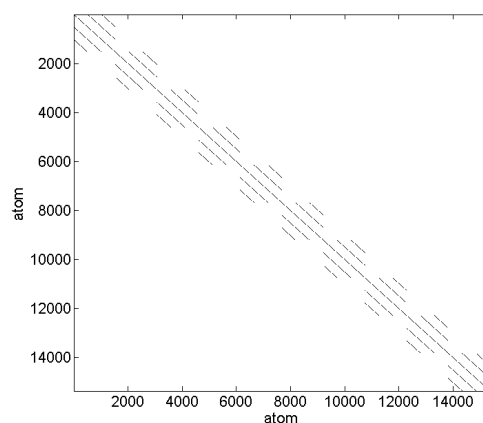
The molecule dictionary is normalized and is searched using maximum coherency as

$$\hat{\Theta} = \arg \max_{\Theta_m} \langle |\text{PH}|, |a(\Theta_m)| \rangle, \tag{5.4}$$

where the  $\Theta$  is the set of parameters of each atom;  $\hat{\Theta}$  is the chose parameter estimates; PH is the observed spotlight PH;  $a$  is the atom being tested; and  $m$  is the index of each parameter set.

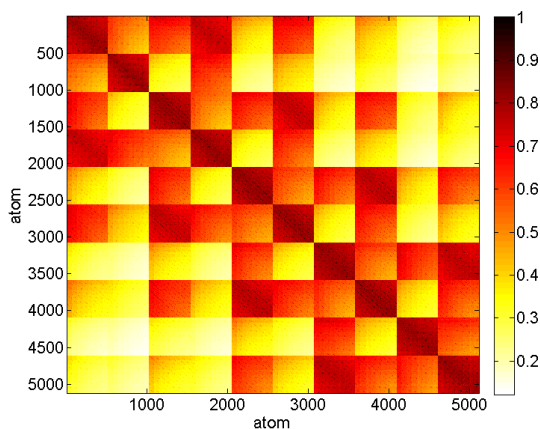


(a) Full dictionary.

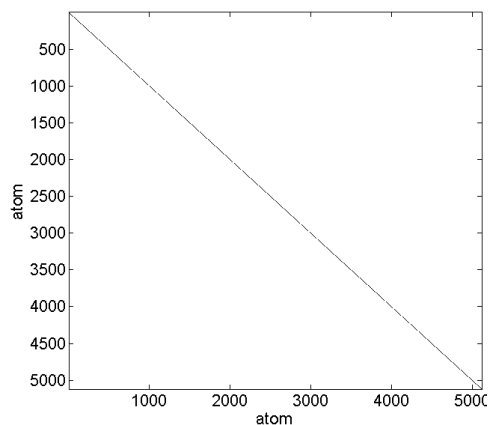


(b) Redundant atoms of the full dictionary.

Figure 5.2: Forming a full dictionary with all the parameters sampled causes redundant atoms. In (a) a full Gram matrix is provided for the dictionary formed from sampling all the parameters. (b) shows the atoms pairs with a coherency of 1.0; the off diagonal points give the redundant atoms.



(a) Molecule dictionary.



(b) Redundant molecules.

Figure 5.3: Forming the molecule dictionary first removes redundant atoms due to height. (a) gives the Gram matrix of the molecule dictionary. (b) shows the molecules with a coherency of 1.0. No off diagonal coherency shows that there are no redundant molecules.



The chosen molecule is sampled to form the atom dictionary. The atom dictionary is not normalized and is searched using

$$\hat{\Theta}_{\text{Final}} = \arg \min_{\Theta_m} \| |\text{PH}| - |a(\Theta_m)| \|_2. \quad (5.5)$$

The final estimate of a scatterer is the parameters estimated for a given shape type. The shape type check cannot always eliminate all but one shape type. For cases where more than one shape type remains for a scatterer, the parameters are estimated for all shape types. The selected PH atom of each shape type is compared to the spotlight PH using an inner product according to

$$\text{correlation}_{\Gamma} = \langle |\text{PH}|, |a_{\Gamma, \hat{\Theta}}| \rangle. \quad (5.6)$$

The shape type and its parameters with the maximum correlation is chosen as the final estimate for the scatterer. The absolute value of observed and atoms is used because of the location phase term in the model,  $e^{jk\Delta R}$ . The phase term modulates the overall shape of the scatterer response with high frequency. Small offsets in location can adjust the phase such that there is destructive interference in the coherency calculation. The absolute value maintains the scatterer response shape,  $M$ .

The final shape types and parameter estimates for each Scenario are provided in Tables 5.2, 5.3, and 5.5. The “Initial” estimates are the initial parameter estimates from Step 2 in Chapter 4. The “Final” estimates are the parameters of the atom chosen after completing the molecule and dictionary search. The “Coherency Check” column is the coherency measure between the observed spotlight PH and the chosen dictionary atom. The coherency is calculated using Equation (5.4).

In Scenario 1, the parameters of one of the dictionary atoms is that of the true parameters. Because the parameters are the same, that atom is chosen with a final coherency match of 1.0. The trihedral has a lower coherency of 0.87 with the observed

Table 5.2: Scenario 1 scatterer shape true parameters, parameter estimates, and shape coherency check. The initial parameter estimates are from Step 2 in Table 4.3. The final estimates are the parameters of the atom chosen after the two stage dictionary search. The  $x$ ,  $y$ ,  $z$ ,  $L$ ,  $H$ ,  $r$  parameters are in meters, and  $\gamma$ ,  $\theta$ ,  $\phi$  are in degrees. The final choice, which is in bold font, is the plate over the trihedral because its coherency with the observed PH is greater.

Estimate Type	Shape Type	Parameter								Coherency	
		x	y	z	L	H	r	$\gamma$	$\theta$	$\phi$	Check
Truth	plate	0	0	0	1.0	1.0	–	0	-32	0	1
Initial	plate	0	0	0	0.97	0.99	–	0	-32.0	0	–
Final	<b>plate</b>	0	0	0	1.0	1.0	–	0	-32	0	<b>1.0</b>
Initial	trihedral	0	0	0	–	0.75	–	24.7	30.9	27.4	–
Final	trihedral	0	0	0	–	2.0	–	40	40	50	0.87

PH so is eliminated as the final shape choice. The near flat PH response of a trihedral is difficult to match to the sinc behavior of the plate PH.

The difference of the two PHs are show in Figure 5.4. Only the magnitude of the imaginary portion of the PH of each is shown. The plate and trihedral PH amplitude response  $M$  has only and imaginary component from Equation (2.8) detailed in Table 2.3. The complex PH return includes both a real and imaginary component when the location offset,  $\Delta R$ , introduces a phase offset. The plate has no phase offset because it is centered at the origin.

Scenario 1 can be compared to Scenario 1 from [2]. Both use a scatterer whose parameters equal the parameters of a dictionary atom. The final result is equivalent; the correct atom is selected.

In Scenario 2, each true parameter set is chosen such that the parameters cannot match the parameters of a dictionary atom. In Cases 1 - 3, one parameter is changed from the list of possible dictionary parameters. The atom chosen for the Cases 2 and 3 is the atom with the parameters closest to the true parameters. Case 3 demonstrates the advantage of the dictionary estimate over the initial estimates. The initial size estimates are poor with errors

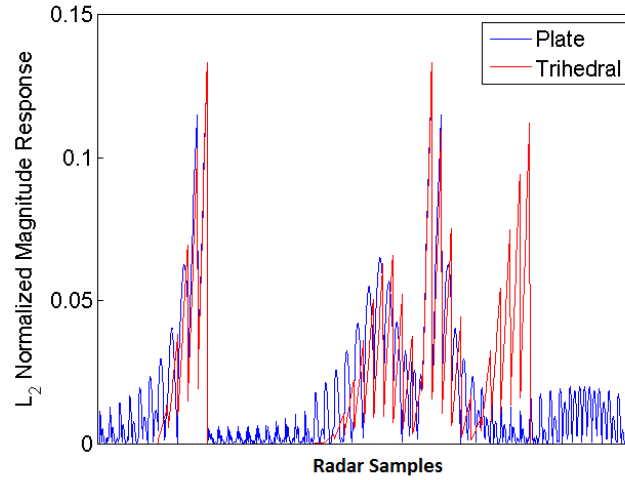


Figure 5.4: Scenario 1 plate and trihedral PHs chosen to match the spotlight PH of the plate in the scene. The PH shows only the imaginary responses of each radar sample. The real part is zero because the plate is centered at  $(x, y, z) = (0 \text{ m}, 0 \text{ m}, 0 \text{ m})$ . The sinc behavior of the plate cannot be replicated by a trihedral response. The response discontinuities are from the flight path partitions.

of  $L_{error} = -0.30 \text{ m}$ ,  $H_{error} = 0.24 \text{ m}$ . The dictionary search compares all the PH history information and is able to match the observed PH with the better final estimates such that the size errors go to zero.

Scenario 3 Case 4 is more complicated because one parameter from each location, size, and orientation parameter set is offset from the dictionary entries. In Cases 1 and 4, the dictionary search does not find the closest atom in parameter space, but the final estimate does improve the parameter estimate for six of the eight parameters. For the two cases where the parameter estimates are worse from dictionary search ( $x$  and  $z$  location), the final parameters from the dictionary are the parameters closest to the initial estimates. The initial  $x$  and  $z$  estimates of  $-0.08 \text{ m}$  and  $1.18 \text{ m}$  are estimated at  $-0.1 \text{ m}$  and  $1.2 \text{ m}$ , respectively.

The reason for the location parameter choice of  $(-0.1 \text{ m}, 0 \text{ m}, 1.2 \text{ m})$  over the closer atom with location parameters  $(0 \text{ m}, 0 \text{ m}, 1.1 \text{ m})$  can be attributed to the resultant  $\Delta R$ . Recall

Table 5.3: Scenario 2 scatterer shape true parameters, parameter estimates, and shape coherency check. The initial parameter estimates are from Step 2 in Table 4.4. The final estimates are the parameters of the atom chosen after the two stage dictionary search. The  $x$ ,  $y$ ,  $z$ ,  $L$ ,  $H$ ,  $r$  parameters are in meters, and  $\gamma$ ,  $\theta$ ,  $\phi$  are in degrees. The final for choice for each case is in bold font with a greater coherency with the observed PH.

Case #	Truth or Estimate	Shape Type	Parameter									Coherency Check
			x	y	z	L	H	r	$\gamma$	$\theta$	$\phi$	
1	Truth	plate	0	0	1.05	1.0	1.0	–	0	-32	0	1
	Initial	plate	-0.08	0.0	1.17	0.95	1.02	–	0.4	-32.0	0.0	–
	Final	<b>plate</b>	-0.1	0	1.2	1.0	1.0	–	0	-32	0	<b>0.85</b>
2	Truth	plate	0	0	0	1.05	1.0	–	0	-32	0	1
	Initial	plate	0	0	0	1.02	0.99	–	0.1	-32.0	0.0	–
	Final	<b>plate</b>	0	0	0	1.1	1.0	–	0	-32	0	<b>0.999</b>
3	Truth	plate	0	0	0	1.0	1.0	–	0	-33.5	0	1
	Initial	plate	0	0	0	0.70	1.24	–	-4.8	-33.3	-0.8	–
	Final	<b>plate</b>	0	0	0	1.0	1.0	–	0	-33	0	<b>0.99</b>
	Initial	triangular	0	0	0	–	0.71	–	37.7	-26.4	49.2	–
	Final	triangular	0	0	0	–	0.7	–	65	-25	70	0.58
4	Truth	plate	0	0	1.05	1.05	1.0	–	0	-33.5	0	1
	Initial	plate	-0.08	0.0	1.18	0.72	1.25	–	-3.8	-33.2	-0.79	–
	Final	<b>plate</b>	-0.1	0.1	1.2	1.0	1.1	–	0	-33	0	<b>0.89</b>
	Initial	triangular	-0.03	0	1.08	–	0.72	–	37.7	-26.4	19.3	–
	Final	triangular	-0.1	0.1	1.2	–	0.7	–	65	-25	70	0.49

from Equation (2.9) that  $\Delta R = \Delta R_0 + \Delta R_r$ .  $\Delta R_0 = 2(x \cos(\tilde{\theta}) \cos(\tilde{\phi}) + y \cos(\tilde{\theta}) \sin(\tilde{\phi}) + z \sin(\tilde{\theta}))$ , and  $\Delta R_r = 0$  for flat shape. The  $\Delta R$  is calculated for the parameter cases in Table 5.4. The chosen atom provides the closest 3-D range location.

Table 5.4: Scenario 2 Case 4  $\Delta R$  consistency coherency check. The term “Closest” is in terms of the parameter estimates individually. The  $\Delta R$  accounts for the Euclidean distance after combining the  $x$ ,  $y$ , and  $z$  location vectors.

Parameters	$\Delta R$ (m)
True	1.05
Chosen Atom	1.03
“Closest” Atom	1.10

The trihedral shape type is discarded for Cases 3 and 4. The same analysis is made from Scenario 1; creating a PH from the trihedral PH equation to match the observed plate PH cannot be accomplished. In these two cases, the plate coherency of 0.99 and 0.82 are much higher than the trihedral coherency of 0.58 and 0.49.

In Scenario 3, the plate, dihedral<sub>2</sub>, sphere, and cylinder all have parameters that match the parameters of a dictionary atom. Each of these shapes is matched to the atom with the parameters equal to the true parameters. In this set, the extra shape type estimates are eliminated since their coherency is less than 1.0 of the chosen atom of the correct shape type.

Dihedral<sub>1</sub> chooses the atom with the closest parameters except the height and pitch. The height parameter has an error of -0.1 m, which is one sample removed from the true parameter. Similarly the pitch estimate is one sample away from the true parameter estimating 5° instead of 0°. Choosing a smaller height parameter decreases the amplitude of the return. The dihedral pitch angle for zero roll angle only affects the amplitude as well due to its symmetry. The pitch puts the specular closer to the flight path, increasing the amplitude. The height underestimate and pitch increase in apparent amplitude offset.

The trihedral location and size choose the closest parameters in the dictionary. The orientation of the trihedral produces near flat amplitude for any small flight path cut. Therefore, little difference exists in the PH for many orientation angles. The coherency of the trihedral spotlight PH is 0.8194 for the chosen atom with  $(\gamma, \theta, \phi) = (-15^\circ, 0^\circ, -10^\circ)$  where as the expected parameters  $(\gamma, \theta, \phi) = (0^\circ, 0^\circ, 0^\circ)$  have a coherency of 0.8193. In general, the trihedral orientation is difficult to estimate. In a real world situation with signal errors, estimating the orientation via dictionary is much more difficult because the coherency estimates are so close.

The top-hat dictionary parameter estimates are all within one dictionary sample from the true parameters. The  $x$  location is not in the dictionary and the closest parameter is

Table 5.5: Scenario 3 scatterer shape true parameters, parameter estimates, and shape check. The initial parameter estimates are from Step 2 in Table 4.5. The final estimates are the parameters of the atom chosen after the two stage dictionary search. The  $x$ ,  $y$ ,  $z$ ,  $L$ ,  $H$ ,  $r$  parameters are in meters, and  $\gamma$ ,  $\theta$ ,  $\phi$  are in degrees. The final for choice for each case is in bold font with a greater coherency with the corresponding spotlight PH.

Truth or Estimate	Shape Type	Parameter									Coherency Check
		x	y	z	L	H	r	$\gamma$	$\theta$	$\phi$	
Truth	plate	-0.3	0	0.3	0.6	0.3	–	0	-30	0	1
Initial	plate	-0.32	0.01	0.33	0.60	0.30	–	0.0	-30.0	0.0	–
Final	<b>plate</b>	-0.3	0	0.3	0.6	0.3	–	0	-30	0	<b>1.0</b>
Initial	triangular	-0.29	0.01	0.28	–	0.32	–	17.2	32.4	18.8	–
Final	triangular	-0.3	0	0.3	–	0.4	–	20	30	20	0.82
Initial	cylinder	-0.88	0.01	-0.06	1.15	–	0.68	-5.3	29.8	-5.5	–
Final	cylinder	-0.9	0	0.1	1.1	–	0.7	-5	30	-5	0.79
Truth	dihedral <sub>1</sub>	0.25	0.5	0	0.6	0.2	–	0	0	0	1
Initial	dihedral	0.26	0.50	-0.01	0.81	0.13	–	0.0	-0.1	0.0	–
Final	<b>dihedral</b>	0.3	0.5	0.0	0.6	0.1	–	0	5	0	<b>0.81</b>
Initial	top-hat	-5.08	1.54	2.24	–	0.16	3.92	3.5	-26.6	-44.8	–
Final	top-hat	0.6	0.6	0.5	–	0.6	0.5	-5	-30	-75	0.76
Truth	dihedral <sub>2</sub>	0	1.1	2.5	0.6	0.3	–	-10	0	0	1
Initial	dihedral	-0.05	1.21	2.56	1.02	0.12	–	4.1	31.4	9.3	–
Final	<b>dihedral</b>	0	1.1	2.5	0.6	0.3	–	-10	0	0	<b>1.0</b>
Truth	triangular	0.75	0	0.5	–	0.18	–	0	0	0	1
Initial	triangular	0.76	0.0	0.49	–	0.18	–	0.0	0.0	0.0	–
Final	<b>triangular</b>	0.7	0.0	0.5	–	0.2	–	-15	0	-10	<b>0.82</b>
Truth	sphere	-1.5	-1.0	0	–	–	0.75	–	–	–	1
Initial	sphere	-1.48	-1.00	0.01	–	–	0.75	–	–	–	–
Final	<b>sphere</b>	-1.5	-1.0	0.0	–	–	0.75	–	–	–	<b>1</b>
Truth	cylinder	0.5	2.0	0	0.5	–	1.5	0	0	-5	1
Initial	triangular	1.81	1.83	0.73	–	0.31	–	11.7	-2.7	1.3	–
Final	triangular	1.8	1.8	0.7	–	0.3	–	10	-5	0	0.65
Initial	cylinder	-0.01	1.84	-0.33	0.61	–	2.10	-9.5	-18.4	-6.9	–
Final	<b>cylinder</b>	0.5	2.0	0	0.5	–	1.5	0	0	-5	<b>1.0</b>
Truth	top-hat	0.25	-1.5	0	–	0.4	0.6	0	0	0	1
Initial	top-hat	0.25	-1.50	0.01	–	0.33	0.60	-0.1	-0.7	8.9	–
Final	<b>top-hat</b>	0.2	-1.4	0	–	0.3	0.7	0	5	0	<b>0.92</b>

chosen. As discussed for Scenario 2, Cases 1 and 4, the location determines the phase parameter of the PH model equation to get the correct range. The top-hat radius parameter estimate may be offset to correct for the true range relative to sampled  $x$  location. The  $\Delta R$  for the chosen atom is closer to the true value than the “closest” atom as shown in Table 5.6.

Table 5.6: Scenario 2 Case 4  $\Delta R$  consistency check.

Parameters	$\Delta R$ (m)
True	1.47
Chosen Atom	1.54
“Closest” Atom	1.39

The top-hat increase in the radius causes an increases in amplitude. The amplitude is offset with a smaller height estimate. The top-hat pitch angle has a similar effect to the dihedral for flight paths about zero azimuth. The combination of the height, radius, and pitch angle of the chosen atom are approximately the same as the true amplitude;  $|A|_{true} = 0.37k$  and  $|A|_{chosen} = 0.34k$ , where  $k$  is the wavenumber. Given the radius was increased, if the height and pitch angles were estimated as the true parameters, the amplitude would be even lower at  $|A|_{closest} = 0.30k$ .

### 5.2.1 Dictionary Results Summary.

The location estimate is bound in Step 2. The 3-D location parameters only appear in the PH equations for location offset from scene center in the  $\Delta R$  variable. Within the bound 3-D location parameters subspace, the parameter combination with the most similar range is chosen. Without the initial bounds, the 3-D location could be much farther from the true location because constant range to the radar in 3-D is an entire plane.

The dictionary search size parameter estimates achieve at worst 0.1 m error relative to the true parameter. The length parameter estimate is always correct because the length determines the PH overall scattering response for the plate, dihedral and cylinder.

Mathematically the scattering response is shown with the sinc function along the flight path,  $M \propto \text{sinc}(kL \sin \phi \cos \theta)$ .

The height estimate scales the amplitude of the response. The accuracy of height parameter depends on the orientation estimate. The estimated orientation affects relative orientation of the shape specular direction to the flight path. A correct orientation estimate will provide a correct height estimate so the return amplitude is correct. If the estimated orientation points specular closer to the flight path, the height will decrease to compensate for the actual amplitude observed.

The radius estimate is a balance of the amplitude response and true range to the object. Like the 3-D location, the radius adjusts the range to the target from the  $\Delta R_r$  term. The radius is also in the scattering response amplitude  $A$ .

The orientation parameters are the most ubiquitous in the scattering models. The orientation affects the specular direction relative to the flight path, so it affects the amplitude of the response. The shape relative orientation to the flight path affects which parts of the sinc function are observed as shown by the azimuth and elevation angles in the scattering response models. Lastly, the orientation angles affect the length of the  $\Delta R_r$  observed for the cylinder and top-hat geometries. The correct orientation angles are selected if in the dictionary atoms except when the angle has very little affect on the PH. Three cases of little PH change with orientation angle are shown prior in Scenario 3.

The Scenarios evaluated in Chapters 3 - 5 are a subset of the parameter combinations tested. The parameters of this subset are in Tables 3.13 - 3.15. Appendix B includes additional cases of each scenario with results. The results found for each of these additional Scenario and Case pairs follow the same analysis for each parameter found for the Scenarios in Chapter 5.



## **VI. Conclusions and Future Work**

This thesis utilized derived canonical shape scattering models [1] to parameterize high dimension radar return data. The overarching objective of this thesis is to improve dictionary formation and search to deliver more accurate parameter estimates. This final chapter outlines the methodology used to achieve the thesis objectives, summarizes the results and analysis, and points to future work to improve upon the research foundation of this thesis.

### **6.1 Objectives and Methodology**

The two main objectives achieved in this thesis are decreased computation and improved parameter estimates. Both objectives are achieved. The details of objective satisfaction are discussed in terms of the methodology steps.

Step 1 decreases computation. The use of 2-D images for analysis decreases computation time relative to [1] where regularized 3-D images are formed. A regularized 3-D image formation requires an extra dimension of interpolation to form the image in the backprojection integral, requires more samples to reduce the point spread function sidelobes, and requires additional calculations to regularize the image to remove the majority of sidelobes with a sparsity assumption.

Step 2 decreases computation. This step preprocesses the error bounds based on analysis of the collection flight path and radar operating parameters, estimates the shape type and model parameter, and combines the two to limit the searchable parameter subspace for dictionary formation. The error bounds are preprocessed once for a flight path and add negligible computation when bounding parameters. Location and size parameter estimation is faster than in [1] because only a few data values and simple calculations

are used. Orientation initialization does require more computation relative to [1] because of the iterative dictionary search. Overall, the parameter estimation is faster.

Step 3 decreases computation time relative to both [1] and [2]. Sampled dictionary formation and search is chosen relative to iterative gradient descent [1] for its improved computation speed. This thesis greatly improves the computation time relative to [2] by replacing the molecule dictionary formation using full dictionary coherency with the efficient molecule formation based on known coherency in the model equations. The full coherency search requires an inner product calculation for each dictionary pair: computations  $\sim \frac{1}{2}N^2 * 2K$ , where  $N$  is the number of dictionary atoms and  $K$  is the number of sample points in a dictionary entry. Using the known coherency from the model equations requires no calculations. The molecule dictionary in this thesis decreases the number of dictionary samples on the order of the number of samples of the height parameter as well.

Step 3 improves the final parameter estimates. Parameter estimation accuracy is improved relative to [2] due to the parameter bounding. In [2], the dictionary is formed using a coarse sampling based on computer memory constraints. The location and size parameters are only able to be sampled to 5 m and 0.5 m resolution, respectively. The orientation parameter is not sampled due to the memory constraint, so no ability to estimate orientation is demonstrated.

## **6.2 Results and Conclusions**

Chapters 3 - 5 provide estimates for each function used throughout the process Steps 1-3. The final shape type and parameter estimates showed accurate results. The final shape type estimate after SPLIT initial estimates, a shape type check, and a final coherency measure against the observed PH correctly chooses the correct shape type in each tested Scenario and Case. The Scenarios showed the dictionary atom with parameters matching the true parameters of a scatterer is always correctly chosen. For scatterers with parameters

not all matched to the parameters of a dictionary atom, the worst estimates are one sample away from the true parameters (Location: 0.1 m; Size: 0.1 m; Orientation: 5°).

The errors in parameter estimates are determined through analysis of the model equations. Attempting to match the correct range,  $\Delta R$ , can cause error in the location, radius, and orientation. Fitting the atom parameters to the sinc response behavior from  $M$  can lead to incorrect the orientation parameters. Adjusting to the amplitude of the observed PH,  $A$ , can cause error in the height, radius, and orientation parameters. Although the parameters are adjusted slightly to fit the observed PH when the atom with the true parameters is not in the dictionary, the final estimate is more accurate relative to [2]. Limiting the searched parameter subspace prevents gross errors from occurring.

The framework in this thesis can be used for any collection flight path and radar parameters. The preprocessing error analysis can be done prior to collection so adjustments can be made if needed. The dictionary sample resolution can be adjusted for user needs as well, so flexibility exists to trade off computation time and increased accuracy.

## **6.3 Future Work**

Many avenues exist to build on the framework of the thesis. The subsections for future work focus on the three main Steps in the thesis as well as the overall system in the first subsection.

### ***6.3.1 Flight Path and System Analysis.***

Flight path analysis. Simple flight paths were chosen to provide non-singular transfer matrices,  $\Theta$ , for each shape type. Increasing the diversity of the flight paths could provide better data for location and radius estimates. Additionally, developing a strong flight path algorithm to determine quality of target parameters would be helpful to a user of this algorithm.

Add system noise, path attenuation, and/or clutter. The thesis was completed in an idealized environment. Adding noise, path attenuation, and/or clutter will demonstrate

which parameters are more susceptible to errors for a real world system. Larger errors in estimates will cause larger bounds for each estimate and make dictionary formation and search more difficult.

Account for scatterer peak splits. Not all flight paths and scatterer orientations remain in a single segment during 2-D image formation. Developing a way to determine if a scatterer peak in one image corresponds to more peaks in another image would provide more 2-D location estimates and subsequent samples for 3-D location estimation.

### ***6.3.2 Shape Choice and Parameter Estimation.***

Flight path and PH. The directionality of PH responses could be incorporated into the algorithm to more definitively discern the shape of each segment. For example, SPLIT does not distinguish between a plate and a sphere. If the amplitude of the radar return through flight path is constant, the segment is more likely to be a sphere than a plate. The PH amplitude change over the flight path could be used to more finely determine shape type.

Orientation Estimates inform Location Estimate. The location parameter estimate calculations for the sphere, cylinder, and top-hat all include the radius parameter. The system of equations are derived for the baseline orientation of each of the three shapes. Re-deriving the layover equations to include orientation geometry would correct for some of the object location and radius error. The orientation estimates with error bounds would provide feedback for more accurate location and radius parameter estimates.

Orientation/RCS refinement for Height Estimate. The height parameter calculation uses the peak RCS equation. However, the maximum received PH amplitude does not provide peak RCS unless the flight path geometry samples at the peak RCS location. The orientation estimates can be used to determine the distance the flight path is from the peak RCS direction. The PH equations can be resolved for the maximum potential RCS given the flight path and orientation. The height parameter can then be calculated using the true maximum RCS given the flight path and orientation.

## Appendix A: Grazing Angle and Tilt Angle Derivations

Appendix C of [13] derives the angles associated with the flight path and image plane created from the collected PH. The coordinate systems to determine the angles are shown in Figure A.1. The ground plane coordinates labeled  $(\bar{x}, \bar{y}, \bar{z})$ , where the  $\bar{y}$  coordinate points to the center of the flight path projected into the ground plane. The slant plane coordinates are labeled  $(\hat{x}, \hat{y}, \hat{z})$ . The  $\hat{y}$  vector points to the middle of the flight path, and  $\hat{z}$  is orthogonal to the flight path. All of the coordinates are unit vectors.

The coordinate system used for the targets in this paper have the positive x-axis at zero azimuth and elevation, the y-axis orthogonal in the ground plane at 90° azimuth, and the z-axis is vertical using the right hand rule convention. Using this as a reference, Jakowatz's vector components are found according to Figure A.1 with the following equations:

$$\bar{x} = [\sin(\phi), \cos(-\phi), 0]^T,$$

$$\bar{y} = [\cos(\phi), \sin(\phi), 0]^T,$$

$$\bar{z} = [0, 0, 1]^T,$$

where  $\phi$  is the azimuth angle in the midpoint of the flight path. An azimuth angle of zero is orthogonal to the standard flight path.

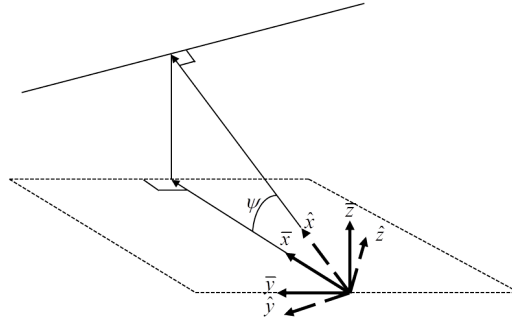


Figure A.1: Slant Plane Coordinate System [13].

The slant plane unit vectors are determined using the following equations:

$$\begin{aligned}\hat{y} &= \frac{[\cos(\phi) \cos(\theta), \sin(\phi) \cos(\theta), \sin(\theta)]^T}{|\hat{y}|}, \\ \hat{z} &= \frac{(v_{start} \times v_{end})}{|\hat{z}|}, \\ \text{where } v_{start} &= [\cos(\phi_s) \cos(\theta_s), \sin(\phi_s) \cos(\theta_s), \sin(\theta_s)]^T, \\ v_{end} &= [\cos(\phi_e) \cos(\theta_e), \sin(\phi_e) \cos(\theta_e), \sin(\theta_e)]^T, \\ \text{and } \hat{x} &= \frac{\hat{y} \times \hat{z}}{|\hat{x}|}.\end{aligned}$$

The variable  $\theta$  denotes the elevation angle, the operator ‘ $\times$ ’ denotes a vector cross product, and the subscripts  $s$  and  $e$  denote the start and end locations of the flight path.

The unit vector,  $\hat{z}$  is orthogonal to the slant plane; the geometry is shown in Figure A.2. Therefore, this is the direction of projection for a point onto the image plane. The grazing angle and tilt angle are calculated as

$$\begin{aligned}\psi &= \arctan\left(\frac{\hat{z}_z}{\hat{z}_x}\right), \\ \eta &= \arctan\left(\frac{\hat{z}_z}{\hat{z}_y}\right).\end{aligned}$$

The angles  $\psi$  and  $\eta$  are used to determine the orthogonal layover angles within the image. The relationships between the scatterer location in 3-D and image location are given in Chapter 3. The equation for each shape includes the layover angles.

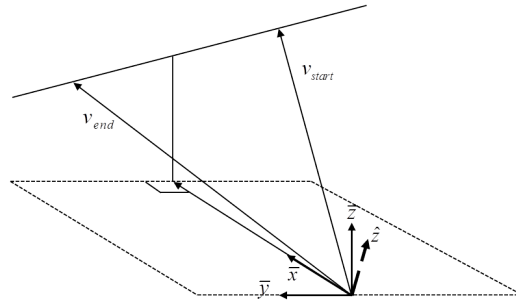


Figure A.2: Cross product geometry for  $\hat{z}$ .

## Appendix B: Additional Results

The results in Chapter 4 provide outputs for a single baseline case for each scenario. Appendix B provides outputs for cases involving all shape types. Scenarios 1 is evaluated for each shape type for parameters that coincide with an entry in the dictionary.

Scenario 2 is tested for each shape type. For each shape type a case is run with a location parameter offset from the dictionary entries, a size parameter offset from the dictionary entries, and an orientation parameter offset from the dictionary entries. Each shape type is tested with one of each of the parameters offset from the dictionary entries.

Scenario 3 is unique in its layout as to compare result to Dr. Jackson's dissertation [1]. As such no additional cases are run for scenario 3.

### B.1 Scenario 1

Scenario 1 is tested for each shape type with the parameters in the dictionary. For completeness, the results of the plate from Chapter 4 are included.

#### *B.1.1 Plate.*

Table B.1: Scenario 1 plate SPLIT shape type estimates.

<b>True shape type</b>	plate
<b>Detected shape type</b>	plate/sphere
<b>Confidence</b>	0.87
<b>Polarization</b>	odd
<b>Shape Estimate</b>	plate, sphere, cylinder, trihedral

Table B.2: Scenario 1 plate shape check.

Truth or Estimate	Shape Type	Shape Check
Truth	plate	–
Estimate	plate	–
	trihedral	–
	sphere	$r \leq 0$
	eylinder	$r \leq 0$

Table B.3: Scenario 1 plate scatterer shape true parameters, parameter estimates, and shape check. The  $x$ ,  $y$ ,  $z$ ,  $L$ ,  $H$ ,  $r$  parameters are in meters, and  $\gamma$ ,  $\theta$ ,  $\phi$  are in degrees.

Estimate Type	Shape Type	Parameter								Coherency	
		x	y	z	L	H	r	$\gamma$	$\theta$	$\phi$	Check
Truth	plate	0	0	0	1.0	1.0	–	0	-32	0	1
Initial	plate	0	0	0	0.97	0.99	–	0	-32.0	0	–
Final	<b>plate</b>	0	0	0	1.0	1.0	–	0	-32	0	<b>1.0</b>
Initial	trihedral	0	0	0	–	0.75	–	24.7	30.9	27.4	–
Final	trihedral	0	0	0	–	2.0	–	40	40	50	0.87

The algorithm correctly estimates the shape type as a plate for Scenario 1 as shown previously in Chapter 4. Additionally, the correct parameters are chosen from the dictionary.



### B.1.2 Dihedral.

No shape type estimate is made for the dihedral from the SPLIT algorithm.

Table B.4: Scenario 1 dihedral SPLIT shape type estimates.

<b>True shape type</b>	dihedral
<b>Detected shape type</b>	
<b>Confidence</b>	
<b>Polarization</b>	even
<b>Shape Estimate</b>	dihedral, top-hat

Table B.5: Scenario 1 dihedral shape check.

<b>Truth or Estimate</b>	<b>Shape Type</b>	<b>Shape Check</b>
Truth	dihedral	–
Estimate	dihedral top-hat	– $r \leq 0$

Table B.6: Scenario 1 dihedral true parameters and parameter estimates. The  $x$ ,  $y$ ,  $z$ ,  $L$ ,  $H$ ,  $r$  parameters are in meters, and  $\gamma$ ,  $\theta$ ,  $\phi$  are in degrees.

Estimate Type	Shape Type	Parameter								Coherency Check	
		x	y	z	L	H	r	$\gamma$	$\theta$		$\phi$
Truth	dihedral	0	0	0	1.0	1.0	–	0	0	0	1
Initial	dihedral	0	0	0	1.00	0.86	–	0.01	0.0	0.01	–
Final	<b>dihedral</b>	0	0	0	1.0	1.0	–	0	0	0	<b>1.0</b>

The algorithm correctly estimates the shape type as a dihedral for Scenario 1. Additionally, the correct parameters are chosen from the dictionary.

### B.1.3 Trihedral.

Table B.7: Scenario 1 trihedral SPLIT shape type estimates.

<b>True shape type</b>	trihedral
<b>Detected shape type</b>	trihedral
<b>Confidence</b>	0.91
<b>Polarization</b>	odd
<b>Shape Estimate</b>	trihedral

Table B.8: Scenario 1 trihedral shape check.

<b>Truth or Estimate</b>	<b>Shape Type</b>	<b>Shape Check</b>
Truth	trihedral	–
Estimate	trihedral	–

Table B.9: Scenario 1 trihedral true parameters and parameter estimates. The  $x$ ,  $y$ ,  $z$ ,  $L$ ,  $H$ ,  $r$  parameters are in meters, and  $\gamma$ ,  $\theta$ ,  $\phi$  are in degrees.

<b>Estimate Type</b>	<b>Shape Type</b>	<b>Parameter</b>									<b>Coherency Check</b>
		<b>x</b>	<b>y</b>	<b>z</b>	<b>L</b>	<b>H</b>	<b>r</b>	<b><math>\gamma</math></b>	<b><math>\theta</math></b>	<b><math>\phi</math></b>	
Truth	trihedral	0	0	0	–	1.0	–	0	0	0	1
Initial	trihedral	0	0	0	–	0.98	–	0.01	0.01	0.0	–
Final	<b>trihedral</b>	0	0	0	–	1.0	–	0	0	0	<b>1.0</b>

The algorithm correctly estimates the shape type as a trihedral for Scenario 1. Additionally, the correct parameters are chosen from the dictionary.

#### B.1.4 Sphere.

Table B.10: Scenario 1 sphere SPLIT shape type estimates.

<b>True shape type</b>	sphere
<b>Detected shape type</b>	–
<b>Confidence</b>	–
<b>Polarization</b>	odd
<b>Shape Estimate</b>	plate, sphere, cylinder, trihedral

Table B.11: Scenario 1 sphere initial and final shape type estimates.

<b>Estimate Type</b>	<b>Detected Shape</b>	<b>Discard Reason</b>
Truth	sphere	–
Estimate	plate	$L < 0.2$
Estimate	sphere	–
Estimate	cylinder	–
Estimate	trihedral	–

Table B.12: Scenario 1 sphere true parameters and parameter estimates. The  $x$ ,  $y$ ,  $z$ ,  $L$ ,  $H$ ,  $r$  parameters are in meters, and  $\gamma$ ,  $\theta$ ,  $\phi$  are in degrees.

<b>Estimate Type</b>	<b>Shape Type</b>	<b>Parameter</b>									<b>Coherency Check</b>
		<b>x</b>	<b>y</b>	<b>z</b>	<b>L</b>	<b>H</b>	<b>r</b>	<b><math>\gamma</math></b>	<b><math>\theta</math></b>	<b><math>\phi</math></b>	
Truth	sphere	0	0	0	–	–	0.5	–	–	–	1
Initial	sphere	0.01	0	0	–	–	0.49	–	–	–	–
Final	<b>sphere</b>	0	0	0	–	–	0.5	–	–	–	<b>1.0</b>
Initial	cylinder	0.04	0	0.03	0.52	–	0.45	-44.8	-22.4	-14.8	–
Final	cylinder	0.6	0.1	0	0.5	–	1.0	-44	-63	-15	0.83
Initial	trihedral	0.43	0	0.25	–	0.15	–	46.0	-15.2	21.1	–
Final	trihedral	0.4	0	0.3	–	0.1	–	14	-24	41	0.93

The dictionary search on the sphere finds the correct parameters in the dictionary. The SPLIT algorithm is not able to distinguish the sphere from the other odd bounce shapes. The plate is discarded because the length estimate is less than 0.2 m. The cylinder and trihedral orientations point the shapes such that returns are not detectable for the entire flight path. Therefore, the sphere not only has the correct parameters but is the most feasible shape type.

### B.1.5 Cylinder.

Table B.13: Scenario 1 cylinder SPLIT shape type estimates.

<b>True shape type</b>	cylinder
<b>Detected shape type</b>	plate/sphere
<b>Confidence</b>	0.63
<b>Polarization</b>	odd
<b>Shape Estimate</b>	plate, sphere, cylinder, trihedral

Table B.14: Scenario 1 cylinder initial and final shape type estimates.

<b>Estimate Type</b>	<b>Detected Shape</b>	<b>Discard Reason</b>
Truth	cylinder	–
Estimate	plate	–
Estimate	sphere	$r \leq 0$
Estimate	cylinder	–
Estimate	trihedral	–

Table B.15: Scenario 1 cylinder true parameters and parameter estimates. The  $x$ ,  $y$ ,  $z$ ,  $L$ ,  $H$ ,  $r$  parameters are in meters, and  $\gamma$ ,  $\theta$ ,  $\phi$  are in degrees.

<b>Estimate Type</b>	<b>Shape Type</b>	<b>Parameter</b>									<b>Coherency Check</b>
		<b>x</b>	<b>y</b>	<b>z</b>	<b>L</b>	<b>H</b>	<b>r</b>	<b><math>\gamma</math></b>	<b><math>\theta</math></b>	<b><math>\phi</math></b>	
Truth	cylinder	0	0	0	1.0	–	0.5	0	0	0	1
Initial	plate	0.40	0.0	0.30	1.04	0.18	–	-0.6	-35.0	0.0	–
Final	plate	0.4	0	0.3	1.0	0.1	–	0	-35	0	0.92
Initial	trihedral	0.44	0.0	0.25	1.04	0.18	–	-0.6	-35.0	0.0	–
Final	trihedral	0.4	0	0.3	1.0	0.1	–	0	-35	0	0.84
Initial	cylinder	-0.09	0.0	-0.05	1.00	–	0.60	0.0	19.7	0.0	–
Final	<b>cylinder</b>	0.6	-0.2	0.2	1.0	–	0.1	0	20	0	<b>1.0</b>

The pitch parameter is also estimated poorly. The pitch parameter ambiguity is also expected with a small roll angle as the cylinder is identical for all pitch angles with zero roll.

The algorithm is not able to discard the plate or trihedral in the shape type check. The maximum coherency chooses the cylinder correctly.

### B.1.6 Top-Hat.

Table B.16: Scenario 1 dihedral SPLIT shape type estimates.

<b>True shape type</b>	top-hat
<b>Detected shape type</b>	–
<b>Confidence</b>	–
<b>Polarization</b>	even
<b>Shape Estimate</b>	dihedral, top-hat

Table B.17: Scenario 1 top-hat initial and final shape type estimates.

<b>Estimate Type</b>	<b>Detected Shape</b>	<b>Discard Reason</b>
Truth	top-hat	–
Estimate	dihedral	–
Estimate	top-hat	–

Table B.18: Scenario 1 top-hat true parameters and parameter estimates. The  $x$ ,  $y$ ,  $z$ ,  $L$ ,  $H$ ,  $r$  parameters are in meters, and  $\gamma$ ,  $\theta$ ,  $\phi$  are in degrees.

<b>Estimate Type</b>	<b>Shape Type</b>	<b>Parameter</b>									<b>Coherency Check</b>
		<b>x</b>	<b>y</b>	<b>z</b>	<b>L</b>	<b>H</b>	<b>r</b>	<b><math>\gamma</math></b>	<b><math>\theta</math></b>	<b><math>\phi</math></b>	
Truth	top-hat	0	0	0	–	1.0	0.5	0	0	0	1
Initial	dihedral	0.50	0.0	0.0	0.55	0.39	–	-52.4	-12.4	-41.1	–
Final	dihedral	0.5	0	0	0.1	0.8	–	-45	15	-50	0.63
Initial	top-hat	0.0	0.0	0.0	–	0.84	0.50	-0.1	-0.7	8.9	–
Final	<b>top-hat</b>	0	0	0	–	1.0	0.5	0	0	0	<b>1.0</b>

The shape type estimates after the shape type check keep the dihedral and top-hat. After the final coherency check, the top-hat is correctly chosen and the parameter estimates are correct.

## B.2 Scenario 2

Scenario 2 is tested for each shape type with the parameters in the dictionary. For completeness, the results of the plate from Chapter 4 are included. To limit the number of trials run, only the most complex combination, Case 4, for the additional shapes is tested.

### B.2.1 Plate.

Table B.19: Scenario 2 plate SPLIT shape type estimates and shape type check.

Case Number	Estimate Type	Detected Shape	Discard Reason
All	Truth	plate	
Case 1	Estimate	plate	
	Estimate	sphere	$r < 0.01$
	Estimate	eylinder	$r < 0$
Case 2	Estimate	plate	
	Estimate	sphere	$r < 0.01$
	Estimate	eylinder	RCS
Case 3	Estimate	plate	
	Estimate	sphere	$r < 0.01$
	Estimate	eylinder	$r < 0$
	Estimate	trihedral	
Case 4	Estimate	plate	
	Estimate	sphere	$r < 0.01$
	Estimate	eylinder	$r < 0$
	Estimate	trihedral	

Table B.20: Scenario 2 plate shape true parameters, parameter estimates, and coherency shape check. The  $x$ ,  $y$ ,  $z$ ,  $L$ ,  $H$ ,  $r$  parameters are in meters, and  $\gamma$ ,  $\theta$ ,  $\phi$  are in degrees.

Case #	Truth or Estimate	Shape Type	Parameter									Coherency Check
			x	y	z	L	H	r	$\gamma$	$\theta$	$\phi$	
1	Truth	plate	0	0	1.05	1.0	1.0	–	0	-32	0	1
	Initial	plate	-0.08	0.0	1.17	0.95	1.02	–	0.4	-32.0	0.0	–
	Final	<b>plate</b>	-0.1	0	1.2	1.0	1.0	–	0	-32	0	<b>0.85</b>
2	Truth	plate	0	0	0	1.05	1.0	–	0	-32	0	1
	Initial	plate	0	0	0	1.02	0.99	–	0.1	-32.0	0.0	–
	Final	<b>plate</b>	0	0	0	1.1	1.0	–	0	-32	0	<b>0.999</b>
3	Truth	plate	0	0	0	1.0	1.0	–	0	-33.5	0	1
	Initial	plate	0	0	0	0.70	1.24	–	-4.8	-33.3	-0.8	–
	Final	<b>plate</b>	0	0	0	1.0	1.0	–	0	-33	0	<b>0.99</b>
	Initial	triherdal	0	0	0	–	0.71	–	37.7	-26.4	49.2	–
	Final	triherdal	0	0	0	–	0.7	–	65	-25	70	0.58
4	Truth	plate	0	0	1.05	1.05	1.0	–	0	-33.5	0	1
	Initial	plate	-0.08	0.0	1.18	0.72	1.25	–	-3.8	-33.2	-0.79	–
	Final	<b>plate</b>	-0.1	0.1	1.2	1.0	1.1	–	0	-33	0	<b>0.89</b>
	Initial	triherdal	-0.03	0	1.08	–	0.72	–	37.7	-26.4	19.3	–
	Final	triherdal	-0.1	0.1	1.2	–	0.7	–	65	-25	70	0.49

### B.2.2 Dihedral.

Table B.21: Scenario 2 dihedral SPLIT shape type estimates and shape type check.

Case Number	Estimate Type	Detected Shape	Discard Reason
All	Truth	dihedral	–
Case 4	Estimate	dihedral	–
	Estimate	<del>top-hat</del>	$r \leq 0$

Table B.22: Scenario 2 dihedral shape true parameters, parameter estimates, and coherency shape check. The  $x$ ,  $y$ ,  $z$ ,  $L$ ,  $H$ ,  $r$  parameters are in meters, and  $\gamma$ ,  $\theta$ ,  $\phi$  are in degrees.

Case #	Truth or Estimate	Shape Type	Parameter									Coherency Check
			x	y	z	L	H	r	$\gamma$	$\theta$	$\phi$	
4	Truth	dihedral	0	0	1.05	1.05	1.0	–	0	1	0	1
	Initial	dihedral	0.0	0.0	1.05	1.05	0.88	–	0.0	0.9	0.0	–
	Final	<b>dihedral</b>	0	0	1.1	1.1	0.9	–	0	10	0	<b>0.99</b>

### B.2.3 Trihedral.

Table B.23: Scenario 2 trihedral SPLIT shape type estimates and shape type check.

Case Number	Estimate Type	Detected Shape	Discard Reason
All	Truth	trihedral	
Case 4	Estimate	plate	$L \leq 0.3$
	Estimate	sphere	$r < 0.01$
	Estimate	cylinder	$r < 0$
	Estimate	trihedral	–

Table B.24: Scenario 2 trihedral shape true parameters, parameter estimates, and coherency shape check. The  $x$ ,  $y$ ,  $z$ ,  $L$ ,  $H$ ,  $r$  parameters are in meters, and  $\gamma$ ,  $\theta$ ,  $\phi$  are in degrees.

Case #	Truth or Estimate	Shape Type	Parameter									Coherency Check
			x	y	z	L	H	r	$\gamma$	$\theta$	$\phi$	
4	Truth	trihedral	0	0	1.05	–	1.05	–	0	1	0	1
	Initial	trihedral	0.0	0.0	1.05	–	1.03	–	0.0	1.0	0.0	–
	Final	<b>trihedral</b>	0.0	0.0	1.0	–	1.0	–	-10	0.0	-10	<b>0.71</b>

### B.2.4 Sphere.



Table B.25: Scenario 2 sphere shape estimates.

Case Number	Estimate Type	Detected Shape	Discard Reason
All	Truth	sphere	
Case 4	Estimate Estimate	plate sphere	$L \leq 0.3$

Table B.26: Scenario 2 sphere shape true parameters, parameter estimates, and coherency shape check. The  $x$ ,  $y$ ,  $z$ ,  $L$ ,  $H$ ,  $r$  parameters are in meters, and  $\gamma$ ,  $\theta$ ,  $\phi$  are in degrees.

Case #	Truth or Estimate	Shape Type	Parameter									Coherency Check
			x	y	z	L	H	r	$\gamma$	$\theta$	$\phi$	
4	Truth	sphere	0	0	1.05	–	–	0.55	–	–	–	1
	Initial	sphere	0.04	-0.01	1.05	–	–	0.55	–	–	–	–
	Final	<b>sphere</b>	-0.1	0.0	1.0	–	–	0.55	–	–	–	<b>0.98</b>

### B.2.5 Cylinder.

Table B.27: Scenario 2 cylinder shape estimates.

Case Number	Estimate Type	Detected Shape	Discard Reason
All	Truth	cylinder	
Case 4	Estimate Estimate Estimate Estimate	plate sphere cylinder triherdal	

Table B.28: Scenario 2 cylinder shape true parameters, parameter estimates, and coherency shape check. The  $x$ ,  $y$ ,  $z$ ,  $L$ ,  $H$ ,  $r$  parameters are in meters, and  $\gamma$ ,  $\theta$ ,  $\phi$  are in degrees.

Case #	Truth or Estimate	Shape Type	Parameter									Coherency Check
			x	y	z	L	H	r	$\gamma$	$\theta$	$\phi$	
4	Truth	cylinder	0	0	1.05	1.05	1.0	–	0	1	0	1
	Initial	plate	0.33	0.0	1.46	1.05	0.19	–	-0.4	-34.7	0.0	–
	Final	plate	0.4	0.0	1.4	1.0	0.2	–	0	-35	0	0.92
	Initial	trihedral	0.43	0.0	1.30	–	0.33	–	-11.6	-30.3	-0.8	–
	Final	trihedral	0.5	0.0	1.4	–	0.4	–	0	-30	0	0.54
	Initial	sphere	-0.20	-0.30	0.63	–	–	2.63	–	–	–	–
	Final	sphere	-0.1	-0.3	0.5	–	–	2.6	–	–	–	0.51
	Initial	cylinder	0.0	0.0	1.05	1.05	–	0.49	0.0	19.7	0.0	–
	Final	<b>cylinder</b>	0.1	0	1.1	1.1	–	0.5	0	-20	0	<b>0.97</b>

### B.2.6 Top-hat.

Table B.29: Scenario 2 top-hat SPLIT shape type estimates and shape type check.

Case Number	Estimate Type	Detected Shape	Discard Reason
All	Truth	top-hat	–
Case 4	Estimate	top-hat	–

Table B.30: Scenario 2 top-hat shape true parameters, parameter estimates, and coherency shape check. The  $x$ ,  $y$ ,  $z$ ,  $L$ ,  $H$ ,  $r$  parameters are in meters, and  $\gamma$ ,  $\theta$ ,  $\phi$  are in degrees.

Case #	Truth or Estimate	Shape Type	Parameter									Coherency Check
			x	y	z	L	H	r	$\gamma$	$\theta$	$\phi$	
4	Truth	top-hat	0	0	1.05	–	1.05	0.5	0	1	0	1
	Initial	top-hat	0.03	-0.01	1.04	–	0.93	0.47	-0.1	0.7	-5.5	–
	Final	<b>top-hat</b>	-0.2	0.0	1.2	–	1.0	0.6	-5	0	-10	<b>0.90</b>

### **B.3 Scenario 3**

No additional cases are run for Scenario 3. The full results are in Chapter 4.

## Bibliography

- [1] J. A. Jackson, Three-Dimensional Feature Models for Synthetic Aperture Radar and Experiments in Feature Extraction, Ph.D. thesis, The Ohio State University, Columbus, OH, 2009.
- [2] G. B. Hammond, “SAR canonical feature extraction using molecule dictionaries,” M.S. thesis, Air Force Institute of Technology, Wright-Patterson AFB, OH, 2012.
- [3] G. B. Hammond and J. A. Jackson, “SAR canonical feature extraction using molecule dictionaries,” in 2013 IEEE Radar Conference (RADAR), 2013.
- [4] J.A. Jackson, “Analytic physical optics solution for bistatic, 3d scattering from a dihedral corner reflector,” IEEE Transactions on Antennas and Propagation, vol. 60, no. 3, pp. 1486–1495, March 2012.
- [5] M. Koets, “Automated algorithms for extraction of physically relevant features from synthetic aperture radar imagery,” M.S. thesis, The Ohio State University, Columbus, OH, 1998.
- [6] L. C. Potter and R. L. Moses, “Attributed scattering centers for SAR ATR,” IEEE Transactions on Image Processing, vol. 6, no. 1, pp. 79–91, Jan. 1997.
- [7] M. A. Koets and R. L. Moses, “Image domain feature extraction from synthetic aperture imagery,” in 1999 IEEE International Conference Proceedings of the Acoustics, Speech, and Signal Processing - Volume 04, Washington, DC, 1999, ICASSP '99, pp. 2319–2322, IEEE Computer Society.
- [8] M. J. Gerry, L. Potter, I. J. Gupta, and A. van der Merwe, “A parametric model for synthetic aperture radar measurements,” IEEE Trans. on Antennas and Propagation, vol. 47, no. 7, pp. 1179–1188, Jul. 1999.
- [9] Y. Akyildiz, “Feature extraction from synthetic aperture radar imagery,” M.S. thesis, The Ohio State University, Columbus, OH, 2000.
- [10] L. Potter H. Chiang, R. L. Moses, “Model-based classification of radar images,” IEEE Transactions on Information Theory, vol. 46, no. 5, pp. 1842–1854, 2002.
- [11] J. A. Jackson and R. L. Moses, “Feature extraction algorithm for 3D scene modeling and visualization using monostatic SAR,” Algorithms for Synthetic Aperture Radar Imagery XIII, SPIE Proceedings, vol. 6237, 3 May 2006.
- [12] J. A. Jackson and R. L. Moses, “Identifiability of 3D attributed scattering features from sparse nonlinear apertures,” in Proceedings of SPIE Algorithms for Synthetic Aperture Radar Imagery XIV, 2007, vol. 6568.

- [13] C. V. Jakowatz, D. E. Wahl, P. H. Eichel, D. C. Ghiglia, and P. A. Thompson, Spotlight-mode Synthetic Aperture Radar: A Signal Processing Approach, Kluwer Academic Publishers, Boston, MA, 1996.
- [14] A. K. Jain, Fundamentals of Digital Image Processing, Prentice Hall, Englewood Cliffs, N.J., 1989.
- [15] M. H. Hayes, Schaum's Outline of Digital Signal Processing, McGraw Hill, New York, second edition, 2012.
- [16] J. A. Jackson, "EENG 714: Advanced radar systems analysis," Class Notes, Air Force Institute of Technology, 2013.
- [17] J. A. Richards, Target Model Generation from Multiple Synthetic Aperture Radar Images, Ph.D. thesis, M.I.T, Cambridge, MA.
- [18] J. A. Richards, A. S. Willsky, and J. W. Fisher, "Expectation-maximization approach to target model generation from multiple synthetic aperture radar images," Optical Engineering, pp. 150–166, 2002.
- [19] M. Richards, J. Scheer, and W. Holm, Principles of Modern Radar, Scitech Publishing, Inc., Raleigh, NC, 2010.
- [20] J. B. Keller, "Geometrical theory of diffraction," Journal of the Optical Society of America, pp. 116–130, 1962.
- [21] M. Cetin and W. C. Karl, "Feature-enhanced synthetic aperture radar image formation based on nonquadratic regularization," Image Processing, IEEE Transactions on, vol. 10, no. 4, pp. 623–631, 2001.
- [22] T.J. Kragh and A.A. Kharbouch, "Monotonic iterative algorithms for SAR image restoration," in 2006 IEEE International Conference on Image Processing, Oct 2006, pp. 645–648.
- [23] M. Ferrara, J. A. Jackson, and C. Austin, "Enhancement of multi-pass 3d circular SAR images using sparse reconstruction techniques," Algorithms for Synthetic Aperture Radar Imagery XVI, Proceedings of SPIE, vol. 7337, no. 01, 2009.
- [24] J. A. Jackson, "Automated image segmentation for synthetic aperture radar feature extraction," in Proceedings of the IEEE 2010 National Aerospace and Electronics Conference (NAECON), 2010, pp. 45–49.
- [25] J. Stach and E. LeBaron, "Enhanced image editing by peak region segmentation," in Proceedings of the AMTA Symposium, October 1996.
- [26] D. F. Fuller, Phase History Decomposition for efficient Scatterer Classification in SAR Imagery, Ph.D. thesis, Air Force Institute of Technology, Wright-Patterson AFB, OH, 2009.

<b>REPORT DOCUMENTATION PAGE</b>					<i>Form Approved</i> <b>OMB No. 0704-0188</b>	
The public reporting burden for this collection of information is estimated to average 1 hour per response, including the time for reviewing instructions, searching existing data sources, gathering and maintaining the data needed, and completing and reviewing the collection of information. Send comments regarding this burden estimate or any other aspect of this collection of information, including suggestions for reducing this burden to Department of Defense, Washington Headquarters Services, Directorate for Information Operations and Reports (0704-0188), 1215 Jefferson Davis Highway, Suite 1204, Arlington, VA 22202-4302. Respondents should be aware that notwithstanding any other provision of law, no person shall be subject to any penalty for failing to comply with a collection of information if it does not display a currently valid OMB control number. <b>PLEASE DO NOT RETURN YOUR FORM TO THE ABOVE ADDRESS.</b>						
<b>1. REPORT DATE</b> (DD-MM-YYYY) 27-03-2014		<b>2. REPORT TYPE</b> Master's Thesis		<b>3. DATES COVERED</b> (From — To) Oct 2012–Mar 2014		
<b>4. TITLE AND SUBTITLE</b>  Improved Dictionary Formation and Search for Synthetic Aperture Radar Canonical Shape Feature Extraction				<b>5a. CONTRACT NUMBER</b>		
				<b>5b. GRANT NUMBER</b>		
				<b>5c. PROGRAM ELEMENT NUMBER</b>		
<b>6. AUTHOR(S)</b>  Crosser, Matthew P., Captain, USAF				<b>5d. PROJECT NUMBER</b>  LRIR12RY19COR		
				<b>5e. TASK NUMBER</b>		
				<b>5f. WORK UNIT NUMBER</b>		
<b>7. PERFORMING ORGANIZATION NAME(S) AND ADDRESS(ES)</b> Air Force Institute of Technology Graduate School of Engineering and Management (AFIT/EN) 2950 Hobson Way WPAFB, OH 45433-7765					<b>8. PERFORMING ORGANIZATION REPORT NUMBER</b>  AFIT-ENG-14-M-21	
<b>9. SPONSORING / MONITORING AGENCY NAME(S) AND ADDRESS(ES)</b> Air Force Office of Scientific Research Dr. Michael Kendra 875 N. Randolph St. Suite 325 Arlington, VA 22203 michael.kendra@afosr.af.mil					<b>10. SPONSOR/MONITOR'S ACRONYM(S)</b>  AFOSR/RTA	
					<b>11. SPONSOR/MONITOR'S REPORT NUMBER(S)</b>	
<b>12. DISTRIBUTION / AVAILABILITY STATEMENT</b> DISTRIBUTION STATEMENT A: APPROVED FOR PUBLIC RELEASE; DISTRIBUTION UNLIMITED						
<b>13. SUPPLEMENTARY NOTES</b> This material is declared a work of the U.S. Government and is not subject to copyright protection in the United States.						
<b>14. ABSTRACT</b> ATR requires detecting and estimating distinguishing characteristics of a target of interest. Radar data provides range and amplitude information; range distinguishes location relative to the radar whereas amplitude determines strength of reflectivity. Strong reflecting scattering features of targets are detected from a combination of radar returns, or radar PH data. Strong scatterers are modeled as canonical shapes (a plate, dihedral, trihedral, sphere, cylinder, or top-hat). Modeling the scatterers as canonical shapes takes the high dimensional radar PH from each scatterer and parameterizes the scatterer according to its location, size, and orientation. This thesis efficiently estimates the parameters of canonical shapes from radar PH data using dictionary search. Target scattering peaks are detected using 2-D SAR imaging. The parameters are estimated with decreased computation and improved accuracy relative to previous algorithms through reduced SAR image processing, informed parameter subspace bounding, and more efficient dictionary clustering. The effects of the collection flight path and radar parameters are investigated to permit pre-collection error analysis. The results show that even for a limited collection geometry, the dictionary estimates the canonical shape scatterer parameters well.						
<b>15. SUBJECT TERMS</b> SAR imaging, Canonical Shape parameterization, Dictionary Formation and Search						
<b>16. SECURITY CLASSIFICATION OF:</b>			<b>17. LIMITATION OF ABSTRACT</b>  UU		<b>18. NUMBER OF PAGES</b>  158	
a. REPORT	b. ABSTRACT	c. THIS PAGE				
U	U	U	<b>19a. NAME OF RESPONSIBLE PERSON</b> Dr. Julie A. Jackson, AFIT/ENG			
				<b>19b. TELEPHONE NUMBER</b> (include area code) (937) 255-3636 x4678 julie.jackson@afit.edu		